An eddy-resolving Reynolds stress model for unsteady flow computations: development and application

Vom Fachbereich Maschinenbau
an der Technischen Universität Darmstadt
zur
Erlangung des Grades eines Doktor-Ingenieurs (Dr.-Ing.)
genehmigte

D i s s e r t a t i o n

vorgelegt von

Dipl.-Ing. Robert Maduta

aus Bukarest

Berichterstatter:	Prof. Dr.-Ing. C. Tropea
Mitberichterstatter:	Apl. Prof. Dr.-Ing. S. Jakirlic
	Apl. Prof. Dr. rer. nat. A. Sadiki
Tag der Einreichung:	04.02.2013
Tag der mündlichen Prüfung:	29.05.2013

Darmstadt 2013
D17 (Diss. Darmstadt)

Hiermit versichere ich, die vorliegende Doktorarbeit unter der Betreuung von Prof. Dr.-Ing. C. Tropea nur mit den angegebenen Hilfsmitteln selbständig angefertigt zu haben.

Darmstadt, den 4. Februar 2013,

Abstract

The present study focuses on a turbulence modeling strategy aiming at advancement of the Reynolds-averaged Navier-Stokes (RANS) approach. The modeling strategy relies on an anisotropy-resolving near-wall second-moment closure model, which is extended to behave as an eddy-resolving model with respect to capturing spatial and temporal variability of turbulence scales. The model should not comprise any parameter depending explicitly on the grid spacing. It means the objective is to formulate a "true" Unsteady RANS (URANS) model. An additional term in the corresponding length-scale determining equation providing a selective assessment of its production represents a key parameter in this novel URANS approach. This term modeled in terms of the von Karman length scale representing the ratio of the second to the first derivative of the velocity field in line with the scale-adaptivity concept (SAS - scale adaptive simulation) introduced by Menter and Egorov [35]. In addition, the background RANS model has been "numerically stabilized" by reformulating some terms - primarily diffusive transport and gradient production - in conjunction with an appropriately defined wall boundary condition for the dissipation rate of kinetic energy of turbulence. Herewith, the use of high-order numerical schemes, such as 2^{nd} order central differencing scheme, is promoted; this issue is of crucial importance with respect to preventing the possible fallback from mainly resolved turbulent structures to modeled ones.

The predictive performances of this instability-sensitive, eddy-resolving model was checked by computing different flow cases including separation from a sharp-edged surface (backward-facing step configurations) and continuous flat and curved surfaces (flow past a tandem cylinder configuration, flow over a 2D Hill and in a 3D Diffuser in a range of geometrical parameters and Reynolds numbers). The results obtained are in closest agreement with available reference data, outperforming significantly the results pertinent to the conventional model of turbulence. Prior to that several globally stable flows, such as natural decay of homogeneous isotropic turbulence and flow in a plane channel have been computed in course of the model calibration. It should be emphasized that in all cases considered the fluctuating

velocity field was obtained started from the steady RANS results.

Finally, an appropriate modification of the background second-moment closure model in the “Steady RANS” framework is proposed leading to substantially improved turbulence level prediction - and consequently the mean flow field - in the separating flow regions; by simultaneously retaining good results in attached flow regions.

Kurzfassung

Die vorliegende Doktorarbeit befasst sich mit der Entwicklung und Anwendung eines neuartigen, instationären Reynolds-gemittelten Navier-Stokes (URANS) Modells, welches als Basis das Skalen-adaptive Konzept (SAS), eingeführt von Menter und Egorov [35], verwendet. Durch Kombination mit einem Reynolds Spannungs Modell, welches den statistischen Ansatz wiedergibt, ist das neue Modell in der Lage, wie man im Laufe dieser Arbeit sehen wird, turbulente Strukturen in der Strömung aufzulösen ohne in einer Gleichung die explizite Gitterabhängigkeit zu benötigen. Der Schlüsselparameter ist dabei ein zusätzlicher Term in der Dissipationsgleichung, welcher selektiv die Produktion der Dissipation in angemessener Weise erhöht. Er besteht aus dem Verhältnis der zweiten zur ersten Ableitung des Geschwindigkeitsfeldes. Die Stabilisierung des Reynolds Spannungs Modells in numerischer Hinsicht, durch die Umformulierung bestimmter Terme und das Abändern einer Wandrandbedingung, ist unerlässlich um numerische Diskretisierungsschemata hoher Ordnung verwenden zu können, welche einen Wechsel von hauptsächlich aufgelösten, turbulenten Strukturen zu Modellierten vermeiden.

Es werden im Zuge dieser Arbeit verschiedene Anwendungsfälle mit Strömungsablösungen von gekrümmten Oberflächen (Anordnung von zweidimensionalen Hügeln, der dreidimensionale Diffusor sowie eine Tandemzylinderanordnung), von spitzen Kanten (zurückspringende Stufe) sowie auch Solche ohne Ablösungen (ebener Kanal, Zerfall von turbulenten Strukturen ohne äußere Einwirkung) berechnet werden. Des weiteren werden die durchweg positiven Ergebnisse mit Referenzdaten verglichen werden um die quantitative Effizienz des neuartigen Modells offenzulegen. Es gilt an dieser Stele festzuhalten, dass in allen berechneten Fällen das Modell von sich aus in einen Strukturauflösenden Modus gewechselt ist, wobei jede Simulation auf ein stationäres Feld gestartet wurde.

In dem letzten Abschnitt befasst sich diese Arbeit mit einer Modifikation des Reynolds Spannungs Modells innerhalb der stationären Simulationsmöglichkeiten. Es wird gezeigt werden, dass mit einer leichten Abänderung

des Skalen adaptiven Konzepts verbesserte Ergebnisse bezüglich abgelöster Strömungen erzielt werden können, ohne jedoch die gute Berechenbarkeit von angelegten Strömungen zu beeinflussen.

Acknowledgements

Financial support by the European project ATAAC is gratefully acknowledged.

This work has been carried out at the Institute of Fluid Dynamics and Aerodynamcs SLA of the Technische Universität Darmstadt during the period between April 2009 to September 2012.

I would like to thank Prof. Dr.-Ing. habil. Cameron Tropea and Apl. Prof. Dr.-Ing. habil. Suad Jakirlic for the possibility to do this work and for their helpful comments on the present work. Especially Apl. Prof. Dr.-Ing. habil. Suad Jakirlic very often helped me out with his deep knowledge in turbulence modeling. He always took his time answering my questions, while he guided me in the right direction if necessary. I would also like to thank my family and my girlfriend Christina who supported and encouraged me, especially during the last months. My cousin Anamaria was a great help with correcting a lot of my English grammar.

Finally I would like to thank my colleagues from the SLA Institute for creating a pleasant atmosphere and the secretaries for handling all the administrative issues.

Contents

1 Introduction

1.1 Motivation

Turbulence in connection with fluid flow occurs in a great variety of occasions with industrial relevance but also in every day situations. External aerodynamics (flow over wings or plane bodies), internal aerodynamics (flow through compressor and turbine configurations), external and internal hydrodynamics (ship and pipe flows), combustion and weatherforecast just to mention a few. Since it obviously plays an important role, the understanding of the phenomenon is promoted for a fairly long time [46]. Nowadays, with increasing computer power, computational fluid dynamics (CFD) have developed as a principal supporter for experimental work. The equations governing the particular turbulent flow problem, are solved numerically on a modeled grid reflecting the actual geometry of interest. To not only support, but also substitute experiments, the results of the computer simulations have to be quite accurate and fast. The two points are in contradiction to each other as will be shown in the following.

The most accurate way to compute a turbulent flow numerically, is by directly solving the transport equations for momentum, energy and the continuity equation, which is called direct numerical simulation (DNS). By directly solving, it is meant that no mathematical model describing and simplifying physics in conjunction with turbulence is used. It is by definition accurate, but it also implies that every effect has to be resolved, in the sense that the numerical grid as well as the chosen time step inside the computation have to be fine enough not to lose any kind of information. Since no model is used, lost information is fed immediately into the transport equations leading consequently to wrong predictions of the flow field. An important parameter which describes, on a certain level, how turbulent a flow problem really is, is the so called Reynolds number Re. The Reynolds number, which is basically the ratio between inertia and viscous forces, can be expressed by a characteristic velocity U, a characteristic length scale H and the molecular viscosity ν with $Re = UH/\nu$. Increasing Re increases the turbulence in the flow which is accompanied by an

increase in turbulent structures and a decrease in structure sizes at the smaller levels. The number of points needed for the numerical grid scales approximately with Re^3 for a DNS [43]. This is a very steep increase and limits automatically the use of this method to very abstract and simple geometries with very low Reynolds numbers. Even with, the nowadays highly increasing computer power, a DNS won't be feasible for industrial relevant cases for many decades. One further problem is the fact, that many parts of the coupled differential equations are solved implicitly, which leads to a disproportionate increase of computational time needed, with increasing the number of gridpoints. To overcome this problem, turbulence models have been introduced in the early 70's starting with the work of Hanjalic, Spalding and Launder [16] [31]. They made use of the average procedure on the differential equations introduced by Reynolds [47]. With that, the turbulent flow problem is described in its average, with the equations containing an extra term that describes the turbulent interaction and has to be modeled. Due to the averaging procedure such kind of models are known as Reynolds Averaged Navier-Stokes models. Since the turbulent interactions as a whole are modeled, relatively coarse computational grids can be used. If one homogeneous direction exists in the flow field (homogeneous in terms of averaged quantities) the complete third dimension can be skipped, since the impact coming from the third dimension is anyhow accounted for by the model. Very large time steps can be used since again only the average of the flow quantities is computed.
The extra term in the averaged momentum equation, called Reynolds stress tensor, can be described by different approaches, of which the second moment closure is the most sophisticated one. It prescribes for each quantity inside the symmetric tensor a differential equation leading to six coupled differential equations. RANS models can give for a variety of turbulent flow cases very accurate results. With fine tuning of model constants, even for complicated cases reasonable results can be obtained. In industrial applications one has to compute more or less very similar topologies. Once problems have been detected with RANS models for particular cases they can be *ad hoc* modified for special interest. Which is a quick and very efficient procedure but suffers from reasonable physical background.
Nevertheless there are typical turbulent flows where RANS models fail substantially. One of these is the massively separated flow from curved surfaces, which is a typical situation in external and internal aerodynamics where the flow separates from from plane wings at high angle of attack of from compressor blades at the leading edge. The so called large eddy simu-

lation (LES) tries to bridge the gap between DNS and RANS by modeling the small turbulent structures and resolving the large ones. This is done by filtering the transport equations, which seems at first to be an adequate procedure, but has been shown to be too costly for higher Reynolds number engineering applications [43] in terms of computational effort; hence this approach remains unfeasible except for some very basic turbulent flow cases.

The motivation of the present work is to develop a turbulence model which, on the one hand is accurate enough for massively separated flows, and on the other hand is closer to RANS than to DNS in terms of required computational resources. The approach taken to achieve these goals was to introduce the scale adaptive simulation concept [35] into a second moment closure RANS model. By doing so the RANS model can be triggered to resolve turbulent flow structures without the explicit use of grid parameters, but rather by using the ratio between first and second velocity derivatives. It will be shown that the new model can be used with much coarser grids than LES demands, due to the continuous and variable shift between the resolved and the modeled part. In fact often the same grid can be used as the RANS simulation would need but extended in a relatively coarse manner in third dimension. Since turbulent structures are resolved, the simulation with this new model must be carried out time dependent. As the grid is much coarser than for LES or DNS, also larger timesteps can be used. It will be shown that by coupling the SAS concept with a second moment closure model, also called Reynolds stress model (RSTM or RSM), and implementing slight modifications and calibration, this newly developed model is able to switch also under quasi stable flow conditions without separations, like for example the turbulent flow in a plane channel, in a structure resolving mode. This distinguishes its features from the SAS concept introduced by Menter and Egorov [35].

The final part of this work addresses a modified RANS model which is able to handle massively separated flows by performing steady state simulations, often on two-dimensional grids. The modifications are not *ad hoc* and the derivation together with the underlying idea will be presented. It consists of a different approach in deriving a length-scale supplying equation and basically makes use of the term introduced in the SAS concept but with an opposite sign. It will be shown that with this RANS model important turbulent flow cases which are known to be well computed by the baseline RANS model, are not influenced by the proposed modifications.

2 Theoretical Background

The computations for this dissertation have been done with OpenFOAM [41], an open source finite volume program package. First a short description of the finite volume method is given, accompanied by the presentation of the Jakirlic-Hanjalic Reynolds stress model (JH-RSM [19]). The latter is the starting point for the turbulence modeling that is going to be the focus of the following chapters.

2.1 Basics of the finite volume-based numerical method

An incompressible flow of a Newtonian fluid (which is the only type accounted for in this work) can be described by the following form of the Navier-Stokes equations

$$\frac{\partial U_i}{\partial t} + U_j \frac{\partial U_i}{\partial x_j} = -\frac{1}{\rho}\frac{\partial P}{\partial x_i} + \frac{\partial}{\partial x_j}\left(\nu \frac{\partial U_i}{\partial x_j}\right), \tag{2.1}$$

in conjunction with the continuity equation

$$\frac{\partial U_i}{\partial x_i}, \tag{2.2}$$

with U_i and P_i representing instantaneous velocity and pressure fields. The flow field, that has to be computed numerically in a fluid mechanics application, can be described accurately by the Eulerian approach, as it gives details of the flow characteristics on the vital points. The result is a set of coupled differential equations describing the problem in any desired point. The finite volume method basically transforms those coupled differential equations into a set of coupled algebraic equations on a discretized domain. At first the differential equations are integrated over each control volume and the Gauss theorem is applied on them. Secondly the surface and volume integrals are approximated and finally the evolved coupled algebraic equation system is solved by applying appropriate methods. These

methods themselves often do some mathematical transformations as a preconditioning step on the matrices system, in which the coupled algebraic equations have been transformed, and finally solve the matrices system in an iterative procedure. As a short example a scalar transport equation (for example the heat transport equation) will be transformed from its initial differential form in its algebraic form. This is done on a discretized control volume mimicking a part of the whole domain of interest shown in Fig. 2.1, which has been taken from [13]. For the control volume the compass notation is used to distinguish faces and and edges. For distinguishing neighboring controlvolumes the compass notation is used as well. Φ is the scalar of interest, while it is assumed that all the other quantities are already known. The transport equation for Φ has the following differential

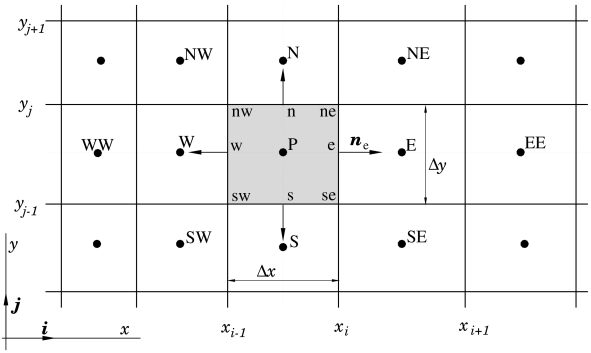

Figure 2.1: Discretized computational domain

form:

$$\frac{\partial}{\partial x_i}\left(\rho U_i \Phi - \alpha \frac{\partial \Phi}{\partial x_i}\right) = f. \tag{2.3}$$

In the next step eq. 2.3 can be integrated on an arbitrary control volume, like that one shown in Fig. 2.1, which results in the following formula:

$$\int_S \left(\rho U_i \Phi - \alpha \frac{\partial \Phi}{\partial x_i}\right) n_i dS = \int_V f dV. \tag{2.4}$$

Here n_i are the components of the unit vector normal to the surface and S the surface. The surface integral can now be split into surface integrals

over each face $S_c(c = e, w, n, s)$ of the control volume:

$$\sum_c \int_{S_c} \left(\rho U_i \Phi - \alpha \frac{\partial \Phi}{\partial x_i} \right) n_{ci} dS_c = \int_V f dV. \tag{2.5}$$

By summing up eq. 2.5 can be divided into convective and diffusive fluxes through the cell faces with

$$F_c^C = \int_{S_c} (\rho \; U_i \Phi) \, n_{ci} dS_c \tag{2.6}$$

being the convective one, and

$$F_c^D = - \int_{S_c} \left(\alpha \frac{\partial \Phi}{\partial x_i} \right) n_{ci} dS_c \tag{2.7}$$

being the diffusive flux. The surface integrals and the volume integral have to be approximated in a next step by averages of the integrands at the control volume faces and further by finding expressions for the face values via midpoint values of the cells. The detailed procedure can be found at [13] or [49] and is described only briefly here. The integrals can be approximated for example through the midpoint rule which leads to

$$F_c^C \approx \rho \; U_i n_{ci} \delta S_c \Phi_c \tag{2.8}$$

for the convective flux, and

$$F_c^D \approx -\alpha n_{ci} \delta S_c \left(\frac{\partial \Phi}{\partial x_i} \right)_c \tag{2.9}$$

for the diffusive fluxes. By applying the central difference scheme (CDS) which uses linear interpolation for the approximation, Φ_c in the convective term can be expressed by values in neighboring cell points. For the face S_e, in which Φ_e is approximated by Φ_P and Φ_E, assuming an equidistant grid, this reads:

$$\frac{1}{2} \Phi_E + \frac{1}{2} \Phi_P. \tag{2.10}$$

Similarly for the diffusive term:

$$\left(\frac{\partial \Phi}{\partial x} \right)_e \approx \frac{\Phi_E - \Phi_P}{x_E - x_P}. \tag{2.11}$$

As already mentioned CDS is not the only way to come to an approximation. It is of second order accuracy but can induce numerical instabilities in the solution system [49]. Another scheme has therefore gained popularity namely the upwind differencing scheme (UDS) which is insensitive to numerical instabilities but only of first order accuracy. Hybrid numerical schemes try to couple the advantages of the both schemes mentioned above by weighting them. By applying the approximation methods to all terms a solution system develops containing algebraic equations which are coupled through the constraint, that each control volume or cell has to be aligned with each side either to other cells or to boundary regions. The equation system can be solved iteratively by using appropriate methods.

With the methods presented above, basically every flow problem can be theoretically computed. The accuracy of the result depends strongly on the structure of the discretized domain, which is named computational mesh. One key point is the number of mesh gridpoints, on which the equations system is solved. A very coarse mesh leads to insufficient accuracy while a fine mesh leads to an increase in computational effort. For laminar flow problems the increase in computational effort is limited since the flow itself does not vary strongly in location and time. As a consequence not that many gridpoints are needed. Those flows can be computed relatively fast and accurate nowadays. The main problem however is that the flow in relevant mechanical applications is mostly turbulent, which means always three-dimensional, chaotic, unsteady and highly diffusive. This behavior negates the possibility to solve the equation system directly as described above. To obtain a reasonably accurate solution all the flow features have to be captured. A turbulent flow varies strongly in location and time. Therefor a very fine mesh and very fine timesteps in the numerical procedure are needed. For complex flows highly relevant for industrial applications, a DNS won't be feasible for many decades [42] [43]. Thus another approach has gained a lot of popularity, the so called Reynolds-averaged Navier-Stokes procedure. RANS is based on the Reynolds decomposition [43] [47] of flow field quantities (for example the velocity U_i) in an fluctuating u_i and averaged $\overline{U}_i$ part:

$$U_i = \overline{U}_i + u_i. \tag{2.12}$$

This decomposition is shown in Fig. 2.2 as an example for a turbulent channel flow computation.

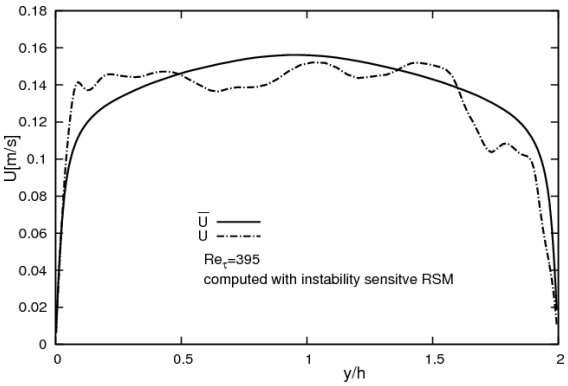

Figure 2.2: Turbulent channel flow with $Re_\tau = 395$, instantaneous and mean velocity profile

2.2 Turbulence modeling

If the decomposition mentioned above is inserted in the momentum equation, and the equation as a whole is averaged again, a slightly different one is obtained with a similar structure like the baseline momentum equation but containing one extra term $\frac{\partial \overline{u_i u_j}}{\partial x_j}$ that results out of the averaging procedure. It reads:

$$\frac{\partial \overline{U}_i}{\partial t} + \overline{U}_j \frac{\partial \overline{U}_i}{\partial x_j} = -\frac{1}{\rho}\frac{\partial \overline{P}}{\partial x_i} + \frac{\partial}{\partial x_j}\left(\nu \frac{\partial \overline{U}_i}{\partial x_j} - \overline{u_i u_j}\right). \tag{2.13}$$

From now on the averaged velocity $\overline{U}_i$ will be denoted as U_i, while the instantaneous one will be explicitly denoted for the remainder of this work. Since $\frac{\partial \overline{u_i u_j}}{\partial x_j}$ consists of unknown quantities, namely the so called Reynolds stresses $\overline{u_i u_j}$, it has to be modeled to close the equation set. This closing procedure, which will be later discussed in more detail in connection with the modifications of the length scale supplying equation, is called turbulence modeling. In the past a great variety of closure approaches have been devised. Maybe one of the most widely used turbulence models is the standard $k\epsilon$ model, either with wall functions or integration of the equations up to the walls, which build up the boundaries of the domain, in which the flow has to be computed. The $k\epsilon$ model consists of two extra equations, where k stands for the turbulent kinetic energy and ϵ for its dissipation

rate [29] [31]. Out of these two quantities the Reynolds stresses $\overline{u_i u_j}$ are constructed via the Boussinesq assumption [43]

$$\overline{u_i u_j} = \frac{2}{3} k \delta_{ij} - \nu_t \left(\frac{\partial U_i}{\partial x_j} + \frac{\partial U_j}{\partial x_i} \right). \tag{2.14}$$

Here ν_t stands for the turbulent viscosity, which is an artifact introduced to close the model equations. ν_t can be expressed in terms of k and ϵ as for example $\nu_t = C_\mu \frac{k^2}{\epsilon}$, where C_μ is just a model constant. It may not be the most sophisticated model but due to its robustness and simplicity it is one of the most widely used. Another approach to model $\overline{u_i u_j}$ inside the RANS equation, is to directly solve transport equations for them, which is then called Reynolds stress transport model or Reynolds stress model. As the Boussinesq assumption is not needed and the Reynolds stress anisotropy can be obtained directly through solving the equations, this closing procedure is by definition more accurate then the formerly explained two equation turbulence model. However is has to be pointed out that some terms in the Reynolds stress transport equations are unclosed and it is not easy to find generally valid modeling approaches for them. Instead of solving two extra equations, seven extra equations (six stress equations, since $\overline{u_i u_j}$ is symmetric, and one length scale supplying equation) have to be solved, which increases calculation time. The strong coupling between the six stress equations and the fact that there is no direct relationship between the derivatives of the Reynolds stresses and the second derivatives of the velocity components, which dampen out numerical instabilities [8] (the Boussinesq assumption builds up a relationship between derivatives of the Reynolds stresses and second derivatives of the velocity components), leads to slow convergence of the computation. Nevertheless, if care is taken in modeling with respect to the correct behavior of each term inside the stress equations and length scale supplying equation, the Reynolds stress modeling gives more accurate results in a lot of cases, which strongly depend on Reynolds stress anisotropy [11] [19]. That is the reason why the JH-RSM [19], which will be introduced next, was chosen as a starting point for this work. This particular Reynolds stress model has been build up by analyzing each term out of the correct Reynolds stress equation and the correct equation for ϵ [19], and by applying proper calibrated models, that have been tested in an *a priori* manner for different cases [19], for those terms. This procedure is called modeling in term by term manner with *a priori* testing. It can be a very useful tool, but it has to be clear that, if the terms in the Reynolds-averaged momentum equation

and the turbulence equations, except the term of interest, are frozen, with so to say correct quantities out of a direct numerical simulation (DNS) or an experiment, it is not ensured that the term of interest has the same value or shape, as if all the equations would have been solved in a coupled manner with different models for the other terms. Nevertheless, this represents the state of the art practice in turbulence modeling at least for RANS models, which in general include a rising number of terms the more sophisticated they are. The Reynolds stress equations of the JH-RSM have the following composition:

$$\begin{aligned}\frac{\mathrm{D}\overline{u_i u_j}}{\mathrm{D}t} &= \frac{\partial}{\partial x_k}\left[\left(\frac{1}{2}\nu\delta_{kl} + C_s\frac{k}{\epsilon^h}\overline{u_k u_l}\right)\frac{\partial\overline{u_i u_j}}{\partial x_l}\right] \\ &\quad - \left(\overline{u_i u_k}\frac{\partial U_j}{\partial x_k} + \overline{u_j u_k}\frac{\partial U_i}{\partial x_k}\right) + \Phi_{ij} - \epsilon^h_{ij},\end{aligned} \tag{2.15}$$

while the dissipation equation is written in its homogeneous form [20] [19]:

$$\begin{aligned}\frac{\mathrm{D}\epsilon^h}{\mathrm{D}t} &= -\epsilon^h_{ij}\frac{\partial U_i}{\partial x_j} - \overline{u_i u_j}\frac{\partial U_i}{\partial x_j}\frac{\epsilon^h}{k} \\ &\quad - 2\nu\left(\frac{\partial\overline{u_i u_k}}{\partial x_l}\frac{\partial^2 U_i}{\partial x_k\partial x_l} + C_{\epsilon 3}\frac{k}{\epsilon^h}\frac{\partial\overline{u_k u_l}}{\partial x_j}\frac{\partial U_i}{\partial x_k}\frac{\partial^2 U_i}{\partial x_j\partial x_l}\right) \\ &\quad - C_{\epsilon 2}f_\epsilon\frac{\epsilon^h\tilde{\epsilon}^h}{k} + \frac{\partial}{\partial x_k}\left[\left(\frac{1}{2}\nu\delta_{kl} + C_\epsilon\frac{\epsilon^h}{k}\overline{u_k u_l}\right)\frac{\partial\epsilon^h}{\partial x_l}\right],\end{aligned} \tag{2.16}$$

with Φ_{ij} being the pressure strain tensor and ϵ^h_{ij} the dissipation tensor.
Another turbulence model which is important for this work, but has not gained so much popularity in the past, is Rotta's $k-kL$ model [48] [35]. In this particular two equation model kL plays the role of an effective length scale, which is needed to model the turbulent viscosity ν_t. Rotta went a different way in modeling $kL = \frac{3}{16}\int_{-\infty}^{\infty} R_{ii}(\vec{x}, r_y)dr_y$ (assuming flows with dominant shear strain in y-direction), namely by deriving an exact transport equation for kL with L being the integral length scale and $R_{ii}(\vec{x}, r_y)$ being the sum of the diagonal of the two-point correlation tensor, R_{ij} [35]. The transport equation for kL has two production terms, the first one being

$$-\frac{3}{16}\frac{\partial U(\vec{x})}{\partial y}\int_{-\infty}^{\infty} R_{21}dr_y \tag{2.17}$$

and the second one

$$-\frac{3}{16}\int_{-\infty}^{\infty}\frac{\partial U(\vec{x}+r_y)}{\partial y}R_{12}dr_y, \tag{2.18}$$

while most of the other two equation models have only one. To simplify the second part of the production, Rotta used the Taylor expansion series for that term, leading to:

$$\begin{aligned}\int_{-\infty}^{\infty}\frac{\partial U(\vec{x}+r_y)}{\partial y}R_{12}dr_y = &\frac{\partial U(\vec{x})}{\partial y}\int_{-\infty}^{\infty}R_{12}dr_y \\ &+\frac{\partial^2 U(\vec{x})}{\partial y^2}\int_{-\infty}^{\infty}R_{12}r_y dr_y \\ &+\frac{1}{2}\frac{\partial^3 U(\vec{x})}{\partial y^3}\int_{-\infty}^{\infty}R_{12}r_y^2 dr_y + ...\end{aligned} \tag{2.19}$$

He then argued that the resulting term, which contains the second velocity derivative can be skipped, since in homogeneous shear flow R_{12} is antisymmetric with respect to r_y. Thus the second term in the production of kL has been modeled by using the third term in the Taylor expansion. This is a large drawback for that model, since the third velocity derivative brings high numerical instability to the equation system. Nevertheless, Rotta's model is very important and useful in understanding the scale adaptive simulation concept introduced by Menter and Egorov [35]. They argued, that in homogeneous shear flows the second velocity derivative is zero anyway and thus does not have to be skipped in the Taylor expansions and, in fact is in many cases the leading term compared to the third velocity derivative [35]. Therefore the term is modeled in the following way:

$$\int_{-\infty}^{\infty}R_{12}r_y dr_y = -const\cdot\overline{u'v'}L^2\left(\frac{1}{\kappa}\frac{1}{\partial U/\partial y}\cdot L\right). \tag{2.20}$$

The von Karman length scale, here shown in boundary layer form, also includes the second velocity derivative:

$$L_{vK} = \kappa\left|\frac{\partial U/\partial y}{\partial^2 U/\partial y^2}\right|. \tag{2.21}$$

Menter and Egorov rewrote the mathematical formulation in terms of the von Karman length scale, which results in an expression containing the ratio between second and first velocity derivatives and with the shear stress modeled in terms of the production of the turbulent kinetic energy P_k

$$-\frac{3}{16}\frac{\partial^2 U(\vec{x})}{\partial y^2}\int_{-\infty}^{\infty} R_{12} r_y dr_y = -const \cdot Pk \cdot \frac{\Psi}{k}\left(\frac{L}{L_{vk}}\right) \tag{2.22}$$

where $\Psi = kL$. This is now inserted into the second part of the production in the kL equation. The second part modeled in this manner is a sink term in the kL equation, reducing in fact kL. As a reminder, the turbulent viscosity, which directly enters the averaged momentum equation, is written in terms of k and kL

$$\nu_t = C_\mu^{1/4}\frac{kL}{\sqrt{k}} \tag{2.23}$$

As can be seen, the sink term in the kL equation reduces the turbulent viscosity, not so much by directly reducing kL, but more through a reduction of the ratio between kL and k. It has to be noticed that also k is reduced by a lower kL in the following manner:

$$\frac{\partial k}{\partial t} + \frac{\partial (U_j k)}{\partial x_j} = P_k - \frac{k^2}{\Phi} + \frac{\partial}{\partial x_j}\left(\frac{\nu_t}{\sigma_k}\frac{\partial k}{\partial x_j}\right) \tag{2.24}$$

where the transport equation for k has been rewritten in terms of $\Phi = \sqrt{k}L$ instead of Ψ [35]. Fig. 2.2 shows an instantaneous velocity profile compared to a time or ensemble averaged one (both obtained with the eddy-resolving Reynolds stress model which will be presented later in that work), for the well-known testcase of the turbulent channel flow with a friction Reynolds number $Re_\tau = 395$ ($Re_\tau = \frac{u_\tau h}{\nu}$ with u_τ being the friction velocity and h the channel half height) [43] [18] [17]. As can be seen, the ratio between second and first velocity derivatives increases for the unsteady velocity profile due to its high bending, which consequently decreases the turbulent viscosity. The averaged momentum equation handles a dramatically reduced turbulent viscosity by starting to resolve structures of the turbulence in the flow, since in the limit when ν_t tends to zero for lets say highly unsteady velocity profiles the averaged momentum equation tends to the non-averaged momentum equation. This means that the simulation changes its behavior from a RANS modeled one more to a direct numerical simulation. Menter argues in latest versions of $k\omega$-SST-SAS that the second term should be

modeled slightly different. Since Rotta claims that R_{12} should vanish for statistical homogeneous turbulence due to the symmetric behavior with respect to r_y (the product $R_{12}r_y$ is asymmetric and the integral becomes zero, as can be seen in Fig. 2.3 taken out from [35]), Menter and Egorov

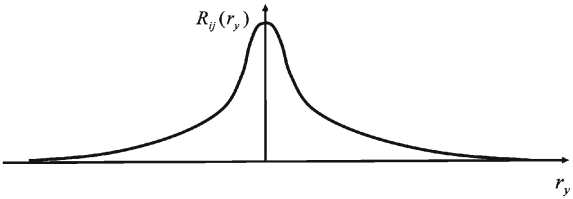

Figure 2.3: Shear component of two-point correlation tensor for homogeneous turbulent flow

proposed to introduce one more Ratio of L/L_{vk} as an observing term for homogeneous turbulence with the model for the extra production being finally:

$$-\frac{3}{16}\frac{\partial^2 U(\vec{x})}{\partial y^2}\int_{-\infty}^{\infty} R_{12}r_y dr_y = -const \cdot Pk \cdot \frac{\Psi}{k}\left(\frac{L}{L_{vk}}\right)^2 \tag{2.25}$$

The second derivative of the mean velocity goes to zero in homogeneous turbulence. The modification may be helpful in the case of steady RANS simulations or simulations with slight unsteadiness (ensembles with large time scales) to detect the direction of homogeneous turbulence but not necessarily for URANS simulations with very high unsteadiness and no instantaneous homogeneous direction with respect to turbulence quantities, which will be discussed more in detail in a later coming chapter.

3 Derivation of an eddy-resolving Reynolds stress model (RSM)

In this chapter different modifications in the JH-RSM model will be shown which will make it sensitive to flow unsteadiness with the help of the aforementioned SAS term. The notation IS-RSM refers to an instability sensitive Reynolds stress model in conjunction with the eddy-resolving concept presented by Menter and Egorov [35]. But first of all it has to be clarified why the SAS term should be combined with a sophisticated but numerically complicated RSM model. The following motivating reasons can be given:

- The RSM is undoubtedly the better background RANS model which can be important in the case when coarse grids are used or the walls are approached, since then the turbulent structure resolving mode increasingly vanishes due to the ratio of second to first velocity derivatives.
- It is expected, due to more coupled time dependent equations and with the lack of a damping artificial eddy viscosity that the Reynolds stress model can be forced to change more quickly to a structure resolving mode with the help of the SAS term and, hopefully, it resolves turbulent structures also for cases which have been beyond the reach of the $k\omega$-SST-SAS, like the turbulent channel flow or the inlet duct of a 3D diffuser.
- And finally the case where the model cannot be triggered to the structure resolving mode because of the very local unstable flow situation and fixed inlet boundary conditions which are not varying in time [35], the RSM model is able to handle more cases accurately.

3.1 Transformation from ϵ^h to ω^h

The most practical way to make the SAS concept transferable to the JH-RSM, is to directly insert it into one of the JH-RSM model equations. Since the original JH-RSM uses the ϵ^h equation as scale supplying equation but

the SAS term is in conjunction with the ω equation of the $k\omega$-SST model some pre-steps are needed, before inserting the triggering term into the model. These steps include the transformation of ϵ^h to ω^h by using the direct relationship

$$\omega^h = \frac{\epsilon^h}{k} \quad \text{and} \quad \frac{\mathrm{D}\omega^h}{\mathrm{D}t} = \left(\frac{\mathrm{D}\epsilon^h}{\mathrm{D}t} k - \frac{\mathrm{D}k}{\mathrm{D}t} \epsilon^h \right) \frac{1}{k^2} \tag{3.1}$$

and simplifications which make the transformation easier and more convenient in terms of numerical behavior. The major simplification is hereby the application of the simple gradient approach inside the turbulent diffusion terms in the underlying ϵ^h and k equations instead of the general gradient one, leading to

$$\frac{\mathrm{D}\epsilon^h}{\mathrm{D}t} = \frac{\partial}{\partial x_k} \left[\left(\frac{1}{2}\nu + \frac{\nu_t}{\sigma_\epsilon} \right) \frac{\partial \epsilon^h}{\partial x_k} \right] + C_{\epsilon 1} \frac{\epsilon^h}{k} P_k - C_{\epsilon 2} \frac{\epsilon^h \epsilon^h}{k} + P_{\epsilon,3} \tag{3.2}$$

and

$$\frac{\mathrm{D}k}{\mathrm{D}t} = \frac{\partial}{\partial x_k} \left[\left(\frac{1}{2}\nu + \frac{\nu_t}{\sigma_k} \right) \frac{\partial k}{\partial x_k} \right] + P_k - \epsilon^h, \tag{3.3}$$

with $\sigma_\epsilon = \sigma_k = \sigma = 1.1$. Nevertheless, the turbulent viscosity has been modeled in terms of Reynolds stress anisotropy A

$$\nu_t = 0.144 \cdot A \cdot k^{1/2} \cdot min \left[10 \left(\frac{\nu^3}{k\omega^h} \right)^{1/4}, \frac{k^{1/2}}{\omega^h} \right] \tag{3.4}$$

and has proven good approximation behavior, at least in turbulent channel flow [2]. Finally the resulting ω^h equation reads:

$$\begin{aligned} \frac{\mathrm{D}\omega^h}{\mathrm{D}t} = & \frac{\partial}{\partial x_k} \left[\left(\frac{1}{2}\nu + \frac{\nu_t}{\sigma} \right) \frac{\partial \omega^h}{\partial x_k} \right] + (C_{\epsilon 1} - 1) \frac{\omega^h}{k} P_k \\ & - (C_{\epsilon 2} - 1)\, \omega^h \omega^h + \frac{2}{k} \left(\frac{1}{2}\nu + \frac{\nu_t}{\sigma} \right) \frac{\partial \omega}{\partial x_k} \frac{\partial k}{\partial x_k} + \frac{1}{k} P_{\epsilon,3}. \end{aligned} \tag{3.5}$$

With the first term on the right hand side being viscous and turbulent diffusion, the second one production, the third destruction, the fourth cross diffusion and the last one production due to mean velocity gradients which is a near wall term and absent in high Reynolds number versions of Reynolds stress models. It reads:

$$P_{\epsilon,3} = -2\nu \left(\frac{\partial \overline{u_i u_k}}{\partial x_l} \frac{\partial^2 U_i}{\partial x_k \partial x_l} + C_{\epsilon 3} \frac{k}{\epsilon^h} \frac{\partial \overline{u_k u_l}}{\partial x_j} \frac{\partial U_i}{\partial x_k} \frac{\partial^2 U_i}{\partial x_j \partial x_l} \right). \tag{3.6}$$

This specific term bears a lot of numerical instability potential, due to combinations of first and second derivatives of the velocity and the Reynolds stresses. It will be remodeled later in the context of using the IS-RSM with high order numerical schemes.

3.2 Full model calculations with ω^h based JH-RSM

Since an adequate transport equation for ω^h has been derived in the last section, test simulations on simple cases, where the results are known to be good with the use of Reynolds stress models, are the logical next step. However before doing so some recalibration of the model constants in the ω^h-equation is needed, which is the direct outcome of the complicated wall boundary condition for ω^h that goes to infinity. The ϵ^h-equation close to walls reads in boundary layer form:

$$\frac{1}{2}\nu\frac{\partial^2\epsilon^h}{\partial y^2} = f_e C_{\epsilon 2}\frac{\widetilde{\epsilon}^h\epsilon^h}{k}. \tag{3.7}$$

Since $C_{\epsilon 2}$ has been calibrated with the homogeneous isotropic decay testcase, it is not insured that it fulfills the requirements of the asymptotic wall behavior of ϵ^h, which is:

$$\epsilon^h = \frac{1}{2}\nu\frac{\partial^2 k}{\partial y^2}. \tag{3.8}$$

This expression is the direct outcome of the turbulent kinetic energy equation in boundary layer form, which has been analyzed for the close to the wall behavior. The leading order term for the asymptotic wall behavior of ϵ^h is constant in the direct wall vicinity, but since in the ϵ^h-equation the second derivative balances the destruction term, the third term in the asymptotic behavior is the important one, which cannot be easily determined in its constants. This is actually not true for the ω^h-equation. The asymptotic value of ω^h is approximately known in terms of the λ wall boundary condition (introduced in [21]), with λ being the Taylor microscale:

$$\omega^h_{wall} = \frac{\epsilon^h_{wall}}{k_P} = \nu\frac{1}{y_P^2}. \tag{3.9}$$

P denotes the first gridpoint close to the wall. The ω^h wall boundary condition can be derived two times to get the value for the second derivative, which describes the molecular viscous diffusion in the boundary layer form of the ω^h-equation. It reads in a form, where only those terms have been inserted, which cannot be neglected very close to the walls:

$$-\frac{1}{2}\nu\frac{\partial^2\omega^h}{\partial y^2} = C_{cr}\nu\frac{1}{k}\frac{\partial\omega^h}{\partial y}\frac{\partial k}{\partial y} - (C_{\epsilon 2}-1)\,\omega^h\omega^h. \tag{3.10}$$

As a direct consequence of $\omega^h_{wall} = \nu\frac{1}{y_P^2}$ and $k_P = \frac{1}{2}(b_1b_1 + b_3b_3)y_P^2$ it follows that

$$-\frac{1}{2}\nu\frac{\partial^2\omega^h}{\partial y^2} = -3.0\frac{\nu^2}{y^4}, \quad (C_{\epsilon 2} - 1)\,\omega^h\omega^h = 0.8\frac{\nu^2}{y^4} \tag{3.11}$$

and

$$C_{cr}\nu\frac{1}{k}\frac{\partial\omega^h}{\partial y}\frac{\partial k}{\partial y} = -C_{cr}4.0\frac{\nu^2}{y^4}. \tag{3.12}$$

From eq. 3.12 $C_{cr} = 0.55$ is obtained. The boundary condition is set for the first gridpoint since directly at the wall $\omega^h = \frac{\epsilon^h}{k}$ has by definition a boundary condition of infinite. Accompanied by that is a zero gradient boundary condition for the explicit terms containing gradient operators.
Fig. 3.1 shows the behavior of the normalized specific dissipation ω^{h+} close to the wall for the turbulent channel flow with $Re_\tau = 395$ obtained with the Reynolds stress turbulence model and the DNS by Iwamoto et al. [17] and Iwamoto [18], while two different values for C_{cr} have been tested. $C_{cr} = 0.55$ obtained from the asymptotic wall behavior and $C_{cr} = 1.0$ obtained by the transformation procedure from ϵ^h and k to ω^h-equation. As can be seen in Fig. 3.1 with $C_{cr} = 1.0$ ω^{h+} is underestimated. While this seems not too dramatic in Fig. 3.1, Fig. 3.2, which is just a zoom into Fig. 3.1, reveals a certainly high underestimation. With $C_{cr} = 0.55$ the shape as well as the values of ω^{h+} close to the wall match the DNS. This becomes even more obvious, if the same graph is shown for a refined mesh for the same turbulent channel flow. By clustering more points in the viscous sublayer, ω^{h+} out of the simulation with the Reynolds stress model and $C_{cr} = 0.55$ follows the DNS very accurately, as can be seen in Fig. 3.3.
One further point has to be clarified. The constant in front of the turbulent cross diffusion term $2.0\frac{\nu_t}{\sigma}\frac{\partial\omega^h}{\partial x_k}\frac{\partial k}{\partial x_k}$, which is basically $2.0/\sigma = 2.0/1.1$ comes from the direct transformation of the k and ϵ^h eq. to the ω^h-eq. by using the same $\sigma_k = \sigma_\epsilon$, which is a simplification. Since the constants in front of the viscous and turbulent diffusion terms should not be recalibrated, the turbulent cross diffusion allows to leave them untouched and at the same time capture the diffusion process correctly, if calibrated properly. One possible testcase for setting up the constant is the turbulent mixing layer, where the oncoming flow is divided into two parts with two different freestream velocities, a higher one and a lower one. With some distance to the inlet the flow starts to mix out which is a continuous process. Experiments for such a testcase have been made by Spencer [50] [38]. Fig.

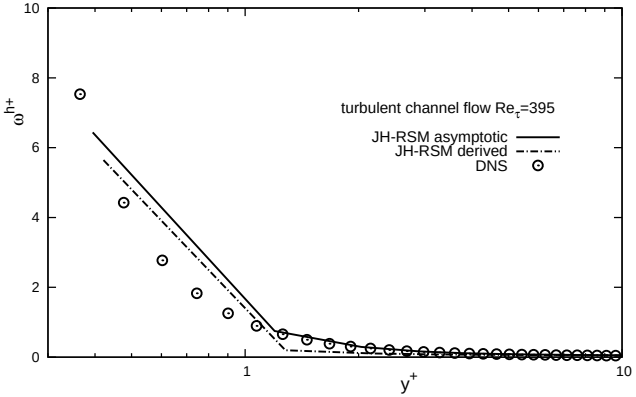

Figure 3.1: Close to the wall behavior of ω^{h+} for turbulent channel flow with $Re_\tau = 395$ - coarse grid

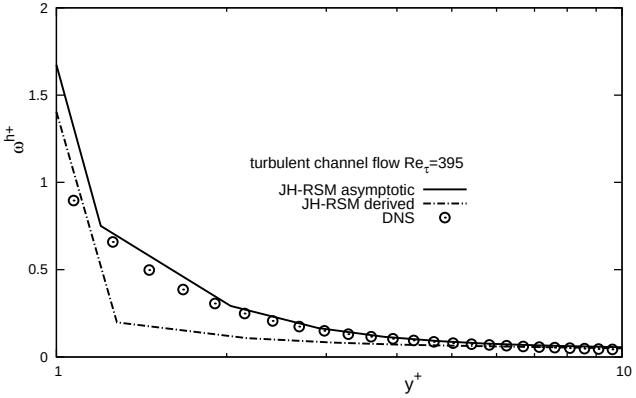

Figure 3.2: Close to the wall behavior of ω^{h+} for turbulent channel flow with $Re_\tau = 395$ - coarse grid, zoom in

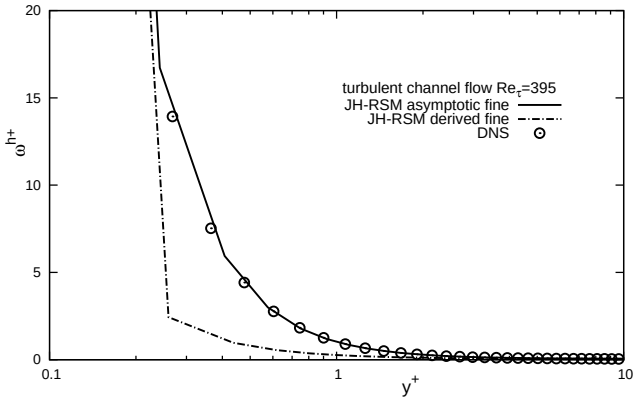

Figure 3.3: Close to the wall behavior of ω^{h+} for turbulent channel flow with $Re_\tau = 395$ - fine grid

3.4 shows the computational domain presenting the already solved mean streamwise velocity, just to give the reader a better impression. The flow is entering the domain from the left with two different velocity block profiles and an imposed velocity gradient in a small area between them. According to Wilcox [53], the mixing layer is an adequate testcase for setting up the constant in front of the turbulent cross diffusion term, by matching the spreading rate $\frac{\partial \delta}{\partial x}$ of the mixing layer, where $\delta = y_{0.9} - y_{0.1}$. $y_{0.1}$ and $y_{0.9}$ are hereby the positions of $U = U_2 + 0.1 \cdot \Delta U$ respectively $U = U_2 + 0.9 \cdot \Delta U$ (U_2 is the lower inlet velocity). Table 3.1 shows the experimental and the com-

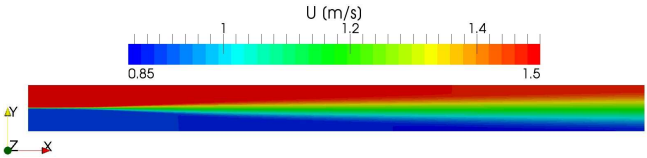

Figure 3.4: Streamwise mean velocity for turbulent mixing layer

puted spreading rates with 2/4 and 2/1.1 as chosen constants. Obviously with the derived value 2/1.1, the spreading rate is highly underestimated compared to the experiments, while 2/4 gives a spreading rate very close to the reference data. Furthermore, this value in relation to the constant

in front of the turbulent diffusion, so basically $\frac{0.25}{0.91} \approx 0.275$, is close to the results Wilcox reached [53], when he calibrated a ratio of $\frac{1/8}{3/5} \approx 0.208$. The ω^h with the calibrated (based on the mixing layer testcase and the

	Experiments	JH-RSM ($\nu_t/4$)	JH-RSM ($\nu_t/1.1$)
Spreading rates	0.0328	0.0315	0.022

Table 3.1: Spreading rates for turbulent mixing layer in self similar region

asymptotic wall behavior) cross diffusion terms has the following form:

$$\frac{\mathrm{D}\omega^h}{\mathrm{D}t} = \frac{\partial}{\partial x_k}\left[\left(\frac{1}{2}\nu + \frac{\nu_t}{\sigma}\right)\frac{\partial \omega^h}{\partial x_k}\right] + (C_{\epsilon 1} - 1)\,\frac{\omega^h}{k}P_k - (C_{\epsilon 2} - 1)\,\omega^h\omega^h + \frac{2}{k}\left(0.55\frac{1}{2}\nu + \frac{\nu_t}{4}\right)\frac{\partial \omega}{\partial x_k}\frac{\partial k}{\partial x_k} + \frac{1}{k}P_{\epsilon,3}. \quad (3.13)$$

3.2.1 Turbulent channel flow

The turbulent channel flow describes a plane channel through which a turbulent flow is driven by a pressure gradient. As accounted for by literature [19] [44] [30], a lot of RANS turbulence models provide good results for a number of flow quantities for this specific case. In the following, the new ω^h-based model will be compared to DNS data of Iwamoto et al. [18] and Jimenez and Hoyas [24] to prove its ability to give comparably good results. Fig. 3.5 shows the outcome in terms of the normalized mean streamwise velocity profile for the turbulent channel flow with $Re_\tau = 395$. As can be seen the linear wall distance law $U^+ = U/u_\tau = y^+$ ($y^+ = yu_\tau/\nu$ being the normalized wall distance) for $y^+ < 5$ and the logarithmic wall distance law $U^+ = \frac{1}{\kappa}\ln y^+ + 5.1$ for $30 < y^+ < 100$ are properly calculated. Fig. 3.6 shows the normalized Reynolds stresses, actually the normal components of the stress tensor, which are also properly calculated in peak values and distribution, by the ω^h based JH-RSM. In Fig. 3.7 the normalized homogeneous dissipation ϵ^{h+} is plotted over y^+ on two different grids, with correct values close to the wall on both grids but the first gridpoint, which underlines the adaptivity of the λ boundary condition, that was found to be valid even for relatively coarse grids up to $y^+ \approx 4$ [21]. The slightly underestimated value of ϵ^{h+} in the first gridpoint is not the consequence of ω^{h+} in this point, since ω^{h+} is by definition of the boundary condition correct, but because of an underestimation of k^+, the normalized turbulent

kinetic energy, as can be seen in Fig. 3.8. k^+ is somewhat to low due to the wrong asymptotic behavior in the $\overline{vv}$ and the $\overline{ww}$ stress component. The same can be said for ϵ^{h+} for the higher Reynolds number ($Re_\tau = 2000$) as shown in Fig. 3.9.

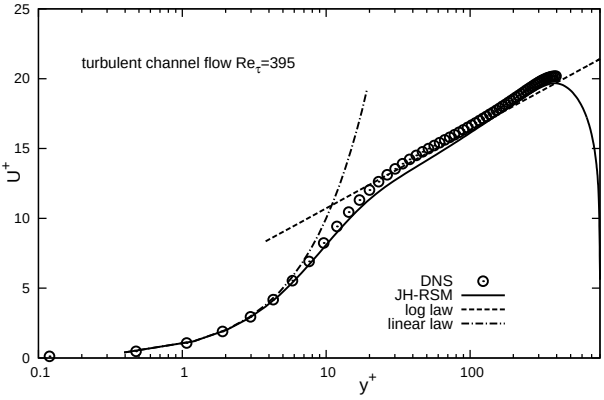

Figure 3.5: Normalized streamwise velocity for turbulent channel flow with $Re_\tau = 395$

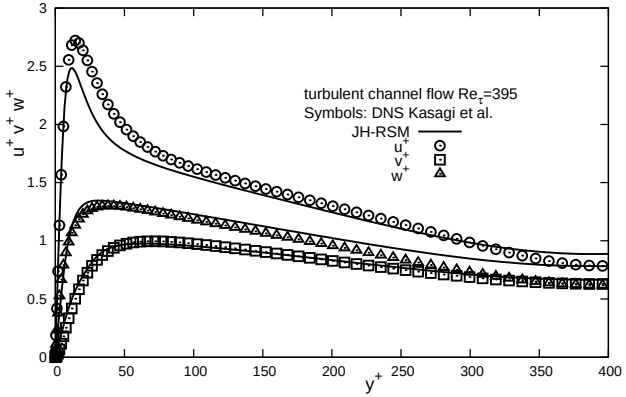

Figure 3.6: Normalized Normal stress components for turbulent channel flow with $Re_\tau = 395$

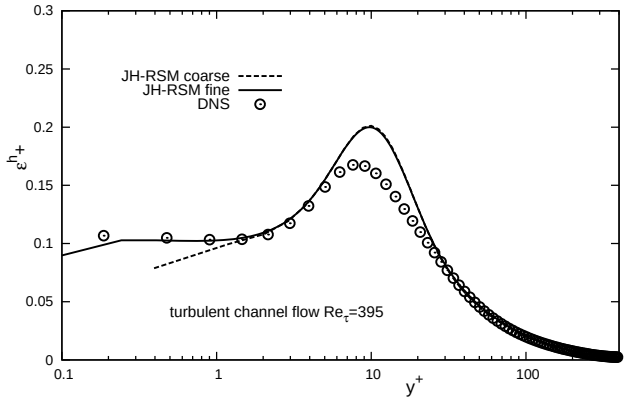

Figure 3.7: ϵ^{h+} for turbulent channel flow with $Re_\tau = 395$ - fine and coarse grid

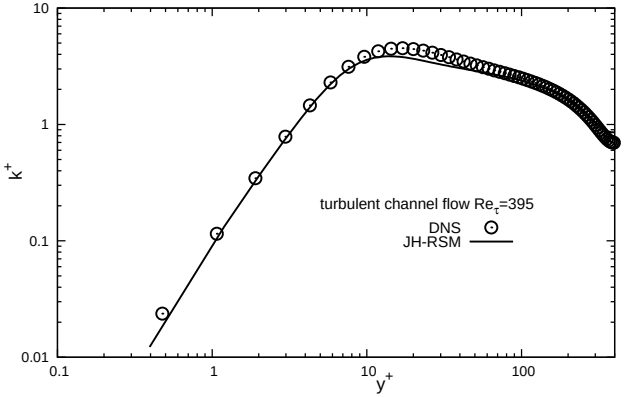

Figure 3.8: k^+ for turbulent channel flow with $Re_\tau = 395$

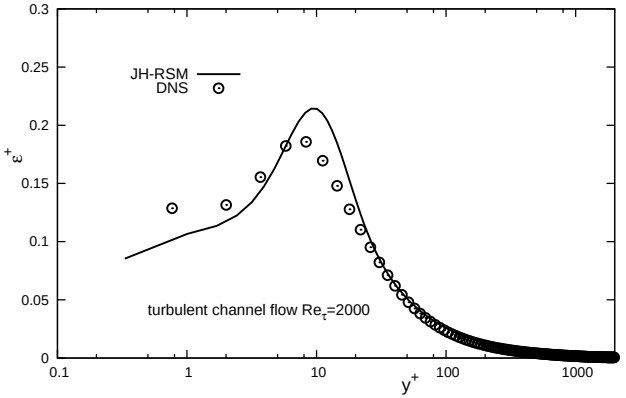

Figure 3.9: ϵ^{h+} for turbulent channel flow with $Re_\tau = 2000$

3.3 From Rotta's kL equation to the instability sensitive model

Since the results using the ω^h based JH-RSM have shown to be very promising, one can go a step further and introduce the instability sensitive term into the ω^h-equation of the JH-RSM. Before doing so, some explanations and clarifications have to be made. First of all Menter and Egorov [35] directly transformed their $\sqrt{k}L$-SAS model ($\sqrt{k}L = \Phi$) to ω-equation. Then they made it fit into the SST concept. A direct transformation of the $\sqrt{k}L$-equation to an ω-equation (which in fact means to properly transform the constants in front of the SAS part) is not preferable in the case of the JH-RSM ω^h based model for the following reasons:

- The JH-RSM uses the Reynolds stresses directly as input for the averaged momentum equation, while all eddy viscosity models use an artificial viscosity and velocity gradients to build up the Reynolds stresses entering the momentum equation as derivatives. For that reason there is no direct general relation between the Reynolds stress modeling concept and the eddy viscosity concept.

- Normally in one and two equation models the length scale supplying equation is set up completely empirical as a transport equation with similar structure like for example the equation for the turbulent kinetic energy. This probably is based on the very popular and early standard $k\epsilon$-model [31] in which the quantity epsilon was not seen as the quantity it really is, namely the dissipation at the smallest scales, but more as a quantity representing the energy transfer from the largest to the smallest scales. One reason for that treatment, since there exists an exact equation for the dissipation rate, is the fact that this equation has a lot of lets say unsafe to model terms and no reference data for comparison was available at the very beginning of modeling. So turbulence researchers that time took the way to use an empirical equation which was well calibrated on different testcases. In fact the ϵ equation in the JH-RSM is modeled out of the exact ϵ equation in a term-by-term manner. The dissipation taking place at the smallest scales can be connected to the practice of modeling the whole energy transfer from the largest to the smallest scales by the fact that there can be only that amount of energy dissipated at the smallest scales like transferred over the whole energy cascade with bearing in mind that the energy transfer from one eddy

to another happens only in case of eddies with similar size [19]. This means that exactly the energy dissipated at the smallest scales must have gone through the whole transfer process. As an outcome this equation is not completely comparable quantitatively in each term to other ϵ equations but physically as described before. Therefore a direct transformation of the Φ-equation is not straightforward.

A more convenient approach is to insert the SAS term directly from the $k\omega$-SST-SAS model into the ω^h-eq. of the JH-RSM and to calibrate it properly, not only in terms of quantity distribution and peak values but also by mimicking the flow behavior obtained with $k\omega$-SST-SAS. Nevertheless, before presenting the calibration procedure the full derivation from Rotta's $k\Psi$ model to the ω^h equation will be presented here just for the sake of completeness. Starting with Rotta's k and Ψ equation in boundary layer form to estimate the constants needed for the transformation:

$$\frac{\mathrm{D}k}{\mathrm{D}t} = P_k - C_\mu^{3/4}\frac{k^{3/2}}{L} + \frac{\partial}{\partial y}\left(\frac{\nu_t}{\sigma_k}\frac{\partial k}{\partial y}\right) \tag{3.14}$$

$$\frac{\mathrm{D}\Psi}{\mathrm{D}t} = \frac{\Psi}{k}P_k\left(\zeta_1 - \zeta_2\left(\frac{L}{L_{vk}}\right)^{1/2}\right) - \zeta_3 k^{3/2} + \frac{\partial}{\partial y}\left[\frac{\nu_t}{\sigma_\Psi}\frac{\partial \Psi}{\partial y}\right]. \tag{3.15}$$

Instead of the proposed model for the term containing the second velocity derivative [34]:

$$-\frac{3}{16}\frac{\partial^2 U(\vec{x})}{\partial y^2}\int_{-\infty}^{\infty} R_{12} r_y dr_y = -const \cdot P_k \cdot \frac{\Psi}{k}\left(\frac{L}{L_{vk}}\right), \tag{3.16}$$

or the newer version [35]

$$-\frac{3}{16}\frac{\partial^2 U(\vec{x})}{\partial y^2}\int_{-\infty}^{\infty} R_{12} r_y dr_y = -const \cdot P_k \cdot \frac{\Psi}{k}\left(\frac{L}{L_{vk}}\right)^2, \tag{3.17}$$

the following expression has been used:

$$-\frac{3}{16}\frac{\partial^2 U(\vec{x})}{\partial y^2}\int_{-\infty}^{\infty} R_{12} r_y dr_y = -const \cdot P_k \cdot \frac{\Psi}{k}\left(\frac{L}{L_{vk}}\right)^{1/2}. \tag{3.18}$$

It will be explained later why exactly this way of modeling has been chosen. Rotta proposed for the constants in the Ψ equation $\zeta_1 \approx 1.2$, based on

measurements of Rose [48], $\zeta_3 \approx 0.11 - 0.13$ and $\sigma_\Psi = 1.0$. $\zeta_2 = const$ can now be estimated from the logarithmic layer requirements ($\partial U/\partial y = u_\tau/\kappa y; k = u_\tau^2/\sqrt{C_\mu}; L = \kappa y; \nu_t = u_\tau \kappa y; P_k = \epsilon$) [35], for example with $\zeta_3 = 0.13$:

$$\kappa y P_k \zeta_2 = \kappa y P_k \zeta_1 - \zeta_3 \left(\frac{u_\tau^2}{C_\mu^{1/2}} \right)^{3/2} + \frac{u_\tau^3 \kappa^2}{C_\mu^{1/2}} \tag{3.19}$$

and finally

$$\zeta_2 = \zeta_1 - \frac{\zeta_3}{C_\mu^{3/4}} + \frac{\kappa^2}{C_\mu^{1/2}} \approx 0.97 \tag{3.20}$$

with $\kappa = 0.41$ and $C_\mu = 0.09$. With the length scale L chosen to be equal to κy in the logarithmic layer the following expression for ν_τ can be obtained:

$$\nu_{\tau log} = u_\tau \kappa y = C_{\nu_\tau} \sqrt{k} L = C_{\nu_\tau} \frac{u_\tau}{C_\mu^{1/4}} \kappa y. \tag{3.21}$$

It follows that $C_{\nu_\tau} = C_\mu^{1/4}$. For the transformation from the $k\Psi$-model to an ω equation similar to that one from the JH-RSM model, not only the constant ζ_2 has to be calculated but also the proper definition of L has to be found. From the logarithmic layer requirement $L = \kappa y$ and from the model for the turbulent length scale

$$L = C_L \frac{k^{3/2}}{\epsilon} = C_L \frac{k^{1/2}}{\omega} (\text{JH} - \text{RSM}), \tag{3.22}$$

it follows that $C_L = C_\mu^{3/4}$, which is needed to be inserted in the transformation process

$$\Psi = kL = \frac{k^{3/2}}{\omega} C_\mu^{3/4} \tag{3.23}$$

and consequently:

$$\omega = \frac{k^{3/2}}{\Psi} C_\mu^{3/4}. \tag{3.24}$$

By applying derivation rules

$$\frac{\mathrm{D}\omega}{\mathrm{D}t} = C_\mu^{3/4} \frac{\mathrm{D}\left(\frac{k^{3/2}}{\Psi}\right)}{\mathrm{D}t} \tag{3.25}$$

the transformation reads [9]:

$$\begin{aligned}\frac{\mathrm{D}\omega}{\mathrm{D}t} &= C_\mu^{3/4}\left[\frac{3}{2}\frac{k^{1/2}}{\Psi}\frac{\mathrm{D}k}{\mathrm{D}t} - \frac{k^{3/2}}{\Psi^2}\frac{\mathrm{D}\Psi}{\mathrm{D}t}\right] \\ &= \frac{3}{2}\frac{\omega}{k}\frac{\mathrm{D}k}{\mathrm{D}t} - \frac{1}{C_\mu^{3/4}}\frac{\omega^2}{k^{3/2}}\frac{\mathrm{D}\Psi}{\mathrm{D}t}.\end{aligned} \tag{3.26}$$

The simplified boundary layer form reads:

$$\begin{aligned}\frac{\mathrm{D}\omega}{\mathrm{D}t} &= \frac{\omega}{k}P_k\left(\frac{3}{2}-\zeta_1\right) - \omega^2\left(\frac{3}{2}-\frac{\zeta_3}{C_\mu^{3/4}}\right) + \frac{\omega}{k}P_k\zeta_2\left(\frac{L}{L_{vk}}\right)^{1/2} \\ &\quad + 3.0\nu_t\frac{1}{k}\frac{\partial\omega}{\partial y}\frac{\partial k}{\partial y} - 2.0\nu_t\frac{1}{\omega}\frac{\partial\omega}{\partial y}\frac{\partial\omega}{\partial y} - \frac{3}{2}\nu_t\frac{\omega}{k^2}\frac{\partial k}{\partial y}\frac{\partial k}{\partial y}.\end{aligned} \tag{3.27}$$

Finally by applying a model for the production $P_k = \nu_t S^2$ ($S = \partial U/\partial y$ is the mean shear rate in boundary layer form), replacing $\nu_t = C_\mu^{1/4}\sqrt{k}L = C_\mu^{1/4}\frac{k^{3/2}}{\epsilon}C_\mu^{3/4}k^{1/2} = C_\mu\frac{k}{\omega}$ and skipping the cross-diffusion term, since it is anyway included in the transformation from ϵ^h to ω^h, the obtained ω-equation reads:

$$\begin{aligned}\frac{\mathrm{D}\omega}{\mathrm{D}t} &= \frac{\omega}{k}P_k\left(\frac{3}{2}-\zeta_1\right) - \omega^2\left(\frac{3}{2}-\frac{\zeta_3}{C_\mu^{3/4}}\right) + C_\mu S^2\zeta_2\left(\frac{L}{L_{vk}}\right)^{1/2} \\ &\quad - 2.0C_\mu\frac{k}{\omega^2}\frac{\partial\omega}{\partial y}\frac{\partial\omega}{\partial y} - \frac{3}{2}C_\mu\frac{1}{k}\frac{\partial k}{\partial y}\frac{\partial k}{\partial y}.\end{aligned} \tag{3.28}$$

This is basically the final expression for a transformed ω-equation from Rotta's model, with the term including the second velocity derivative modeled by Menter's proposal. The resulting equation can be directly compared to the transformed ω^h-eq. in its constants and terms. As already stated, the cross diffusion has been skipped in the upper ω-eq. since the ω^h-eq. has a similar term. In a further step L can be expressed in terms of the turbulent length scale definition of the $k\omega$-SST-SAS $L_{SST} = \frac{k^{1/2}}{C_\mu^{1/4}\omega}$. By simple multiplication the length scale used later can be obtained:

$$L = \frac{k^{1/2}}{C_\mu^{3/4}\omega} = C_\mu\frac{k^{1/2}}{C_\mu^{1/4}\omega}. \tag{3.29}$$

By inserting this in eq. 3.28

$$C_\mu S^2\zeta_2\left(\frac{L}{L_{vk}}\right)^{1/2} = C_\mu^{3/2}S^2\zeta_2\left(\frac{L_{SST}}{L_{vk}}\right)^{1/2} = \widetilde{\zeta}_2 S^2\left(\frac{L_{SST}}{L_{vk}}\right)^{1/2}, \tag{3.30}$$

it follows that $\widetilde{\zeta}_2 \approx 0.026$, which is the value of the constant that is going to be compared with the calibrated one, used in this work. Rewriting eq. 3.28 leads to

$$\frac{\mathrm{D}\omega}{\mathrm{D}t} = \frac{\omega}{k} P_k \left(\frac{3}{2} - \zeta_1\right) - \omega^2 \left(\frac{3}{2} - \frac{\zeta_3}{C_\mu^{3/4}}\right) + \widetilde{\zeta}_2 S^2 \left(\frac{L_{SST}}{L_{vk}}\right)^{1/2} - C_{SAS} \left(C_\mu \frac{k}{\omega^2} \frac{\partial \omega}{\partial y} \frac{\partial \omega}{\partial y} + \frac{3}{4} C_\mu \frac{1}{k} \frac{\partial k}{\partial y} \frac{\partial k}{\partial y}\right), \tag{3.31}$$

with $C_{SAS} = 2$. During early runs with the IS-RSM, the model has shown large numerical instabilities and needed a lot of computational effort. High order numerical schemes for the convective terms could simply not be used. With low order schemes the IS-RSM showed the same going back to RANS mode, under locally unstable flows, like the $k\omega$-SST-SAS. The numerical instability and the computational effort stems from the complicated modeled $P_{\epsilon,3}$. It consists of two terms which should mimic the near wall term from the exact ϵ^h-eq., with changing in sign close to walls. In RANS simulations of three-dimensional flows with no homogeneous direction in terms of mean velocity and Reynolds stresses, $P_{\epsilon,3}$ consists of 108 parts. In URANS simulations with structure resolving possibility all of the 108 terms have to be used always in each timestep. This term should be modeled in a simpler way, for stability reasons as much as cost reduction. Turbulent channel flow simulations reveal that $P_{\epsilon,3}$ at its peak is only 1/4 of the production of ϵ^h [19]. Nevertheless it cannot be skipped since it is important for the high value of ϵ^h close to the wall. An easier way to model $P_{\epsilon,3}$ is not to use eq. 3.6, but instead a kind of simple gradient approach. This has been done in the context of modeling the near wall term E, which is important mainly in the buffer layer [3], in the Launder-Sharma $k\epsilon$ model. There it reads:

$$E = 2.0 \nu \nu_t \left(\frac{\partial^2 U_i}{\partial x_j^2}\right)^2. \tag{3.32}$$

This approach will also be used from now on together with modeling $P_{\epsilon,3}$ in the JH-RSM. The turbulent viscosity has been modeled in terms of Reynolds stress anisotropy (see eq. 3.4). One big advantage, beyond the much more stable behavior, is that it can be expressed with the OpenFOAM *GradGrad* operator, which accelerates its computation a lot. If this term is retransformed to its counterpart inside the ϵ^h equation, normalized and plotted over y^+ for the turbulent channel flow with $Re_\tau = 395$, the second peak close to the wall is captured nicely as can be seen in Fig. 3.10,

where it is compared to the complicated form of the $P_{\epsilon,3}$ term. The first negative peak cannot be captured, since the *GradGrad* operator always gives positive values, which is actually not so important, since very close to the wall the viscous diffusion and destruction terms make up the main parts. The value of ϵ^h is captured correctly, as can be seen in Fig. 3.11, where this quantity is plotted in its normalized form over y^+ (first calculated point is skipped). Also included in Fig. 3.11 is the ϵ^h distribution with the skipped $P_{\epsilon,3}$ term, which consequently leads to an overprediction close to the wall.

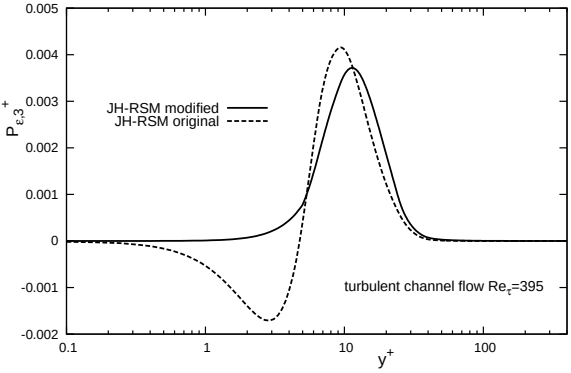

Figure 3.10: Different $P_{\epsilon,3}$ formulations - turbulent channel flow with $Re_\tau = 395$

A simple, robust and still, in some points away from the wall accurate enough formulation for $P_{\epsilon,3}$ has been found, implemented and tested for the turbulent channel in the context of Reynolds stress modeling (see Appendix A for the full model description). As a next step this is introduced into the IS-RSM. Accompanied by that, the numerical schemes for the convective schemes are going to be increased. The final ω^h-eq. of the IS-RSM has the following form:

$$\frac{\mathrm{D}\omega^h}{\mathrm{D}t} = \frac{\partial}{\partial x_k}\left[\left(\frac{1}{2}\nu + \frac{\nu_t}{\sigma}\right)\frac{\partial \omega^h}{\partial x_k}\right] + (C_{\epsilon 1} - 1)\,\frac{\omega^h}{k}P_k \\ - (C_{\epsilon 2} - 1)\,\omega^h\omega^h + \frac{2}{k}\left(0.55\frac{1}{2}\nu + \frac{\nu_t}{4}\right)\frac{\partial \omega}{\partial x_k}\frac{\partial k}{\partial x_k} + \frac{1}{k}P_{\epsilon,3} + P_{SAS} \tag{3.33}$$

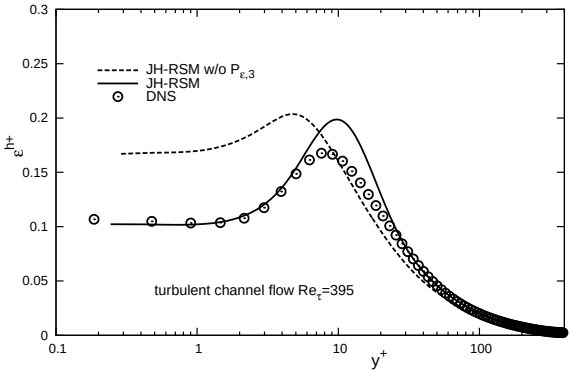

Figure 3.11: ϵ^h w/o $P_{\epsilon,3}$ for turbulent channel flow with $Re_\tau = 395$

with

$$P_{SAS} = 0.004\text{max}\left(1.755\kappa S^2\left(\frac{L_{SST}}{L_{vk}}\right)^{1/2} - 8T_2, 0\right),$$
$$T_2 = \frac{k}{1/3} max\left(\frac{1}{k^2}\frac{\partial k}{\partial x_j}\frac{\partial k}{\partial x_j}, \frac{1}{\omega^h\omega^h}\frac{\partial \omega^h}{\partial x_j}\frac{\partial \omega^h}{\partial x_j}\right). \tag{3.34}$$

The constants belonging to the instability sensitive term have been calibrated by means of testcase computations presented in the next chapter. $\widetilde{\zeta_2} \approx 0.026$ can be compared to $0.004 \cdot 1.755 \cdot \kappa \approx 0.00288$ which displays a reduction of the extra production of ω^h. This is actually in line with the expected behavior, that the Reynolds stress model can be triggered more quickly to its structure resolving mode. The original power of two at $(L_{SST}/L_{vk})^2$ caused a high overshoot of the fluctuations with complete destruction of the modeled quantities. At this point it must be recalled, that the power of two was originally introduced to detect directions of homogeneous turbulence and therefore deactivate the SAS term. In a structure resolving mode homogeneous turbulence cannot occur and so the power of two is in fact a triggering value for the SAS term, in areas where the length scale ratio is higher than one. In areas with lower length scale ratio it has a damping function. The power of 1/2 introduced in the IS-RSM is a mechanism which flattens the forcing, with increasing it in areas with length scale ratios smaller then one and reducing it in areas with length scale ratios larger then one. This leads to an even distribution and retained proper

modeled parts in eddy-resolving simulations, for the computed testcases (see Appendix B for the full IS-RSM description).

4 Testcase results

This chapter presents results for different flow configurations. The majority of them include large separations and are globally unstable. It is known that these flow configurations, namely the 2D Hill with different Reynolds numbers, the flow over a backward-facing step, the 3D Diffuser with two expanding walls and the tandem cylinder configuration with two distances in-between, representing two characteristic effects, are beyond most RANS models (the backstep can be quite accurately simulated with the use of Reynolds stress models). The IS-RSM could be a cost saving alternative for those simulations compared to DNS or even LES, still giving reasonable results compared to conventional RANS. Nevertheless, some of the testcases do not exhibit separation, however are locally unstable. These flow configurations in turn are beyond the SAS-concept as introduced by Menter and Egorov [35]. It will be shown that the IS-RSM can be triggered to an eddy-resolving model even for those testcases.

4.1 Decay of homogeneous isotropic turbulence

The decay of isotropic turbulence is presented here to guarantee the correct behavior of the structure resolving capability at high wave number range in spectral space and to ensure that the model is not accumulating energy at high wave numbers. In the $k\omega$-SST-SAS this is done by a grid dependent limiter [33], the IS-RSM will be limited just by the numerical scheme. This testcase describes basically a cube with the normalized dimensions of 2π in each direction and periodic boundary conditions everywhere, in which fluctuations decay from a starting field, since no outer forcing exists. From an existing DNS [51] of an isotropic turbulence case, with $Re_\lambda = 104.5$ based on the Taylor microscale, data was taken out of the DNS grid with 512 cells in each direction and then by spectral filtering made it suitable for much coarser grids containing 64 cells and 128 cells in each direction as can be seen in Fig. 4.1 showing the interpolated field on both grids in terms of velocity magnitude.

Fig. 4.2 shows the results of the IS-RSM for the decay testcase with 64^3 cells. The energy cascade is plotted over wavenumbers in spectral

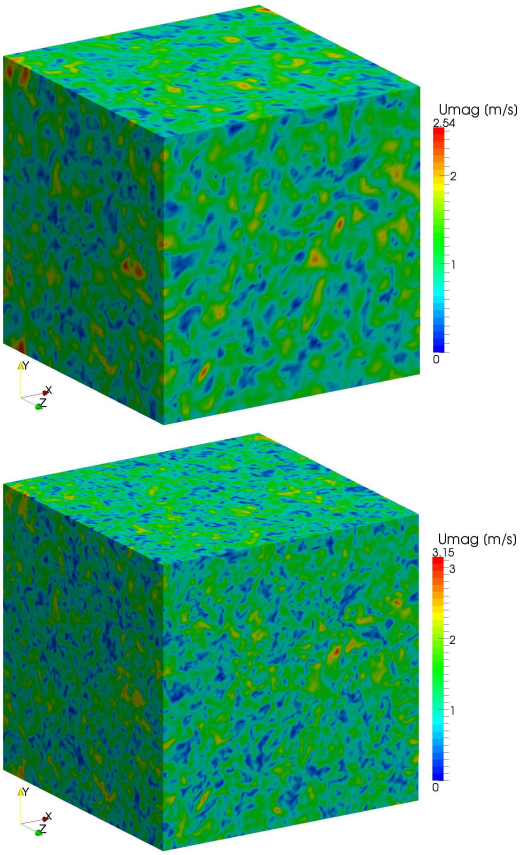

Figure 4.1: Interpolated velocity field from the well resolved DNS for decay of isotropic, homogeneous turbulence - coarse (64^3 cells) and fine grid (128^3 cells)

space after 0.45, 1.01 and 1.45 seconds of decay. As numerical scheme for discretization of the convective terms a blending between 95 per cent CDS and 5 per cent UDS has been chosen. The results of the model are in good agreement to the DNS for all three time spans with slight energy accumulation after a longer time span at high wavenumbers.

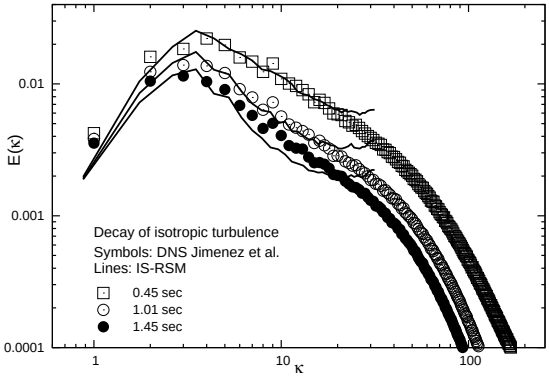

Figure 4.2: Decay of isotropic, homogeneous turbulence (64^3 cells) - IS-RSM computation with 95 per cent CDS

The same decaying of homogeneous isotropic turbulence has also been studied on a 128^3 cells containing grid with 95 per cent CDS. Fig. 4.3 shows the results of the IS-RSM compared to the DNS. Again the energy cascade is plotted for three different times of the decaying process. The decay process is captured quite convincingly. This is a nice feature, since it proves the ability to react on refined meshes correctly with resolving more structures, while grid dependency is not needed. Concerning the decay testcase the new model behaves as wanted. It captures the decay process very stable, due to the remodeled $P_{\epsilon,3}$ term and shows no energy loss at high wavenumbers, due to high order numerical scheme.

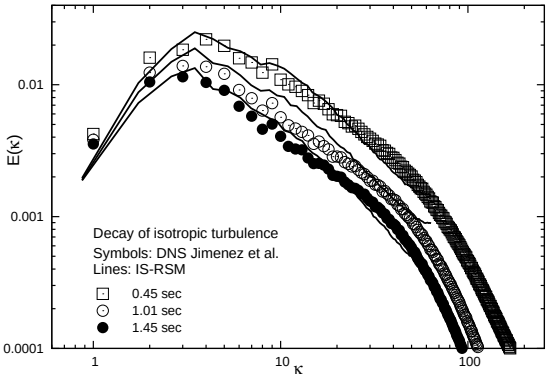

Figure 4.3: Decay of isotropic, homogeneous turbulence (128^3 cells) - IS-RSM computation with 95 per cent CDS

4.2 Turbulent channel flow at $Re_\tau = 395$

The turbulent channel testcase, as already mentioned, describes a turbulent plane channel flow, which is periodic in the streamwise direction and homogeneous in its averaged flow quantities in the spanwise direction. The simulation together with the SAS related term have been performed on three grids containing 360000, 460000 and 560000 cells (60 cells in the streamwise direction, 100 cells in height direction and 60 cells in width direction for the 360000 cells grid) with the width being the same as the height and the length two times the height as explained in [52]. Different grids have been chosen to prove the capability of the model to adjust itself to different grids and react with more resolved turbulent structures, without explicit grid dependency. Fig. 4.4 shows the instantaneous streamwise velocity field after a certain development time on the different grids. Obviously it is a real instantaneous field which means that the model is able to resolve structures even for quasi stable flows in terms of SAS structure resolving possibilities. What directly appears is, that the finer the grid the more resolved structures occur in the flow field. It should be mentioned that the simulation has been started on a steady field without even reducing the starting values for the modeled Reynolds stresses, which could help as a trigger. As numerical scheme a blending between 95 per cent of CDS and 5 per cent of UDS has been used. It is one thing to trigger a model to resolve structures by systematically reducing its modeled val-

ues, but a completely different one to match the statistics correctly after enough time averaging. To validate the statistics the averaged quantities have to be analyzed, which are the time and space averaged profiles of the streamwise velocity and the Reynolds stresses. Furthermore the modeled portion of the stresses to the resolved one is going to be checked to make sure that the model is not completely destroyed and the simulation gets the character of an under-resolved DNS. For the statistics the flow has been averaged in time over 1000 flow-through times. Since the spanwise and the streamwise direction are homogeneous in terms of averaged quantities, the time averaged fields can also be averaged over those two space directions. As a comparison to the results obtained by the instability sensitive model, the DNS of Iwamoto et al. [18] is plotted as reference. Fig. 4.5 shows the normalized mean velocity U^+ over the normalized wall distance y^+ in logarithmic scale on the 460000 cells grid. As can be seen the velocity profile obtained by the turbulence model is in very good agreement with the DNS. It is also in very good agreement with the linear law in the viscous sublayer for $y^+ < 5$ and with the logarithmic law for $y^+ > 30$, which are also plotted in Fig. 4.5. The normalized Reynolds normal stresses are shown in Fig. 4.6 for the medium grid (460000 cells). The IS-RSM gives qualitatively and quantitatively good results of the Reynolds stresses with some overshoot of the normalized streamwise stress component $u^+ = \sqrt{\overline{uu}}/u_\tau$ and underestimation in the peaks of the other two normal components. Fig. 4.7 shows the resolved u^+ and the modeled part on two different grids (460000 and 560000 cells). The modeled part is by far smaller than the resolved one on both grids but definitely cannot be neglected. This means, that the simulation character does not change to an under-resolved DNS like behavior with completely vanished modeled part. It is important to mention the reduced modeled part on the finer grid, which underlines the adapting character of the instability sensitive model. Fig. 4.8 shows the normalized turbulent shear stress $\overline{uv}^+$ over y^+ on the medium grid. It is illustrated here to complete the plots of the Reynolds stresses. The simulation with the IS-RSM captures sufficiently accurate the shear stress profile obtained by the DNS. Just as an reminder, a LES giving similar results in terms of predicted velocity profiles needs at least 1.2 million cells, while wall models have been used. The Reynolds stresses with that grid have been essentially worse predicted [15].

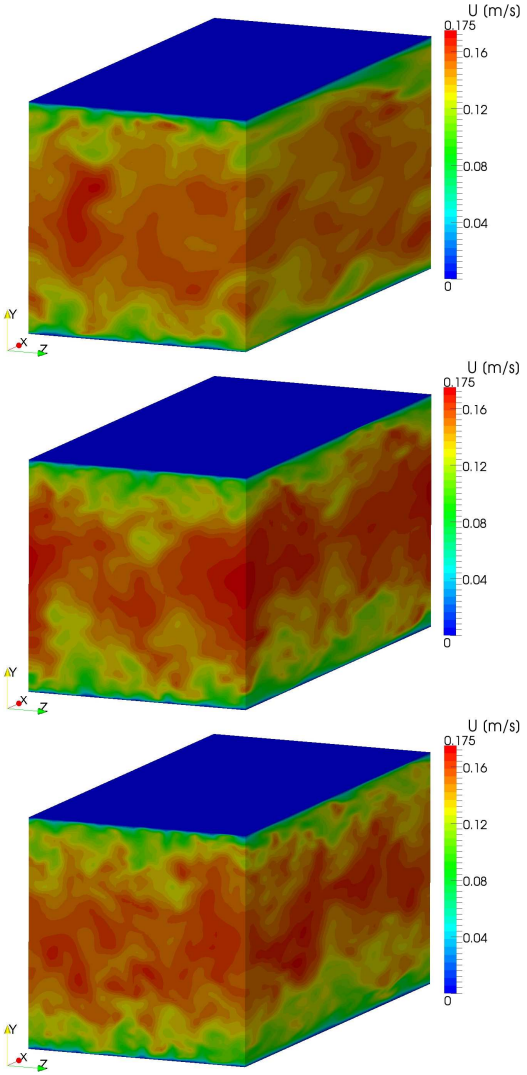

Figure 4.4: Instantaneous streamwise velocity for turbulent channel flow with $Re_\tau = 395$ - coarse, medium and fine grid

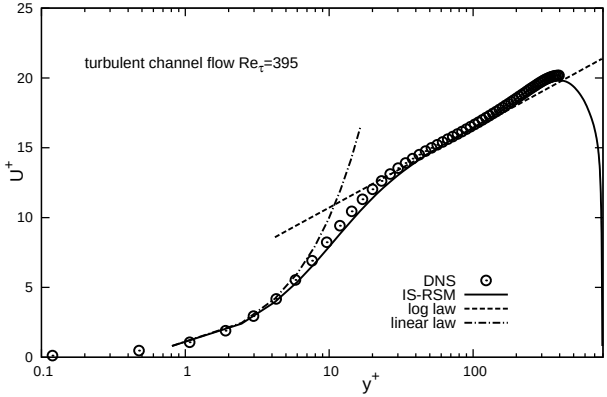

Figure 4.5: Streamwise mean velocity for turbulent channel flow with $Re_\tau = 395$ - IS-RSM computation

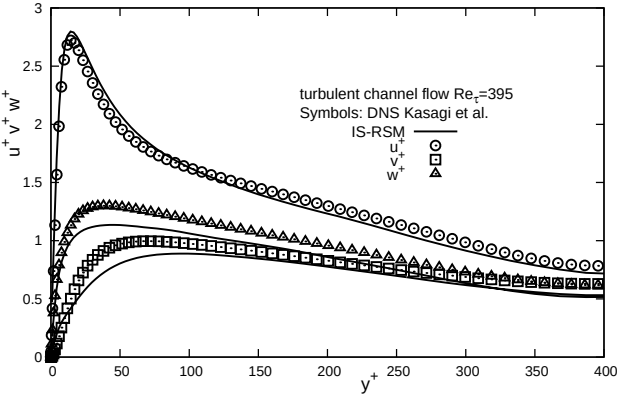

Figure 4.6: Normal stress components for turbulent channel flow with $Re_\tau = 395$ - IS-RSM computation

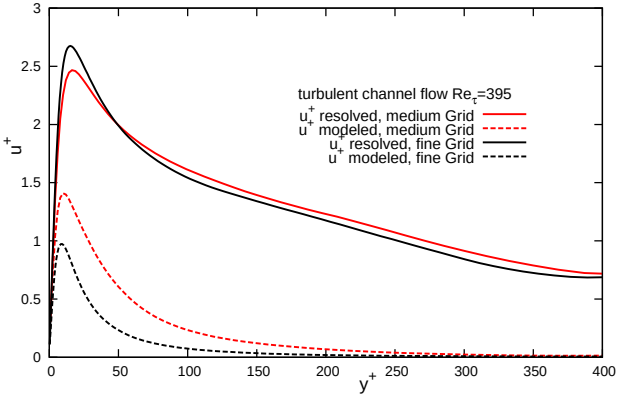

Figure 4.7: Normalized $\overline{uu}$ stress component for turbulent channel flow with $Re_\tau = 395$ - grid adaptivity

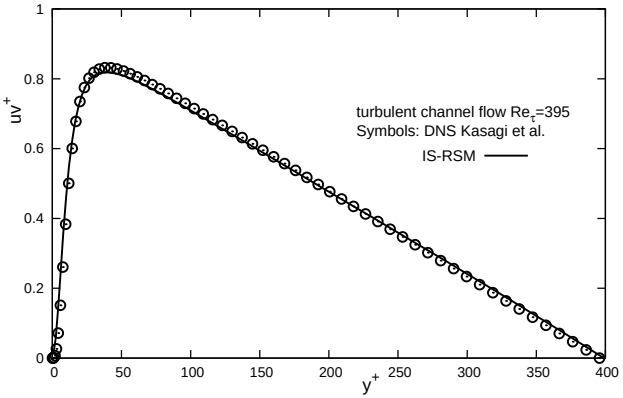

Figure 4.8: Normalized shear stress component $\overline{uv}$ for turbulent channel flow with $Re_\tau = 395$ - IS-RSM computation

4.3 Turbulent Flow over a 2D Hill with different Reynolds numbers

The 2D Hill testcase features two hills, of which only half of each is included in the geometrical setup. The geometry starts on top of the first hill and ends on top of the second one. It should mimic an infinite number of hills, one by one, a part of which is cut out and represented by those two half hills. The geometry is bordered by two walls, the lower one following the contour of the hills and the upper one forming a straight wall. The dimensions are 9 H in length with H being the hill height, and 3.14 H in total height. The flow separates from the first hill, due to the adverse pressure gradient, reattaches somewhere in-between the hills and then accelerates till it reaches the top of the second hill. The described flow topology can be seen in Fig. 4.9, where streamlines are shown on top of the normalized pressure field for the lower Reynolds number case. Periodic boundary conditions were applied on inlet and outlet for all quantities, with an imposed mass flow representing a given Reynolds number. The grid for the 2D Hill contains approximately 25500 cells in the xy-plane and 60 cells in the spanwise direction for the computation in conjunction with the IS-RSM. Two Reynolds numbers are going to be examined, $Re_H = \frac{U_b H}{\nu} = 10600$ and 37000, with U_b being the bulk velocity. The reference data for the lower Reynolds number consists of experimental data by Rapp [45] and a well resolved LES on a 13.1 million cells grid by Breuer [6]. For the higher Reynolds number only experimental data by Rapp is going to be compared to the results obtained by using the turbulence models. The computational grid has been refined appropriately close to the walls, giving maximum $y+$ values of somewhat higher then 1 for $Re_H = 10600$ and peak values of 3 for $Re_H = 37000$ in the accelerating part of the second hill. The y^+ distribution on the lower wall can be seen in Fig. 4.10 for both Reynolds numbers.

Starting with the lower Reynolds number 10600 the RANS simulations have been done exclusively on the 2D grid in the xy-plane with 25500 cells. Opposite to the turbulent channel flow the quality of the results obtained with the JH-RSM is known to be very inaccurate, with an overprediction of the recirculation zone after the first hill and a large underprediction of the turbulence quantities in the separating shear layer. This is not only the case for that particular RANS model but for a broad range of models, at least concerning the low values of the turbulent kinetic energy and the Reynolds stresses [54]. So the performance of the IS-RSM is of special interest. Fig.

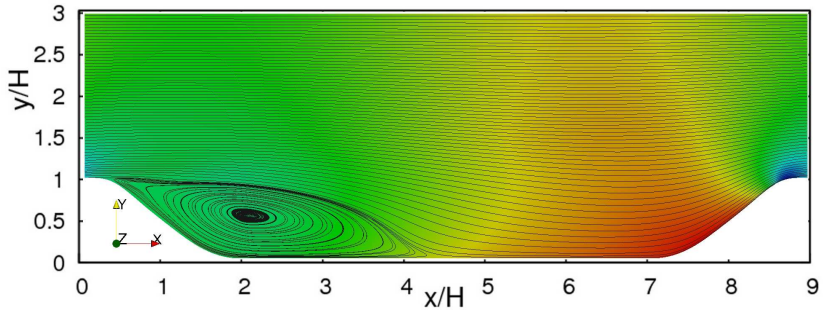

Figure 4.9: Normalized dimensions and typical streamlines for the 2D Hill

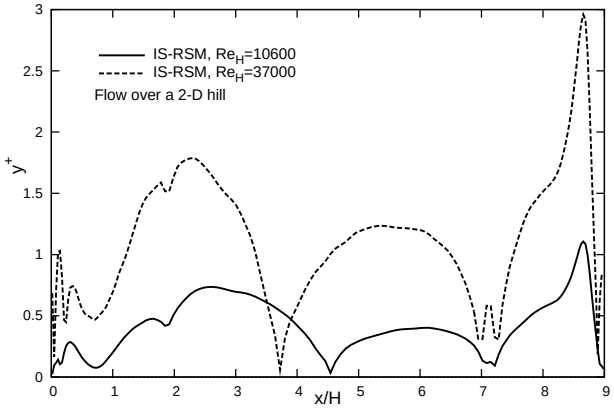

Figure 4.10: y^+ for both Reynolds numbers on the lower wall

4.11, 4.12, 4.13 and 4.14 show crossplots of the normalized mean streamwise velocity U/U_b, the normalized stress in the streamwise direction $\overline{uu}/U_b^2$, the normalized turbulent kinetic energy k/U_b^2 and the normalized Reynolds shear stress $\overline{uv}/U_b^2$ at ten discrete positions $x/H = 0.05$ (on top of the first hill), 0.5 (close to the separation point), 1.0 (at the beginning of the recirculation zone), 2.0 directly inside the recirculation zone), 4.0 (at the the end of the recirculation zone), 6.0 (outside the separation), 7.0 (at the bottom of the second hill) and 8.0 in the accelerating part of the second hill. As already mentioned, the JH-RSM overestimates the length of the recirculation zone with reattachment at around 6.3 x/H. As can be seen in Fig. 4.11, the peak in the velocity profile close to the lower wall on top of the first hill at position 0.05 x/H is highly underestimated leading to a deficit in the following points of interest along the hill. The overprediction of the recirculation zone a direct result of the high underestimation of the turbulent quantities in the separating shear layer starting close to the separation point, as can be seen in Fig. 4.12, 4.13 and 4.14. The oscillation of the separation point, caused by the curved surface and the backsplashing into the freestream under a sharp angle, dramatically increases the normal stress in the streamwise direction right before the separation point inside the boundary layer. This can be seen clearly in Fig. 4.12 in the first crossplotted line.

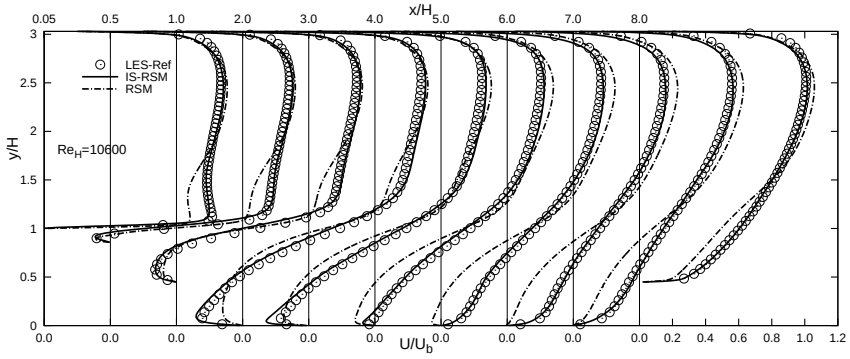

Figure 4.11: Streamwise mean velocity at characteristic points - IS-RSM and RSM for $Re_H = 10600$

Fig. 4.15 gives an impression of the oscillating separation point by means of pressure fluctuations calculated with the IS-RSM, on top of the first hill

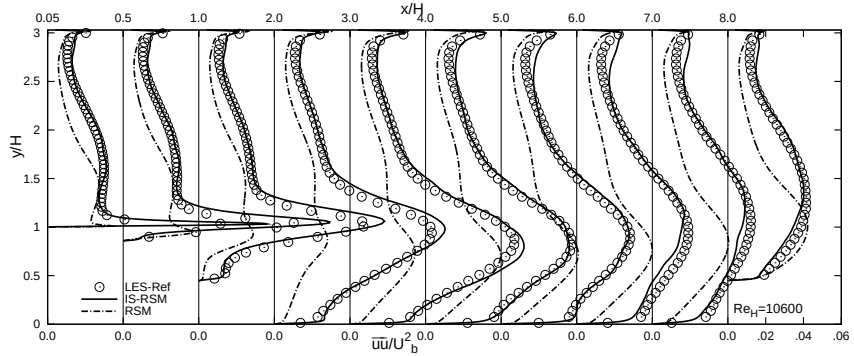

Figure 4.12: Normalized $\overline{uu}$ stress component at characteristic points - IS-RSM and RSM for $Re_H = 10600$

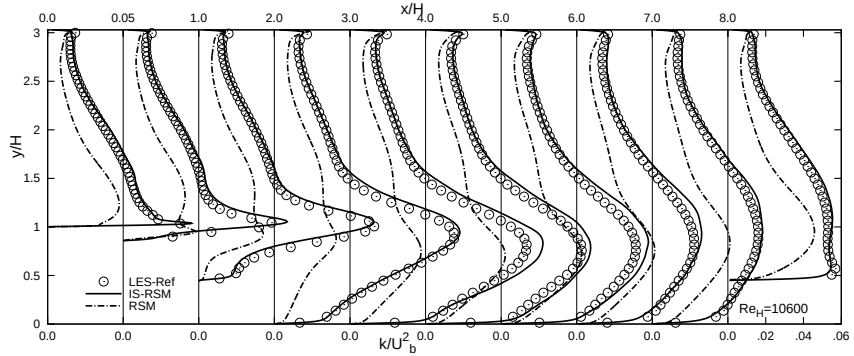

Figure 4.13: Turbulent kinetic energy at characteristic points - IS-RSM and RSM for $Re_H = 10600$

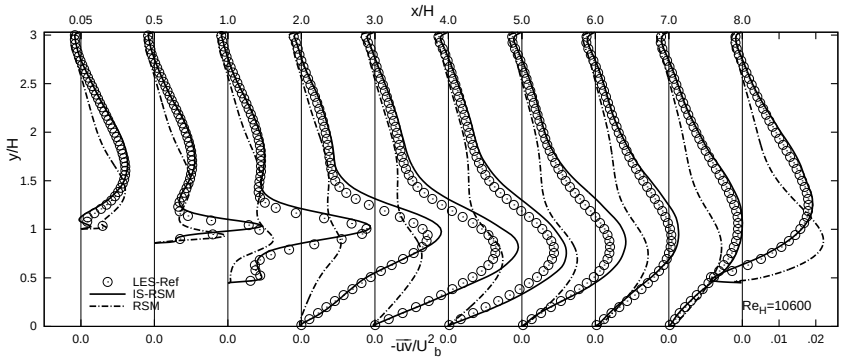

Figure 4.14: Normalized shear stress component $\overline{uv}$ at characteristic points - IS-RSM and RSM for $Re_H = 10600$

coloured by instantaneous streamwise velocity, with the intention to show the highly unstable separation line changing in time and space.

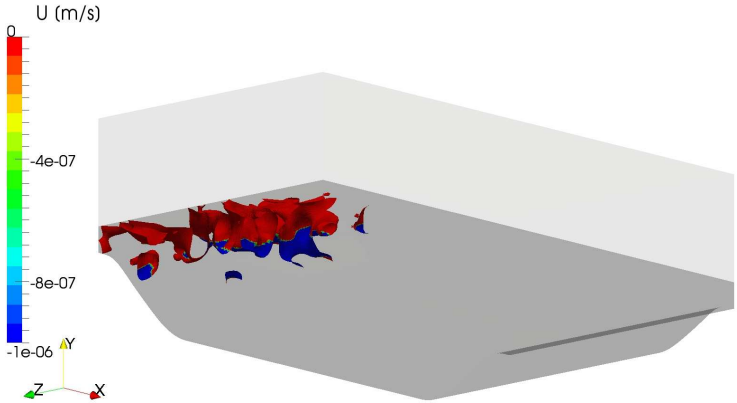

Figure 4.15: Pressure fluctuations close to separation point - $Re_H = 10600$

The very high value of $\overline{uu}/U_b^2$ affects the turbulence in the separating shear layer in the sense that it leads to a faster mixing of the recirculation zone with the freestream [14]. That phenomenon with highly unstable large scale motions near the crest of the first hill is beyond a statistical approach. Thanks to its eddy-resolving features, the IS-RSM can capture exactly this

unstableness. Consequently, the results have to improve. Qualitatively the flow pattern obtained with the RANS is close to reality, but quantitatively wrong. The results of the IS-RSM nicely follow the reference date in terms of velocity profile distribution along the hill as can be seen in Fig. 4.11. Also the results of the turbulence quantities shown in Fig. 4.12 to 4.14 are very close to the reference data. The simulation with the instability model have also been done on a coarse grid containing 240000 cells. The results in terms of normalized mean streamwise velocity and normalized turbulent shear stress can be seen in Fig. 4.16 and 4.17. The coarse grid shows the main features of the turbulence quantities with the peaks being in the correct range and proper behavior of the flow with respect to velocity distribution.

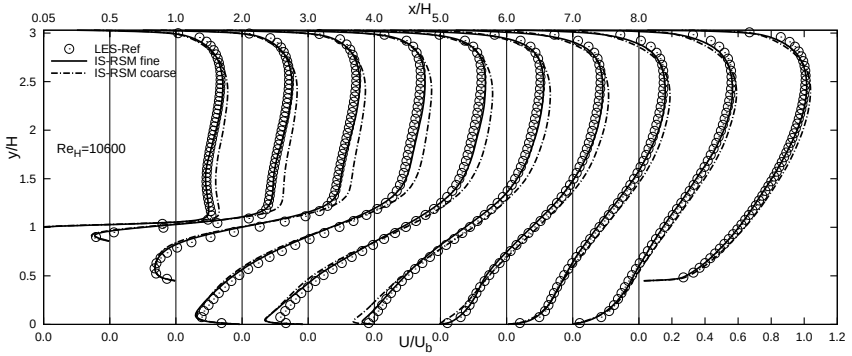

Figure 4.16: Streamwise mean velocity at characteristic points - IS-RSM for $Re_H = 10600$, coarse and fine grid

Coming to the higher Reynolds number case $Re_H = 37000$, Fig. 4.18 shows the normalized mean velocity U/U_b plotted over the hill height, along the hill in the streamwise direction at the presented 10 discrete points. Fig. 4.19 shows the turbulent shear stress. The main features are pretty much the same as in the lower Reynolds number case. The flow separates close to the top of the first hill, reattaches in-between the hills and accelerates at the beginning of the second hill. The reattachment point, which can be extracted from the experiments made for that specific Reynolds number, moves somewhat closer to the first hill ($x/H \approx 3.7$ compared to $x/H \approx 4.7$ for $Re_H = 10600$). The normalized turbulent shear stress $\overline{uv}/U_b^2$ is slightly lower in its peaks in the separating shear layer compared to the lower

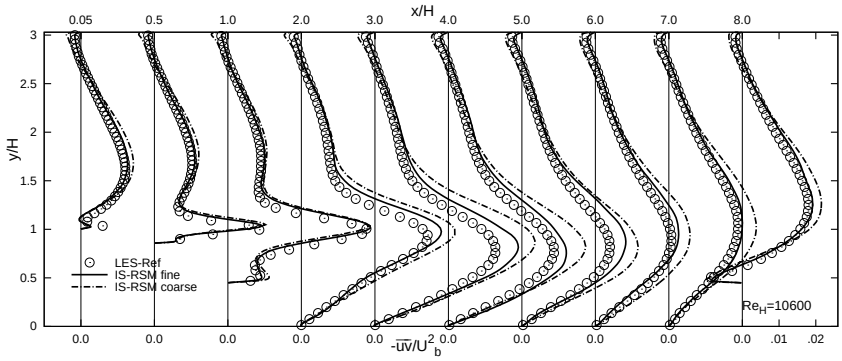

Figure 4.17: Normalized shear stress component $\overline{uv}$ at characteristic points - IS-RSM for $Re_H = 10600$, coarse and fine grid

Reynolds number case, with the absolute values naturally being higher. The basic information which can be taken out of Fig. 4.18 is that for this higher Reynolds number the JH-RSM is even less adequate for reproducing the flow features, respectively the reattachment point and the shape of the velocity profile, correctly. The recirculation zone is highly overpredicted. The instability sensitive approach shows a very good velocity distribution with proper reattachment point. Also the velocity peak on top of the first hill is quantitatively captured. The simulations with the IS-RSM have been done exclusively on the fine grid. Since the Reynolds number increased nearly by four times the coarse grid wouldn't have been suitable.

Finally the friction coefficient, plotted in Fig. 4.20 gives an impression of how the two Reynolds numbers 10600 and 37000 differ from each other. The case with the higher Reynolds number shows earlier reattachment and a lower velocity gradient inside the recirculation zone. Unfortunately there is no experimental data available containing C_f for the higher Reynolds number, but at least the reattachment point is known which coincides with the results from the IS-RSM. The RSM gives a totally different friction coefficient for two reasons. Firstly the very low turbulence intensity in the separating shear layer causes a long recirculation zone and consequently a delayed transit through the zero friction line. Secondly the velocity gradient close to the lower wall is too low in the beginning of the recirculation zone, leading to a totally different shape in C_f distribution compared to the IS-RSM and the reference LES, as can exemplarily be seen in Fig. 4.21 for

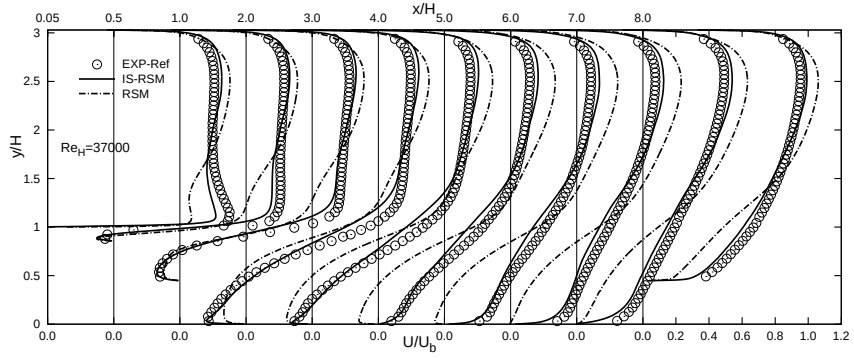

Figure 4.18: Streamwise mean velocity at characteristic points - IS-RSM and RSM for $Re_H = 37000$

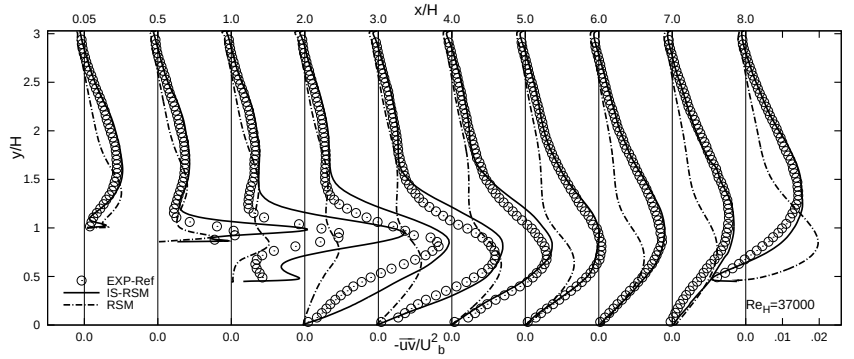

Figure 4.19: Normalized shear stress component $\overline{uv}$ at characteristic points - IS-RSM and RSM for $Re_H = 37000$

the lower Reynolds number case.

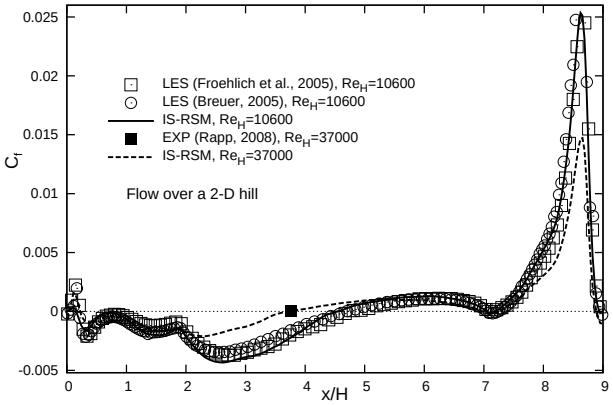

Figure 4.20: Friction coefficient on the lower hill wall - IS-RSM, different Reynolds numbers

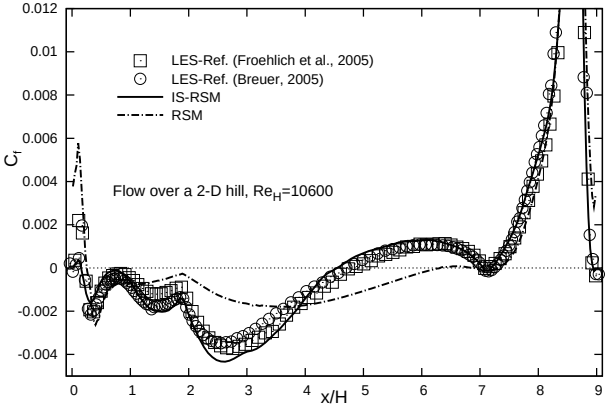

Figure 4.21: Firction coefficient on the lower hill wall - IS-RSM and RSM for $Re_H = 10600$

4.4 Turbulent flow in a 3D Diffuser

The three-dimensional diffuser with a Reynolds number of 10000, based on duct height and bulk velocity, is a very special testcase. In contrast to asymmetric diffuser geometries, like that one of Obi et al. [39], which has one homogeneous direction, namely the spanwise one, one plane and one expanding wall, the 3D Diffuser of Cherry et al. [7] has two expanding walls, the upper and the right wall. Those two walls expand in a different ratio, the upper wall expanding faster. The geometry and its dimensions can be seen in Fig. 4.22. The inlet of the diffuser consists of a duct with the width being more than three times the height. This testcase is somewhat different to the ones already presented in this work, since it is not only a matter of separation from curved surfaces, actually not as curved as the 2D Hill, but also a problem of properly catching the flow anisotropy due to corner vortices in the inlet duct. Slight variation in them can lead to totally different separation behavior even on the wrong wall. Fig. 4.23 gives an impression of the high flow unsteadiness due to turbulent separation inside the diffuser by means of the instantaneous streamwise velocity shown on different planes (IS-RSM simulation).

Since the IS-RSM is able to switch into structure resolving mode for locally unstable flows, as shown for the case of the turbulent channel, this should also be possible for the inlet duct of the diffuser. In Fig. 4.24 the

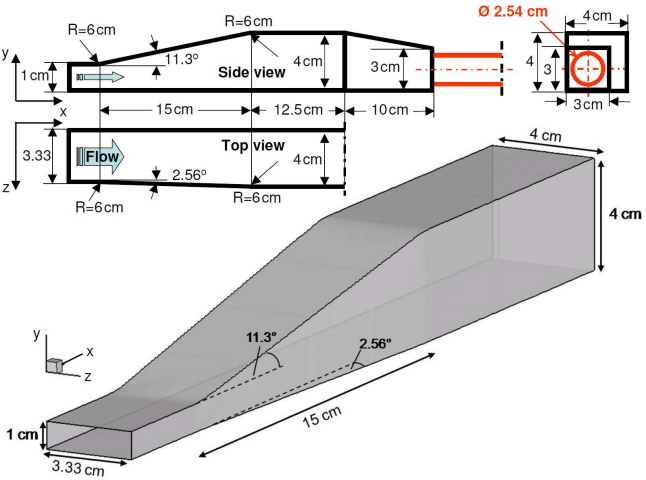

Figure 4.22: Sketch with dimensions of the 3D Diffuser

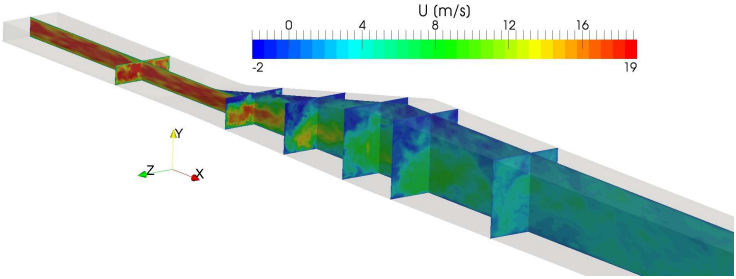

Figure 4.23: Fluctuating streamwise velocity through the diffuser at $Re_H = 10000$ - IS-RSM computation

instantaneous streamwise velocity is shown in the duct geometry. This simulation has been done as a precursor step to prove the structure resolving capability.

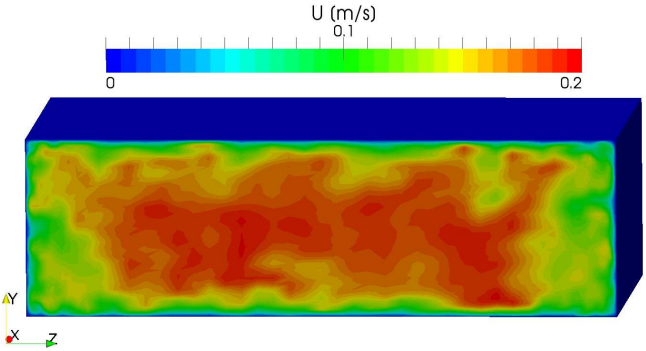

Figure 4.24: Fluctuating streamwise velocity through the inlet duct at $Re_H = 10000$ - IS-RSM computation

To mimic the periodic 3D duct out of the precursor computation, the geometry of the 3D Diffuser has been expanded in its inlet region nearly by the same amount in the negative streamwise direction as the dimensions of the precursor 3D duct simulation, with an inlet section of $15H$ and H being the inlet duct height.
The 3D Diffuser was presented as testcase in the 13th ERCOFTAC SIG 15 workshop in Graz [5] with focus on turbulence modeling. The results of that workshop showed that eddy viscosity RANS approaches, no matter if two equation models or the more sophisticated four equation $k\epsilon - \zeta f$, all separate at the right expanding wall in contrast to the experiments of Cherry et al. [7] and highly resolved DNS of Ohlsson et al. [40] (220 million cells), which showed the separation to occur on the complete upper wall.
Reynolds stress models, either as explicit algebraic Reynolds stress models or as differential ones in general performed better with the separation being at least in the upper corners. The difference in the results obtained with RANS models can be explained with the inability of the eddy viscosity models to reproduce corner vortices in the inlet duct.
Regarding the results of the models used in this work, all simulations have been performed on the same grid obtained from one partner of the European project for "Advanced Turbulence Simulation for Aerodynamic Application Challenges" (ATAAC). It was originally designed for RANS simulations and

therefore had to be refined for the computations with the IS-RSM. Results obtained with the JH-RSM have been calculated on two versions of the grid containing 750000 and 1.5 million cells leading to the same results and thus to grid convergence. The finer grid with 1.5 million cells has been refined in the streamwise direction by doubling the points. Furthermore, the inlet section has been elongated to allow for the use of the recycling method, which forces a properly designed turbulence model to resolve turbulent structures, due to an imposed mass flow on a certain cyclic area. The final grid used for runs with the IS-RSM contained approximately 3.75 million cells, while $y^+ < 1.5$ has been ensured in the first gridpoints close to the walls in the whole domain. The boundary conditions were set to atmosphere pressure at the outlet and zero gradient for all the other quantities. Vice versa, fixed values were chosen for all quantities at the inlet with zero gradient for pressure for the simulations with the RANS model and the recycling method as inlet boundary condition for the IS-RSM.
Fig. 4.25 compares contours of the time averaged streamwise velocity on five planes in the streamwise direction at the positions $x/H = 2, 5, 8, 12$ and 15. The results of the IS-RSM are shown together with experimental data, DNS data and results from the JH-RSM. As can be seen, the instability sensitive RSM separates on the upper wall like the experiments and the DNS, with somewhat too early separation at the first position and a reduced recirculation area at the last position. The RANS version of the same model separates properly at the beginning of the expansion, as can be seen in the first plane, but then the recirculation zone moves somewhat to the right wall, occupying in the latter part of the expansion the upper and lower right corner, which simply leads to a different flow than in the reference data.

The pressure recovery obtained with the instability sensitive model is mostly consistent with Cherry's data, while the RANS results are closer to the DNS. This can be seen in Fig. 4.26 where the pressure coefficient distribution $C_p = (p - p_{ref})/(\frac{1}{2}\rho U_{bulk}^2)$ is shown along the lower wall, with p_{ref} being the reference pressure on the lower wall very close to the expansion. JH-RSM underestimates the pressure coefficient starting from half the expansion length, while the IS-RSM starts with the correct gradient in the C_p and later slightly overestimates the pressure recovery, which is in line with the underestimated size of the recirculation zone at $x/H = 12$ and 15. The results of the RANS model concerning the good prediction of the pressure coefficient is pure coincidence, since the overall flow pattern is different.

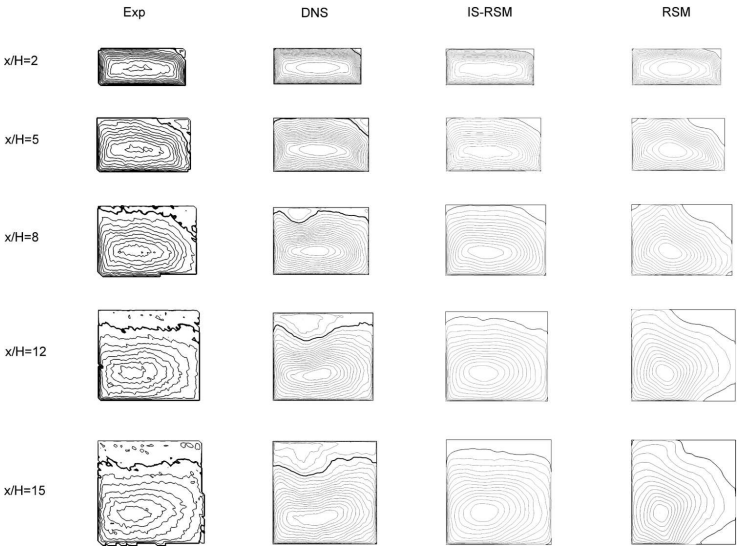

Figure 4.25: Velocity contour plots at five characteristic streamwise positions - Performance of different models

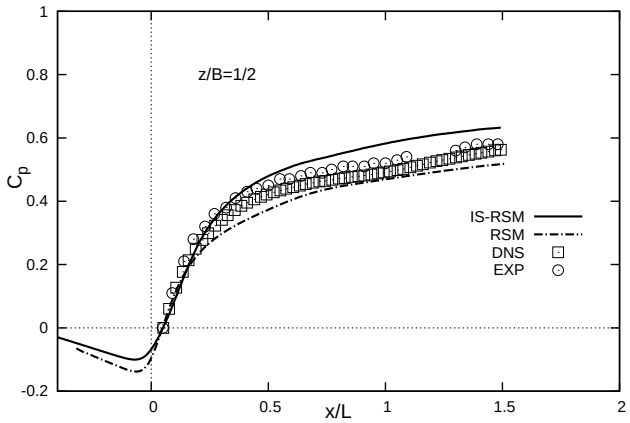

Figure 4.26: Pressure coefficient on the lower diffuser wall - performance of different models

The comparison, as obtained from the velocity contour plots, is important for checking the global flow behavior. But nevertheless, crossplots of different quantities in the streamwise direction over the height of the diffuser cannot be neglected for final conclusions about the model performance. The reference datasets offer three points in the spanwise direction, namely $z/B = 0.25$ (close to the left wall), $z/B = 0.5$ (in the middle of the inlet duct) and $z/B = 0.875$ (close to the right expanding wall) where B is the total width of the inlet duct. From these points crossplots can be made in the streamwise direction starting from the expansion point $x/H = 0$. Fig. 4.27 to 4.29 show graphs of the normalized mean streamwise velocity profile starting in the three different spanwise positions and plotted in the streamwise direction. Concerning the results of the JH-RSM, its inability to display the separation correctly on the whole upper wall, is evident in the crossplotted velocity profiles. At the positions $z/B = 0.25$ and $z/B = 0.5$ the velocity is highly overestimated in nearly every point in the streamwise direction in the upper half of the diffuser. This is in line with the contour plots, which reveal no separation on the upper wall but more in the upper right corner. Therefore the velocity crossplots at $z/B = 0.875$ show a high underestimation of the velocity in the upper half of the diffuser in most of the reference points in the streamwise direction. As can be seen in Fig. 4.27 to 4.29 the IS-RSM performs essentially better in these crossplots, with the discrepancies compared to the reference data being small compared to its underlying RANS model. Especially close to the upper wall, where the RANS model has a great velocity deficiency, the instability sensitive model shows significantly better results due to the well reproduced global flow features with separation over the entire upper wall, starting approximately at $x/H = 8$.

To close the 3D Diffuser testcase in Fig. 4.30 to 4.32 crossplots of the normalized mean Reynolds stress component in the streamwise direction $\frac{\sqrt{\overline{uu}}}{U_{bulk}}$ are shown. The IS-RSM overpredicts the Reynolds stresses close to the upper wall right from the beginning at the positions $x/H = 2$ and 5. In latter reference points the agreement is quite good, especially concerning the shape of the stress profiles. The RSM in general exhibits good agreement in term maximum values of the normal Reynolds stresses with some deficiencies in the shape close to the lower wall.
As a final statement on the diffuser case, the instability sensitive model is able to reproduce the recirculation zone in its correct position and length and also nearly quantitatively in its exact dimensions in each streamwise position, while the RSM model is not able to simulate the separation zone

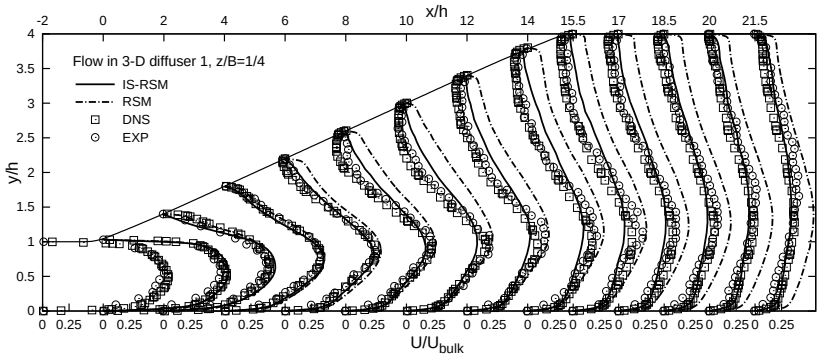

Figure 4.27: Streamwise mean velocity at $z/b = 1/4$

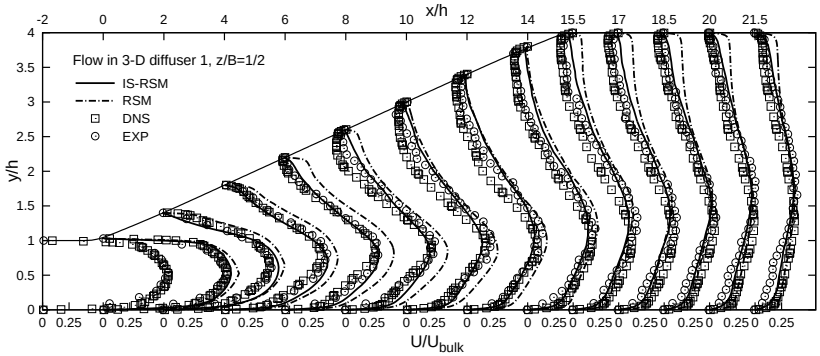

Figure 4.28: Streamwise mean velocity at $z/b = 1/2$

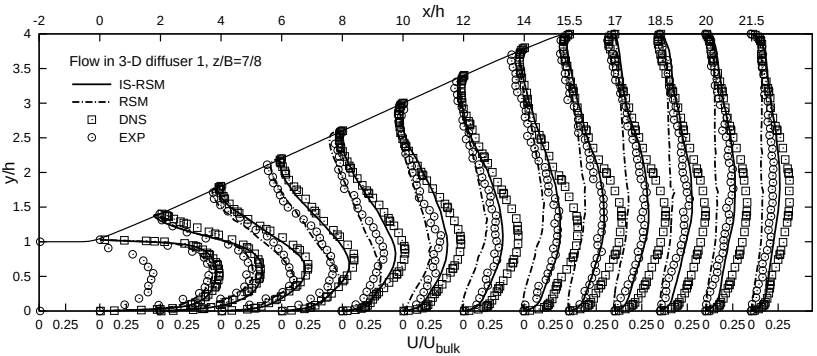

Figure 4.29: Streamwise mean velocity at $z/b = 7/8$

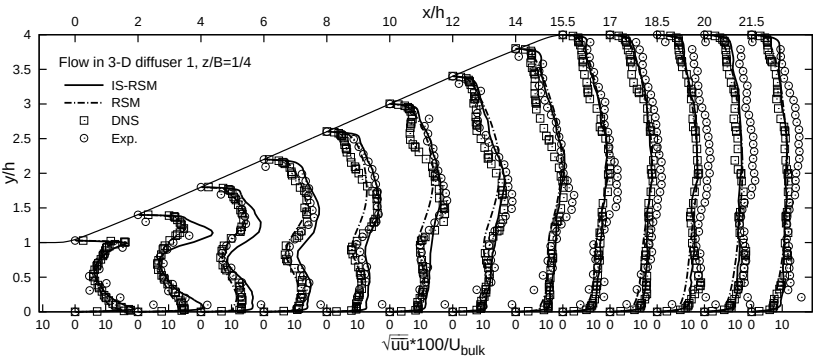

Figure 4.30: Normalized $\overline{uu}$ stress component at $z/b = 1/4$

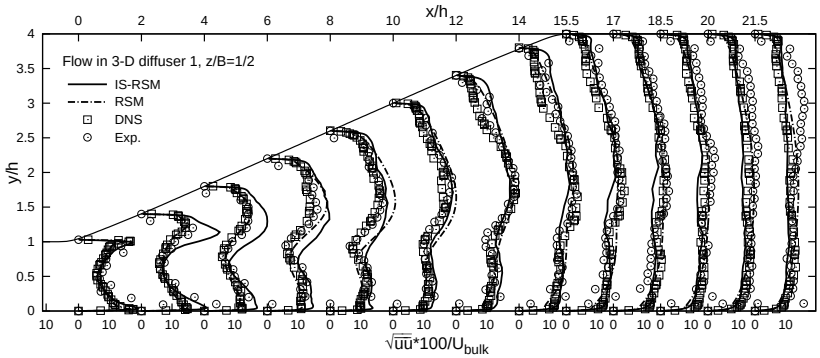

Figure 4.31: Normalized $\overline{uu}$ stress component at $z/b = 1/2$

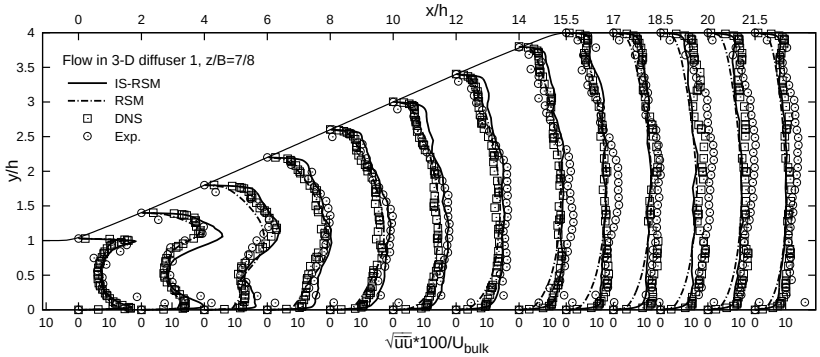

Figure 4.32: Normalized $\overline{uu}$ stress component at $z/b = 7/8$

which occupies the entire upper wall.

4.5 Flow over a backward-facing step

The flow over a backward-facing step has been investigated for long time [25] [32] [10] with different Reynolds numbers and expansion ratios $Er = D/d$. D is hereby the height of the outlet region and d the height of the inlet region. Here the focus lies on the one with $Re = \frac{U_0 H}{\nu} = 5100$, where H is the step height, U_0 the freestream velocity and $Er = 1.2$. The backstep describes a boundary layer flow on which a sudden expansion is imposed. This consequently leads to a flow separation. However, after a certain distance to the step the flow recovers. The flow topology can be seen in Fig. 4.33 by means of streamlines through the geometry along with the normalized dimensions of the domain. A lot of good data is available for comparison, even a DNS with data that can be used to calculate the budgets of the Reynolds stresses or the turbulent kinetic energy, as for example the dissipation rate. As the flow through the 3D Diffuser, the flow over the backstep is unstable due to separation at the expansion, but in the spanwise direction homogeneous in terms of averaged quantities. Its inlet lies quite close to the separation point, which - contrary to the diffuser - is fixed for geometrical reasons. The close inlet needs special treatment, since fixed inlet boundary conditions would dampen out the capability of the IS-RSM to switch into structure resolving mode. The recycling technique mentioned above is also unserviceable since the boundary layer is developing from its starting value. To overcome these problems an inflow generator [27] had to be used to ensure fluctuating velocity fields in each time step and artificially damped modeled Reynolds stresses. The grid for the IS-RSM computations contains 53000 cells in the xy-plane, properly refined close to the walls and in the separating shear layer, and 30 cells in the spanwise direction with a dimension of three step heights. Periodic boundary conditions were imposed on the spanwise boundaries, while zero gradient outlet boundary conditions with fixed outlet pressure (atmospheric pressure) and fixed inlet boundary conditions per time step for each quantity except the pressure, have been used. For the computations with the JH-RSM, which accompany the eddy-resolving ones, the two-dimensional grid has been in use, including fixed inlet boundary conditions not only per time step but through the whole computation. Fig. 4.34 shows the 3D calculation with the instantaneous streamwise velocity obtained from the IS-RSM simulation. The flow enters the domain on the left, separates at the step and

recovers after some distance to the expansion. Obviously the upper part of the domain with freestream character shows quasi steady behavior.

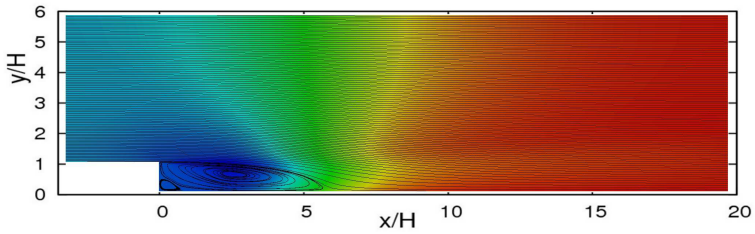

Figure 4.33: Normalized dimensions and characteristic streamlines for the flow over a backward-facing step at $Re_H = 5100$

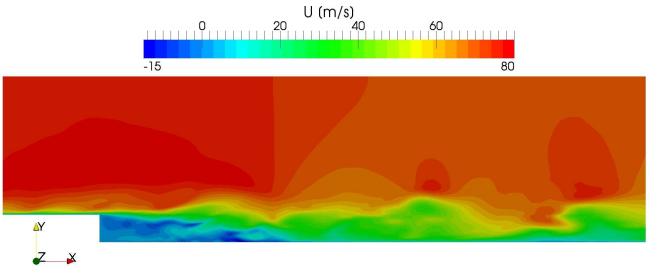

Figure 4.34: Instantaneous streamwise velocity through the backstep configuration - IS-RSM computation

It is known from literature [19] that Reynolds stress models, especially the JH-RSM, perform well for the backstep flow. The reattachment point is around x/$H = 6.1$. Fig. 4.35 shows normalized mean streamwise velocity profiles U/U_0 along the step at different streamwise positions $x/H = 0$, 2, 4, 6, 10, 15, 19. $x/H = 0$ is the separation point from the fixed step edge, 2 and 4 are points in the recirculation zone, 6 marks the end of the recirculation zone and 10, 15 and 19 are points in the recovering boundary layer. Results from a DNS [32] as well as experimental results [25] are compared to the ω^h based JH-RSM and to the IS-RSM. As can be seen both turbulence models perform quite well with no remarkable differences from the reference data.

Fig. 4.36 and Fig. 4.37 show profiles of the normalized Reynolds stress

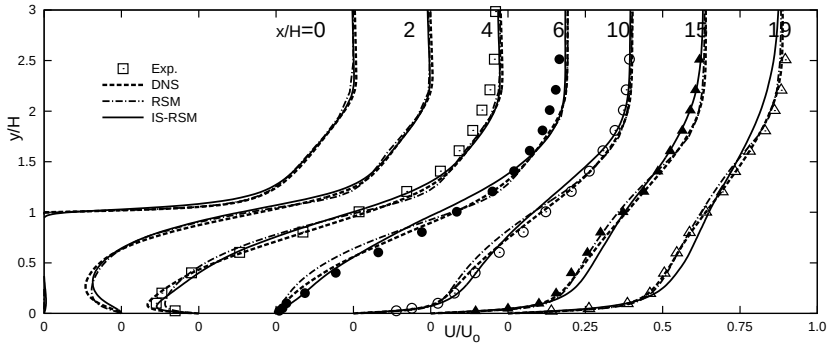

Figure 4.35: Streamwise mean velocity for the backstep flow with $Re_H = 5100$

components $u^{'}/U_0$, with $u^{'} = \sqrt{\overline{uu}}$ and $v^{'}/U_0$ ($v^{'} = \sqrt{\overline{vv}}$) as representatives of turbulent quantities. Again both turbulence models perform well, with some overshoot in the stress components far away from the bottom wall and close to the symmetry plane, calculated by the IS-RSM in the latest positions 15 and 19. This can be explained by the outlet being close to those very last positions. The outlet boundary condition with fixed pressure reflects back into the domain somewhat and thus has some impact in regions where actually nothing happens in terms of gradients of turbulence quantities.

The feature very hard to capture with conventional RANS models is the negative peak in the pressure coefficient C_p (shown in Fig. 4.38) and the friction coefficient C_f (shown in Fig. 4.39) inside the recirculation zone. Those are the consequence of the unsteadiness in the near wall region with different splashing regions. The IS-RSM captures the negative peaks as well as the distribution of C_P and C_f very accurately as can be seen in Fig. 4.38 and 4.39, while the RSM is not able to reproduce them.

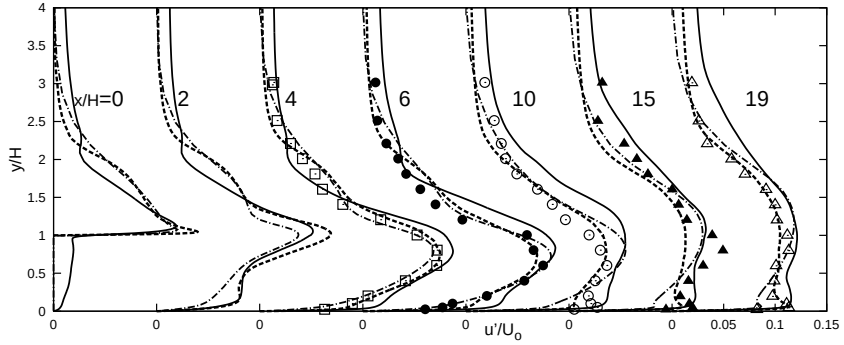

Figure 4.36: Normalized $\overline{uu}$ stress component for the backstep flow with $Re_H = 5100$

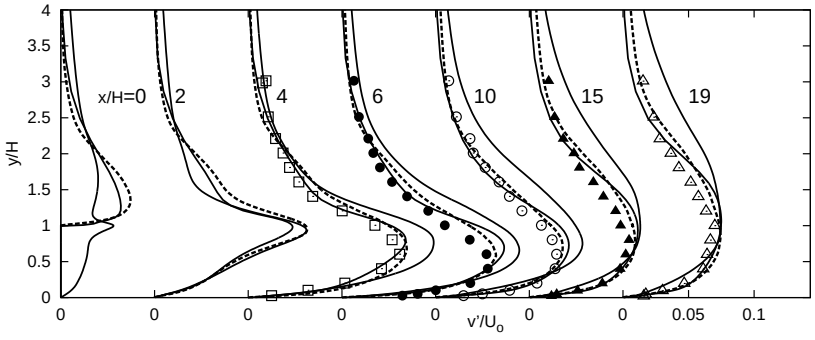

Figure 4.37: Normalized $\overline{vv}$ stress component for the backstep flow with $Re_H = 5100$

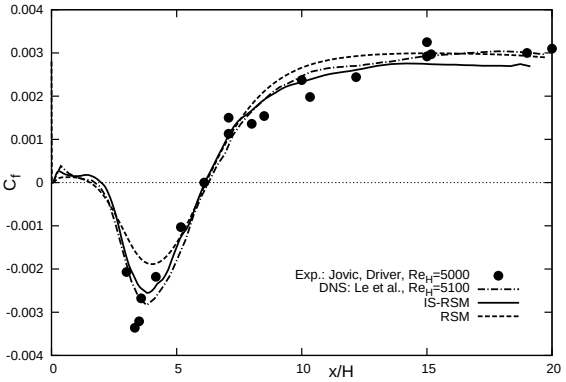

Figure 4.38: Friction coefficient on the lower wall - performance of different models

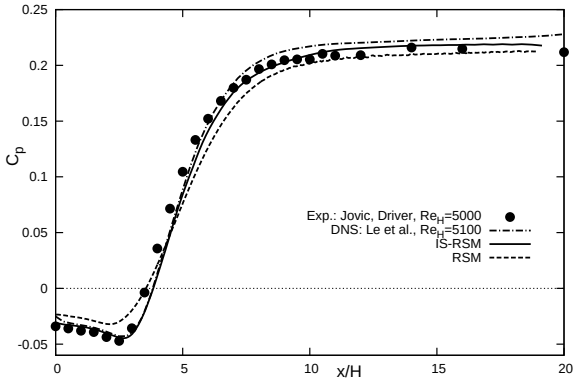

Figure 4.39: Pressure coefficient on the lower - performance of different models

4.6 Turbulent flow past a tandem cylinder configuration

The tandem cylinder testcase describes two cylinders in a row with a certain distance in-between. The oncoming flow has zero angle of attack, which means it is in terms of time averaged flow quantities a totally symmetrical geometrical setup. This testcase was also part of the ATAAC European project. Experiments have been carried out at the NASA BART facilities in Langley by Jenkins et al. [22] [23] and Neuhart et al. [37]. These experiments serve as reference data for the performed simulations. It should be mentioned that a lot of classical RANS calculations have been done [26]. These calculations have been undertaken by applying the URANS method, since the vortex street behind each cylinder is unsteady by nature. Steady simulations would get serious convergence problems or/and the results would be questionable. Basically it can be said, that no model performed satisfyingly in getting proper results for all the major flow quantities.
The experiments consist of two setups which differ in the spacing between the cylinders. This different spacing leads to a completely different flow topology, which will be discussed later. Fig. 4.40 and 4.41 show the different setup with isocontours of vorticity magnitude representing the highly unsteady flow behavior, where the spacings are $L/D = 1.435$ for the short distance and 3.7 for the large distance. D is hereby the cylinder diameter. The vorticity magnitude, coloured by the normalized streamwise velocity U/U_0, with U_0 being the freestream velocity has been computed with a IS-RSM simulation. This highly unsteady vorticity field proves its capability to switch into structure resolving mode for these testcases. Fig. 4.42, taken from [22], shows the experimental facility at NASA Langley, with the cylinders having the height of 16 D and being fixed on a disc, which can be rotated to change the angle of attack.

The testcase is especially interesting in terms of the acoustic field and the noise strength, since it should mimic the landing gear of a plane (namely the wheels in a row). The landing gear is one of the main noise sources during landing [4] [28]. For that reason the short distance is of particular interest, since it is close to the standardized distances of real landing gears. Nevertheless, the long distance bears a different flow topology and is therefore also taken into consideration. In the experiments the oncoming flow was slightly turbulent with a very low turbulence level of 0.09 per cent [22] and a Reynolds number of $Re = 166000$ based on inlet velocity and cylinder

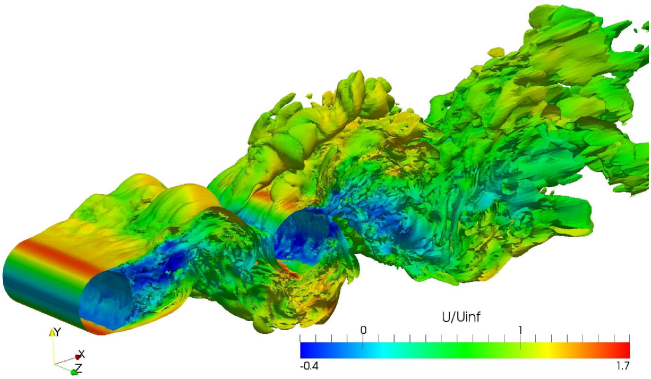

Figure 4.40: Vorticity magnitude coloured by normalized instantaneous streamwise velocity - $L/D = 3.7$ computed with the IS-RSM

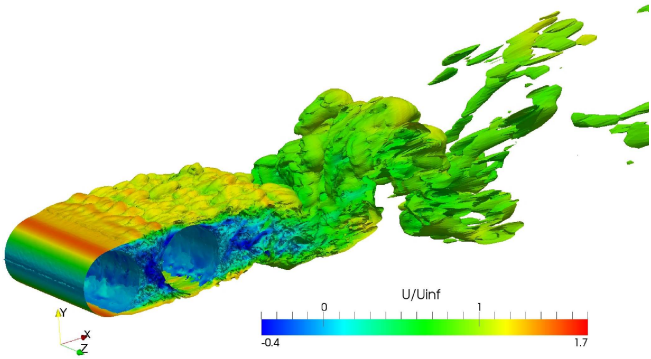

Figure 4.41: Vorticity magnitude coloured by normalized instantaneous streamwise velocity - $L/D = 1.435$ computed with the IS-RSM

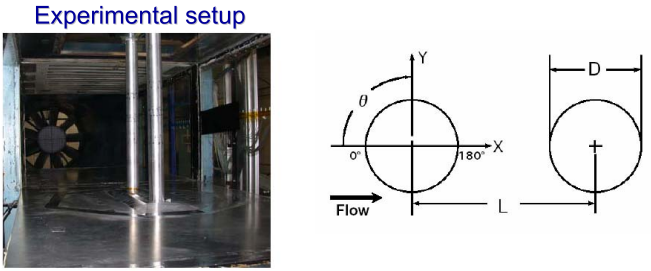

Figure 4.42: Experimental setup - BART facilities at NASA Langley

diameter. This in combination with a laminar flow regime starting from the stagnation points of the cylinder would have led to serious problems for turbulence models in predicting the flow field quantitatively correctly. In further examinations by Neuhart et al. [37] the experiments where slightly changed with triggering wires on the first half of both cylinders, to ensure quick transition from laminar flow to turbulent one. One may argue that the oncoming flow hitting the second cylinder is purely turbulent. But actually this is only partly true. The testcase with the long distance consists of alternating detachment from the first cylinder including laminar regions, which has a large effect on the flow field behind the second cylinder. In the following comparisons the tripped experiment will always be used as reference.

First of all the differences between the two distances are going to be explained. For the large distance case the flow detaches from the first cylinder, develops in a vortex stress and hits the second cylinder. Unfortunately this vortex street contains laminar regions, that are a consequence of the distance, which does not allow for the developing of a fully turbulent vortex street. Behind the second cylinder the flow detaches and develops into a fully turbulent vortex street. For the small distance case the cylinders are so close that no vortex street can develop behind the first cylinder. The flow detaches from the first cylinder and reattaches on the first half of the second cylinder. The distance is therefor not short enough, for the whole configuration to be seen as one large obstacle where the flow detaches from the first cylinder and builds up a complete detachment hull over the second cylinder.

4.6.1 Large distance case $L/D = 3.7$

As already mentioned conventional RANS models have major problems predicting the flow field, which is highly unsteady because of separations from moving points, reattachments and very unstable recirculation regions. Furthermore the effects add up behind the second cylinder. The mesh for this case using a 2D simulation with the JH-RSM contains around 60000 cells in the xy-plane with points clustered around the cylinders, in-between them and in the wake behind the second cylinder. The mesh can be seen in Fig. 4.43 which zooms in on the area near the cylinders.

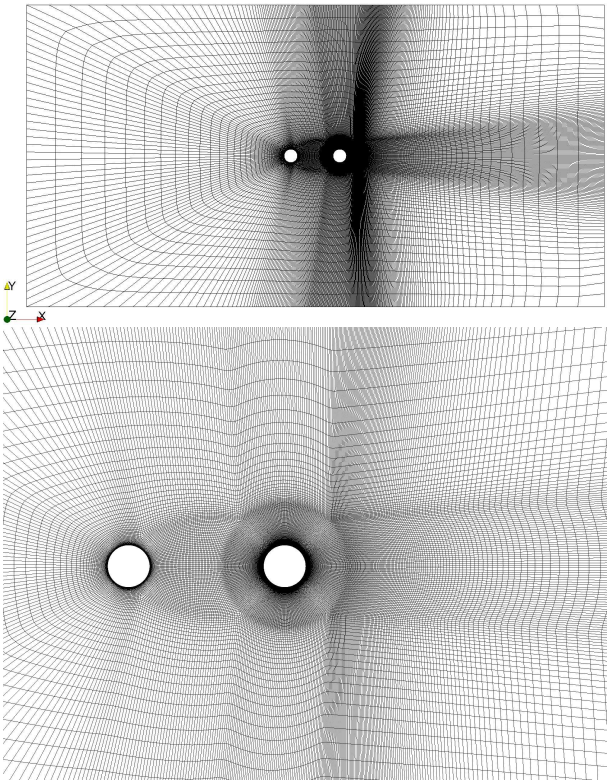

Figure 4.43: Computational grid for $L/D = 3.7$

The dimensions of the computational domain were set far enough from the area of interest using zero gradient outlet boundary conditions and

freestream boundary conditions for the rest. The inlet has fixed value boundary conditions. Coming to the eddy-resolving simulations of the tandem cylinder testcase, the grid was extruded in the spanwise direction by an amount of two cylinder diameters, while the grid itself remained the same in the xy-plane as for the JH-RSM calculations. 80 identically-sized cells were placed in the spanwise direction, resulting in 4.8 million cells in total. The time step was appropriately chosen to obtain peak CFL numbers below 0.7 for all simulations. The inlet values (since it is a fixed value inlet boundary condition) were not changed, so no artificial damping of the modeled turbulence values was done. This means that the whole field up to the second half of the first cylinder remains steady. The simulation with the IS-RSM was triggered to switch into structure resolving mode with the unsteady separation from the first cylinder and then remained in that mode for the space between the cylinders and behind the second cylinder. It stayed in a very steady mode around the cylinders, as it was expected, since no instability triggering obstacle or phenomena could be found in the rest of the domain. As numerical scheme a blending between upwind and CDS with 92 per cent CDS was chosen. Averaging has been applied over 80-100 convective time units and was found to be enough. Fig. 4.44 and 4.50 show the normalized mean streamwise velocity U/U_0 on the centreline between the cylinders and in the wake of the second cylinder. The JH-RSM (running in unsteady mode) underpredicts the recirculation zone length behind the first cylinder with a high overshoot in the peak value of the velocity. In contrast to that it overpredicts the length behind the second cylinder severely. The totally wrong behavior behind the second cylinder is partly due to the wrong prediction of the flow field in-between the cylinders, which has impact on the second cylinder. The IS-RSM matches the experimental results much better. The distribution and the peak values agree reasonably well with the reference. The end of the recirculation zone is very close to the experimental data, especially behind the second cylinder. The length of the recirculation zone in the gap region improves also notably compared to the JH-RSM.

The obtained velocity profiles are the direct consequence of the predicted turbulence quantities. The flow is highly unsteady and three-dimensional. These features cannot be captured sufficiently by the JH-RSM. Fig. 4.46 and Fig. 4.47 show the normalized two-dimensional turbulent kinetic energy $2DTKE = (\overline{uu}+\overline{vv})/2U_0^2$ in-between and behind the second cylinder. The high overprediction of $2D\ TKE$ behind the first cylinder compared to the experiments leads to the very small recirculation zone which was shown

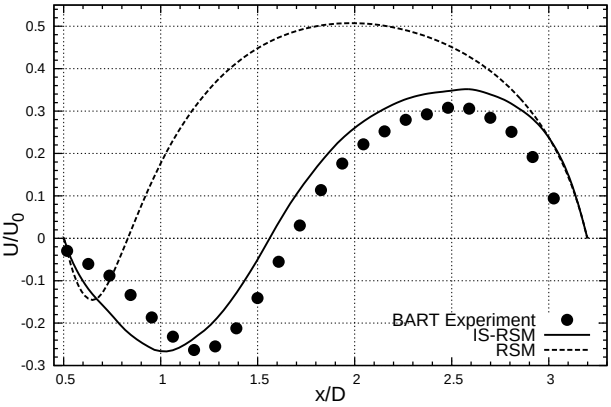

Figure 4.44: Mean normalized centreline velocity in the gap for $L/D = 3.7$

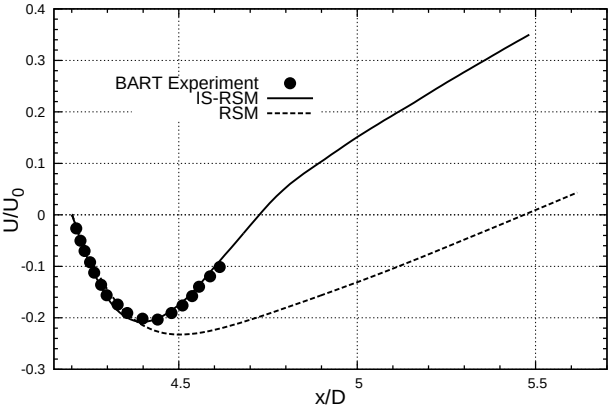

Figure 4.45: Mean normalized centreline velocity in the wake for $L/D = 3.7$

in the graph of the streamwise velocity profile. Behind the second cylinder the turbulence is underpredicted, which then leads to a very long recirculation zone. It should be mentioned that the turbulent kinetic energy consists mainly of resolved turbulent structures. This underlines the high unsteadiness since even conventional URANS without real structure resolving features obviously resolves a big part of them. By using the IS-RSM, which is capable of capturing the three-dimensional interactions of the large turbulent structures properly, the $2DTKE$ is well predicted in terms of distribution and peak values, while again the wake region behind the second cylinder shows slightly better results.

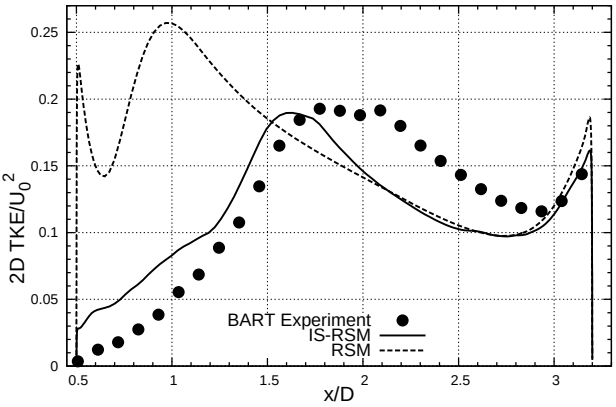

Figure 4.46: Centreline $2D$ turbulent kinetic energy in the gap for $L/D = 3.7$

To complete the part of the tandem cylinder simulations with the large distance Fig. 4.48 and 4.49 show the pressure coefficient $C_P = (p - p_0)/(\frac{1}{2}\rho U_0^2)$ on the surfaces of the first and second cylinder. Here p_0 is the pressure at the inlet of the domain. The profile obtained with JH-RSM on the second cylinder is quite close to the experiments, except for an overestimated pressure plateau behind the cylinder. The suction peaks on the first cylinder are overestimated by a remarkable amount as can be seen in Fig. 4.48. Nevertheless, the pressure coefficient is the only quantity computed with the RSM, which is not so far from the experimental reference data. The IS-RSM can do this job better for both cylinders, with improvement in terms of predicted suction peaks on the first cylinder and improved pressure plateau behind the second cylinder. A grid independence study

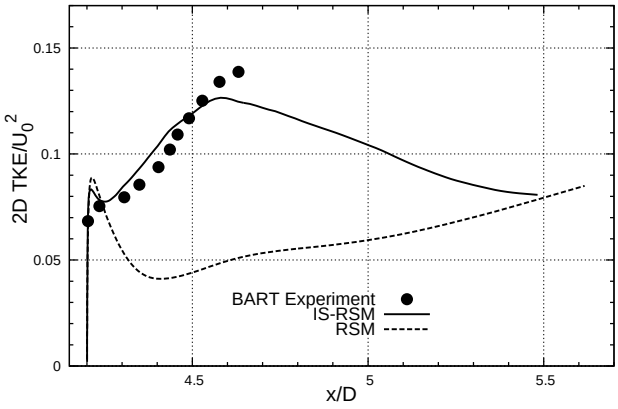

Figure 4.47: Centreline $2D$ turbulent kinetic energy in the wake for $L/D = 3.7$

has been done for the JH-RSM simulations and the grid was refined in three steps from 60000 to 120000 and finally to 300000 cells with no real convergence in one particular direction. The results were all similar but no trend could be observed. This is also an indication for the highly unsteady case which is simply not suitable for baseline RANS.

4.6.2 Short distance case $L/D = 1.435$

The testcase with the short distance in-between the cylinders is different from the large distance case, with the flow detaching from the first cylinder and reattaching on the second. Therefore, profiles of flow quantities plotted on the centreline are only of interest behind the second cylinder. The large distance case was very hard to predict successfully by the JH-RSM, as was shown in the previous section. This is also partly true for the short distance case. One problematic effect, the bistable vortex street in-between the cylinders, can be neglected here since the cylinders are very close to each other. Nevertheless, this testcase also suffers from high unsteadiness of the separations on the upper and lower surfaces of the second cylinder, with a developing vortex street. Therefor it can be expected that by using the IS-RSM the results should improve, similar to the large distance case. The grid used for the short distance was designed according to observations made for the large distance case. Again 60000 cells have been used in the xy-plane,

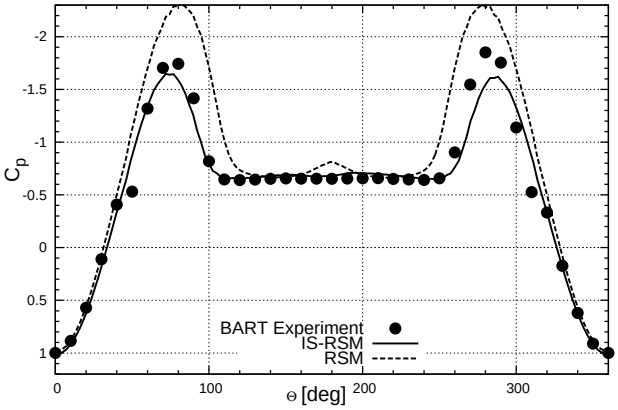

Figure 4.48: Pressure coefficient on the first cylinder for $L/D = 3.7$

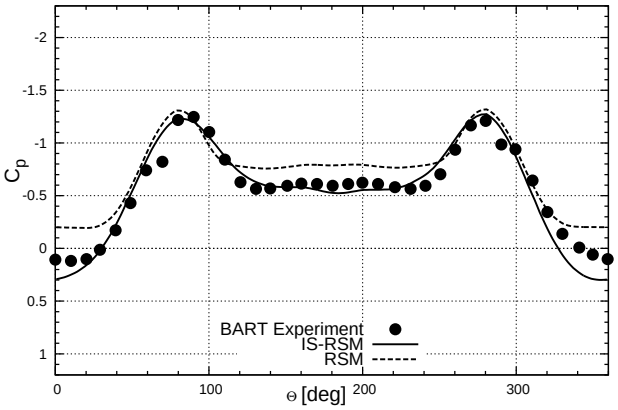

Figure 4.49: Pressure coefficient on the second cylinder for $L/D = 3.7$

while for the IS-RSM the grid was extruded in the spanwise direction by the amount of two diameters and 80 cells. Fig. 4.50 shows the normalized mean streamwise velocity U/U_0 on the centreline behind the second cylinder. As can be seen the JH-RSM underpredicts the recirculation zone behind the cylinder by far, which is indicated by negative streamwise velocity. This is qualitatively close to the results for the large distance case behind the first cylinder. The IS-RSM shows nearly the correct length of the recirculation zone. Also the shape follows the reference experimental data well. Fig. 4.51 shows the normalized $2D\ TKE$ on the centreline behind the second cylinder. The RSM highly overpredicts this quantity, with a totally wrong slope in its profile starting directly from the cylinder surface. This is of course not the intended results, but at least coincides with the short recirculation zone. The baseline RANS is unable to cope with the unsteady interactions of the three-dimensional flow field. Obviously these interactions have to be captured in order to predict the flow correctly. By using the IS-RSM the turbulent kinetic energy is somewhat overestimated, but still much closer to the reference data. It is also in good qualitative agreement concerning the correctness of the peak location in respect to the distance from the cylinder.

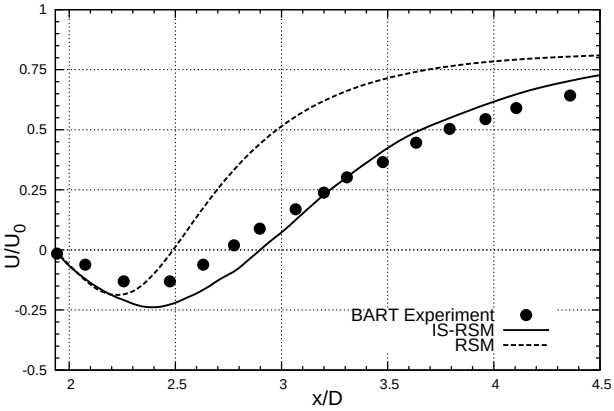

Figure 4.50: Mean normalized centreline velocity for $L/D = 1.435$

Fig. 4.52 and 4.53 show the normalized mean pressure coefficient on both surfaces of the cylinders. For the long distance as well as for the short distance, C_p is the only quantity computed by the RSM, which at least has a very similar distribution as in the experiments. Also the IS-RSM agrees

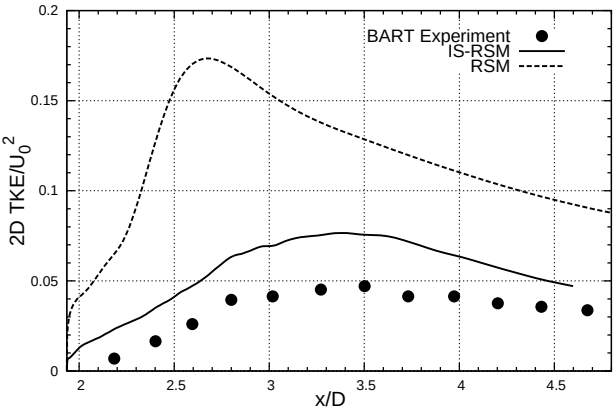

Figure 4.51: Centreline $2D$ turbulent kinetic energy for $L/D = 1.435$

well with the reference data. No more detail can be given in terms of C_p, since the pressure distribution on the second cylinder reveals an asymmetry, in terms of suction peaks in the reference data [37]. A misalignment could not safely be ensured in the experiments due to the very short distance in-between the cylinders. Therefore, no absolute value for C_p can be given.

4.6.3 Root mean square of surface pressure distribution

Since the tandem cylinders should mimic a landing gear, it is of special interest to correctly predict the strength of the acoustic field coming from the cylinders, as a result of the interaction with the flow. A lot of noise during landing comes from the landing gear. The root mean square of the pressure, $(C_p)_{rms} = p_{rms}/(\frac{1}{2}\rho U_0^2)$, with $p_{rms} = \sqrt{\overline{p' p'}}$ and p' being the instantaneous pressure, serves as a quantity to measure the strength of the acoustic field. The turbulent flow field, which hits the landing gear, separates and reattaches in highly unsteady points has a direct impact on the lift and drag coefficient, which then leads to noise development. The strongly varying lift and drag can be captured through the pressure field. Which finally brings us to $(C_p)_{rms}$ as a measurement of the unsteady pressure field. By definition the unsteady interactions in the turbulent flow field must be captured accurately to give a good representation of the strength

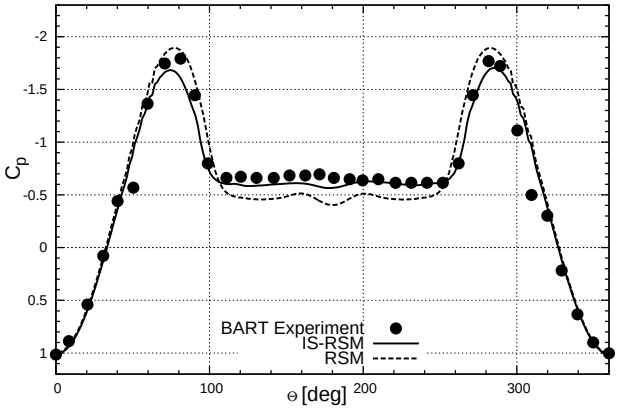

Figure 4.52: Pressure coefficient on the first cylinder for $L/D = 1.435$

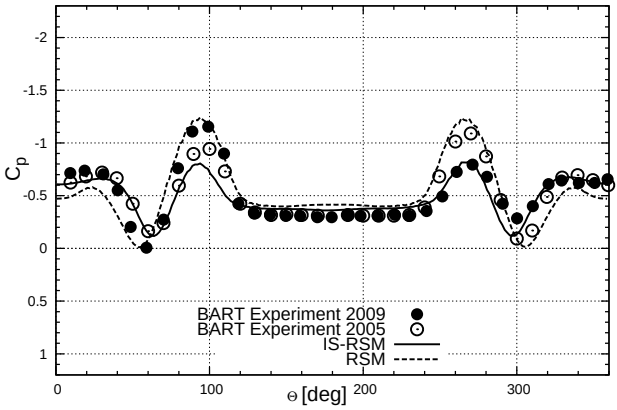

Figure 4.53: Pressure coefficient on the second cylinder for $L/D = 1.435$

of the acoustic field. As for both distance cases the noise coming from the second cylinder is much more intense than the one from the first, $(C_p)_{rms}$ is shown in Fig. 4.54 and 4.55 only on the second cylinder. Obviously the JH-RSM is neither able to predict the peaks nor the distribution of $(C_p)_{rms}$ for both testcases while the IS-RSM shows excellent results. The RSM cannot capture the unsteady interactions of the eddies with sufficient accuracy due to the complete lack of any smaller eddies. For the $(C_p)_{rms}$ it is necessary to capture a broader range in size and frequency of the interacting eddies. Trying to model them has proven mostly unsuccessful, at least concerning the strength of the acoustic field.

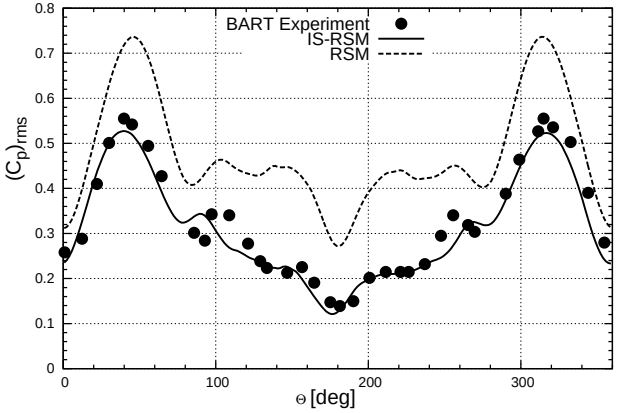

Figure 4.54: Root mean square of pressure on the second cylinder - performance of different models for $L/D = 3.7$

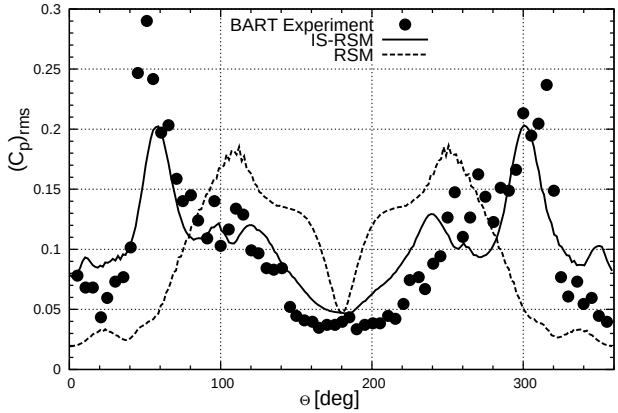

Figure 4.55: Root mean square of pressure on the second cylinder - performance of different models for $L/D = 1.435$

5 A RANS RSM model accounting for selective turbulence production enhancement

This chapter gives another interpretation of Rotta's kL model in a manner similar to the approach taken by Menter and Egorov [35] in deriving the equations for the SAS model. It is divided into some analysis of the term Rotta modeled by applying the Taylor expansion series and which finally lead to the introduction of the ratio of first to second derivatives of the velocity field, and results obtained by applying a different approach in modeling this term. First of all, as a reminder, the negative sign in front of the originally proposed term by Rotta which contains the third derivative, was chosen to fulfill the log-law. This is one of the reasons why the term containing the second derivative was seen as superior as explained in [35]. Choosing a negative sign for a constant is not the natural way and not straightforward to justify [35]. The statement seems true, but at least for the modeling procedure presented here it is not quantitatively relevant, as will be shown later. Furthermore, this term, which was introduced to distinguish between different length scales in the flow [35], should be more important in difficult flow regimes which were traditionally hard to simulate accurately, like for example large separation from curved surfaces with highly oscillating separation and reattachment points. The logarithmic law could be reproduced with nearly any, more sophisticated turbulence model. Let's think about what happens with the term containing the integral form in the Taylor expansion series. This term, if analyzed around the separation from a curved surface, is strictly negative with R_{12} being negative and the second velocity derivative being positive. Especially close to separation points the term should be really important, due to the high bending of the velocity profile. Based on that it can be argued that a negative sign in front of the model of the term should be more adequate, compared to the positive sign, which fulfills the log-law but, vice versa, not the parts where it was intended to help compared to models bearing only one length scale source.
Basically what the SAS term is doing, either in its original form out of the

$k\omega$-SST-SAS or the modified one from the IS-RSM, is that it detects high ratios between first and second derivatives and increases the production in the ω-equation. The SAS term is nothing else than an extra production blended with the ratio of the derivatives. Since ω increases, the ratio of ϵ/k has to increase and k/ϵ has to decrease, which leads to reduced model values and consequently to the ability to resolve flow structures since damping effects through the model vanished partly. This behavior makes the question whether the log law can be correctly obtained or not irrelevant, since the flow field is globally resolved and the prediction of the log-law relies on the correct capturing of the resolved turbulence. The JH-RSM(-P_{SAS}) model, which will be introduced in this chapter, detects high ratios between second and first velocity derivatives, as they occur around separation points on curved surfaces, and decreases the production of ω, because of its flipped sign, thus leading to increased model values of the Reynolds stresses. It has the form of a blended negative production. The goal is to remedy with this term the misbehavior most models show in the case of strong separation from curved surfaces, namely the large underprediction of the Reynolds stresses in the separating shear layer and consequently the overprediction of the recirculation zone. It is not completely *ad hoc* and is based on Rotta's integral length scale model with assumption, that the sign in front of the term containing the second velocity derivative and the Reynolds shear stress can be estimated through its behavior in separating shear layers. As will be shown, the term is very small anyway in the log-law area. Of course it should play no role in parts of the flow regime which could have been already well predicted by the baseline JH-RSM. This should be ensured. By its very nature the term is important only when the production of ω^h is high and the ratio of the second to the first velocity derivative is high, since it blends the ω^h production with the derivatives ratio. "Important" means that it is quantitatively in the range of the production of ω^h, while the production itself has to be of course relevant in the transport equation of ω^h. Fig. 5.1 shows (-P_{SAS}) together with velocity crossplots for the 2D Hill case at the position $x/H = 0.5$. The term starts with its major impact somewhat later then the separation point near the crest of the first hill and then convects to an area with high production of ω^h, which is expected, since production and blending due to velocity derivatives are the main parts of the (-P_{SAS}) term. The reason why the high bending of the velocity profile directly in the separation point is not accounted for or not detected, is because of the protection inside the (-P_{SAS}) term which was designed to help the eddy-resolving models models to go back to RANS mode close

to walls. What the (-P_{SAS}) term actually recognizes is the high bending in the velocity profile just before the streamwise velocity drops down to negative values. The area with high bending is marked in Fig. 5.1. It shifts to regions of high production rates of ω^h (P describes the production of ω^h) and consequently to high first velocity derivatives as can be seen in Fig. 5.2 for the position $x/H = 1.2$. Actually it is quite smart to attack the second high bending area with the $(-P_{SAS})$, since that one due to separation is inside the boundary layer, which should not be disturbed by the model. For the flow over a backward-facing step, which contains massive separation, the (-P_{SAS}) has less impact for the following two reasons: the reduced second velocity derivative and the increased first derivative. The bending in the marked area of Fig. 5.1 shows high second derivatives and low first derivatives of the velocity to be the nature of continuous separation from the curved surface. The same velocity profile is shown in Fig. 5.3 for the backstep right after separation at the position $x/H = 0.5$. Due to separation from the fixed point the whole velocity profile is suddenly pulled downwards through the lower wall of the backstep which leads to an increase of the first derivative and a decrease of the second one.

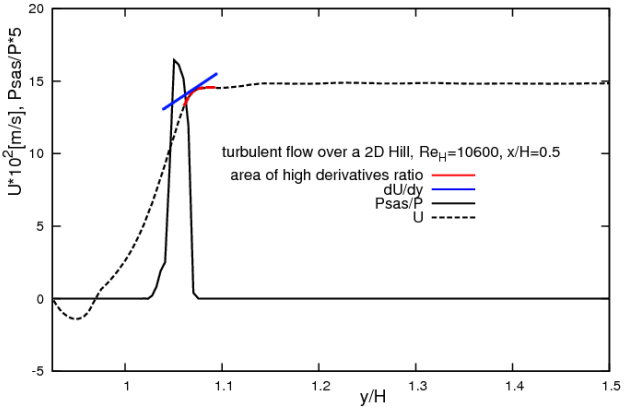

Figure 5.1: Illustration of $(-P_{SAS})$ impact on 2D Hill flow - $x/H = 0.5$ and $Re_H = 10600$

Fig. 5.6 to 5.9 show the ratio between $(-P_{SAS})$ and the production of ω^h, $\left|\frac{(-P_{SAS})}{P}\right|$ for the simulated flow over a 2D Hill, over a backward-facing step, for the 3D Diffuser and the turbulent mixing layer. Concerning

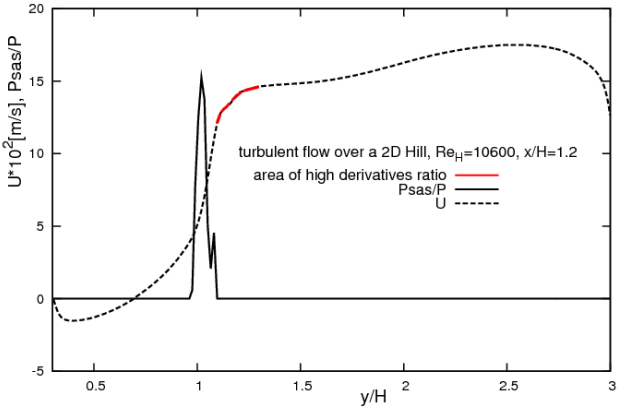

Figure 5.2: Illustration of $(-P_{SAS})$ impact on 2D Hill flow - $x/H = 1.2$ and $Re_H = 10600$

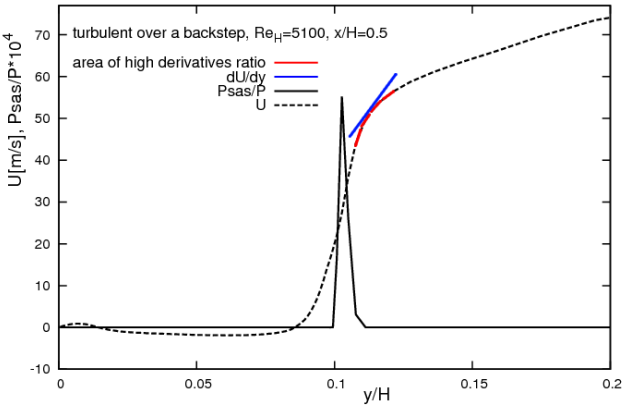

Figure 5.3: Illustration of $(-P_{SAS})$ impact on backstep flow - $x/H = 0.5$ and $Re_H = 5100$

the mixing layer case Fig. 5.6 shows a zoom into the area of interest, namely the very high shearing zone at the beginning immediately after the inlet. Each simulation has been done in conjunction with the JH-RSM($-P_{SAS}$). All cases contain different kinds of bending of the velocity profile. The backward-facing step and the mixing layer can be predicted with sufficient accuracy by the JH-RSM without modification. The results should not change while including the ($-P_{SAS}$) term since that would mean it has negative side effects. To distinguish more accurately between velocity profile bending due to flow separation and due to mixing out of two streams with the same flow direction, the Reynolds stress anisotropy parameter A has been introduced as a barrier for the impact of the ($-P_{SAS}$) (for example switching the term off for $A < 0.2$). It seems that a separated flow, which recirculates and hits back with a different flow direction into the main stream, is a lot more isotropic exactly beneath the separation point than the simple mixing out of two streams with the same flow direction but totally different magnitude. The latter case leads to a dramatic increase of the normal stress component in the streamwise direction, and therefor to high Reynolds stress anisotropy. Fig. 5.4 and 5.5 show the effect explained above by means of A for the 2D Hill case and the mixing layer.

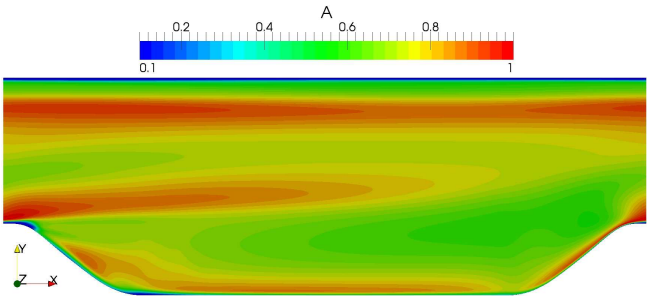

Figure 5.4: Anisotropy parameter for the 2D Hill

After the introduction of the sensitivity parameter A, the term is ready to work with. After some recalibration of the constants, which in have in fact been set up for the correct behavior of the IS-RSM, the final version

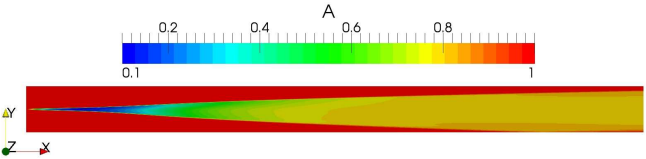

Figure 5.5: Anisotropy parameter for the turbulent mixing layer

reads:

$$(-P_{SAS}) = -0.0055\text{max}\left(1.755\kappa S^2\left(\frac{L}{L_{vk}}\right)^{1/2} - 20T_2, 0\right),$$
$$T_2 = \frac{k}{1/3}max\left(\frac{1}{k^2}\frac{\partial k}{\partial x_j}\frac{\partial k}{\partial x_j}, \frac{1}{\omega^h\omega^h}\frac{\partial \omega^h}{\partial x_j}\frac{\partial \omega^h}{\partial x_j}\right). \tag{5.1}$$

As can be seen in Fig. 5.8 and 5.9 $\left|\frac{(-P_{SAS})}{P}\right|$ is a lot higher for the 2D Hill and the 3D Diffuser when compared to the backstep and the mixing layer. Consequently the basic concept seems to work. Still the magnitude of the effect has to be examined by analyzing the flow topology carefully for each testcase.

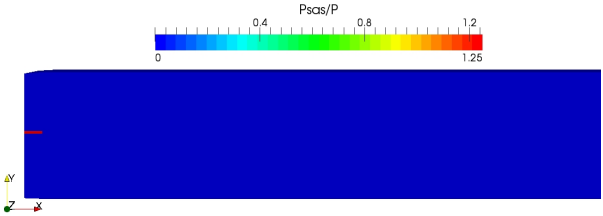

Figure 5.6: Production ratio for the turbulent mixing layer

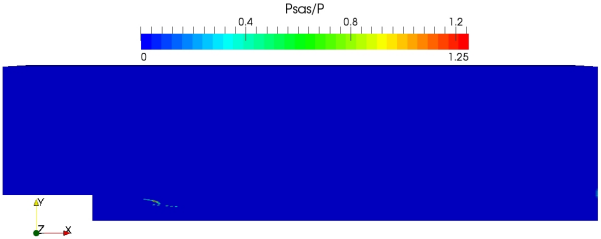

Figure 5.7: Production ratio for the flow over a backward-facing step

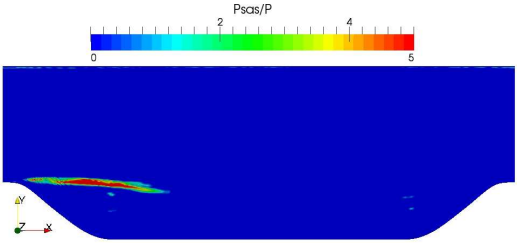

Figure 5.8: Production ratio for the 2D Hill

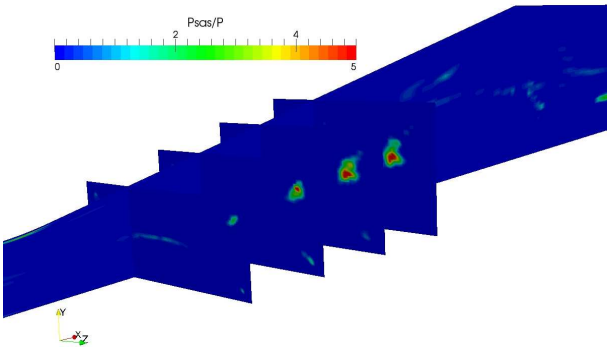

Figure 5.9: Production ratio for the flow through a 3D Diffuser

5.1 Testcase results with the JH-RSM($-P_{SAS}$)

In the following the results obtained with the JH-RSM($-P_{SAS}$) for different testcases will be shown in terms of crossplots and contour plots of different calculated quantities. The testcases consist of the 2D Hill with two different Reynolds numbers, the flow over a backward-facing step, the turbulent channel flow with $Re_\tau = 395$, the turbulent mixing layer and the flow in a 3D Diffuser.

5.1.1 Turbulent channel flow

Fig. 5.10 shows the normalized velocity U^+ over y^+ for the turbulent channel flow. The results of the JH-RSM($-P_{SAS}$) coincide with the baseline Reynolds stress model. Not only the velocity but also the stress components, shown in Fig. 5.11 by means of the normal components in normalized form, did not change.

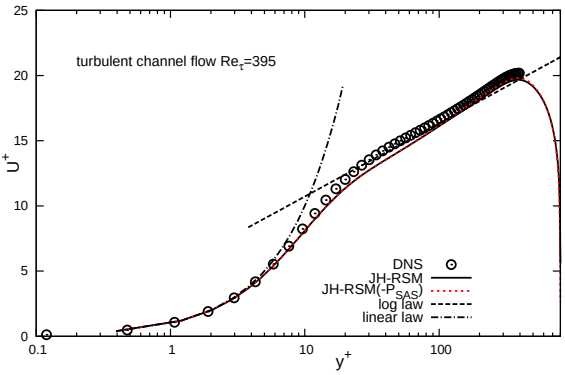

Figure 5.10: Streamwise mean velocity for the turbulent channel flow with $Re_\tau = 395$ - computation with the ($-P_{SAS}$) model

The part where the ($-P_{SAS}$) is active is very small compared to the whole domain. Fig. 5.12 shows the ratio of the extra production term ($-P_{SAS}$) over the production in the ω^h-equation. In the log layer which ranges from approximately y^+=30 to 100 the term plays no role compared to the production of ω^h. It is in order of magnitude compared to the production right in the middle of the channel at $y^+ = 395$, as can be seen

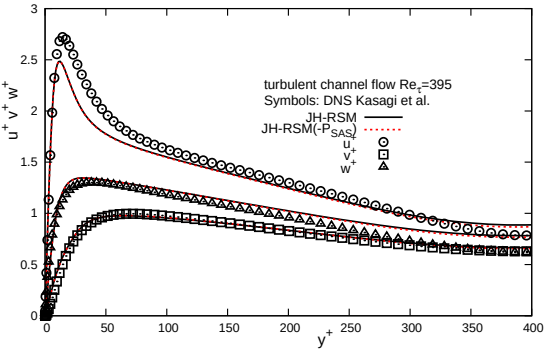

Figure 5.11: normal stress components for the turbulent channel flow with $Re_\tau = 395$ - computation with the $(-P_{SAS})$ model

in Fig. 5.12. Actually at this point P itself becomes unimportant and thus the $(-P_{SAS})$ as well.

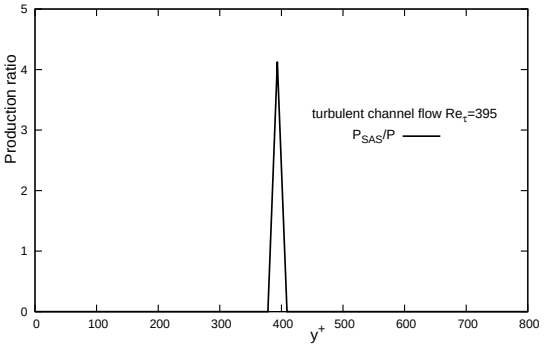

Figure 5.12: Quantitative illustration of the production ratio for the turbulent channel flow - $Re_\tau = 395$

5.1.2 Turbulent mixing layer

The turbulent mixing layer is very different from the channel flow. Fluid enters the computational domain with two different block velocity profiles and an imposed gradient in-between them as can be seen in Fig. 5.13. Then the upper and lower layer start mixing and finally after some time a self similar flow state develops. Compared to the channel flow, high bending of the velocity profile occurs during the mixing process. Nevertheless, this bending is differently pronounced than for the separation point on curved surfaces in terms of the Reynolds stress anisotropy parameter A, as already explained. The $(-P_{SAS})$ term should be able to react to that. The reference data for the mixing layer is taken from the experiments of Spencer [50] [38] and contains normalized streamwise velocity, turbulent kinetic energy and Reynolds shear stress at different points in the streamwise direction. To get a better impression of the case the reader is referred to Fig. 3.4 which shows the domain with the computed streamwise velocity. On the upper and lower bound symmetry boundary conditions were imposed with fixed uniform inlet velocities at the inlet and zero gradient at the outlet. The flow direction is from left to right.

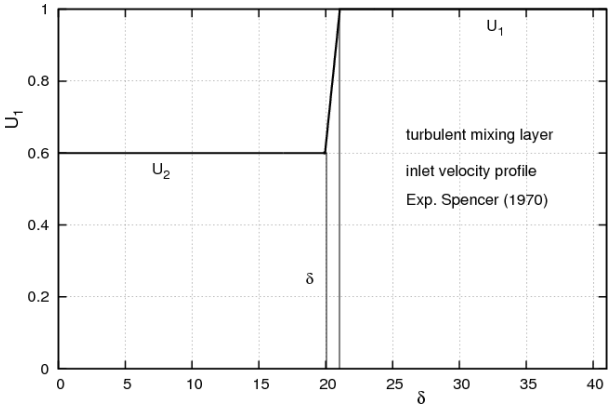

Figure 5.13: Inlet velocity profile for the turbulent mixing layer

Fig. 5.14, 5.15 and 5.16 show crossplots of the normalized velocity, normalized turbulent kinetic energy and normalized Reynolds shear stress over the normalized mixing layer height. Results obtained with the JH-RSM and the $(-P_{SAS})$ version are compared to the experimental reference data. Only the last point in the streamwise direction $x/\delta = 400$, with δ being

the size of the shear layer thickness at the inlet, is shown since the others contain similar information. The normalized mean velocity profiles calculated by both turbulence models are very close to the reference data. The turbulence quantities predicted by the ($-P_{SAS}$) version are slightly higher, which actually brings them closer to the reference data, at least concerning the turbulent kinetic energy.

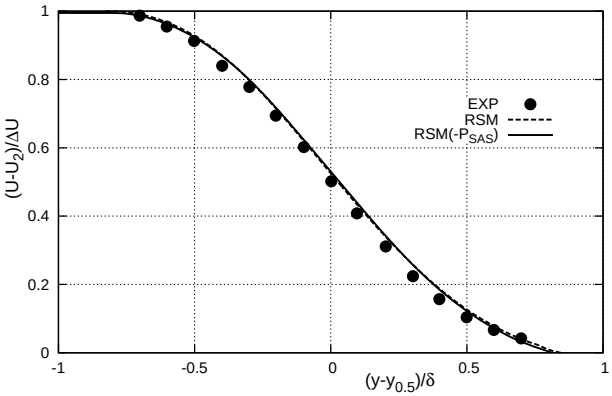

Figure 5.14: Normalized streamwise velocity at $x/\delta = 400$ - computation with the ($-P_{SAS}$) model

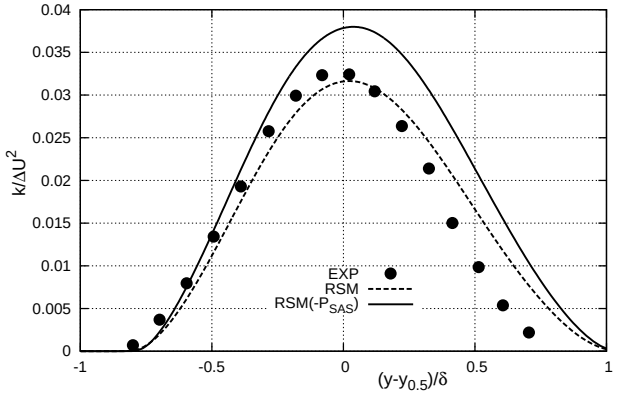

Figure 5.15: Normalized turbulent kinetic energy at $x/\delta = 400$ - computation with the $(-P_{SAS})$ model

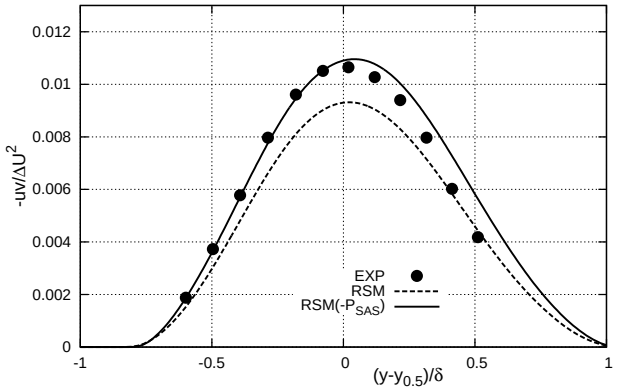

Figure 5.16: Normalized turbulent shear stress at $x/\delta = 400$ - computation with the $(-P_{SAS})$ model

5.1.3 Flow over a backward-facing step

The turbulent channel flow and the turbulent mixing layer are both attached flows. The backward-facing step is a flow case with separation from a fixed point marked by the step edge. The ($-P_{SAS}$) model was introduced to account for the effects that appear during separation from curved surfaces by detecting high bending of the velocity profile, which occurs especially when the separation takes place in a tiny space and develops continuously. The flow in the backstep case separates suddenly, which leads to a mild bending of the velocity profile as illustrated in Fig. 5.3. The JH-RSM($-P_{SAS}$) should also be able to detect that and therefor adjust itself to a value which has less importance in the ω^h equation. The backstep with its geometry, boundary conditions and crossplots of different quantities has already been discussed in detail in the previous chapters. Fig. 5.17 shows normalized mean streamwise velocity profiles, obtained with the baseline RSM and the ($-P_{SAS}$) model, plotted over the step height at different streamwise positions. Obviously both turbulence models catch the profiles from the reference DNS and the experimental data very well in terms of distribution and peak values. The length of the recirculation zone behind the step, which is marked by the negative streamwise velocity, is in good agreement.

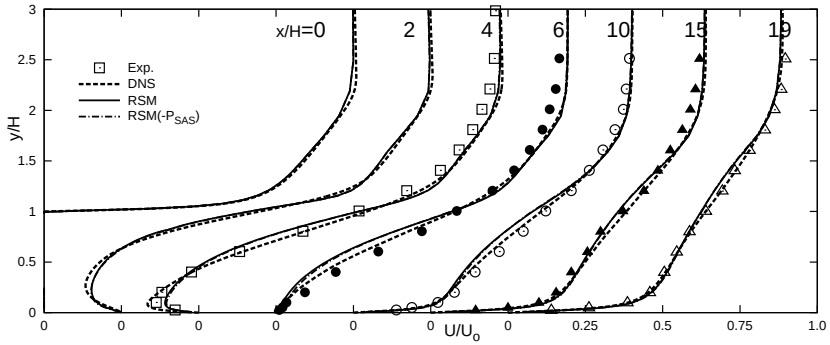

Figure 5.17: Normalized streamwise velocity for the backstep flow with $Re_H = 5100$ - computation with the ($-P_{SAS}$) model

Fig. 5.18 shows distributions of the normalized stress $u^{'}/U_0$ at different streamwise positions over the step height as a measure of turbulence intensity in the separating shear layer. Right from the beginning behind

the step, at the position $x/H = 2$, the JH-RSM underestimates $u^{'}/U_0$ compared to the DNS but then quickly recovers to proper values in the ongoing separating shear layer. Due to this quick recovery the recirculation zone is of correct length. The JH-RSM($-P_{SAS}$) starts with slightly higher values of $u^{'}/U_0$ right behind the step. As intended, the obtained flow quantities calculated with both turbulence models are very similar.

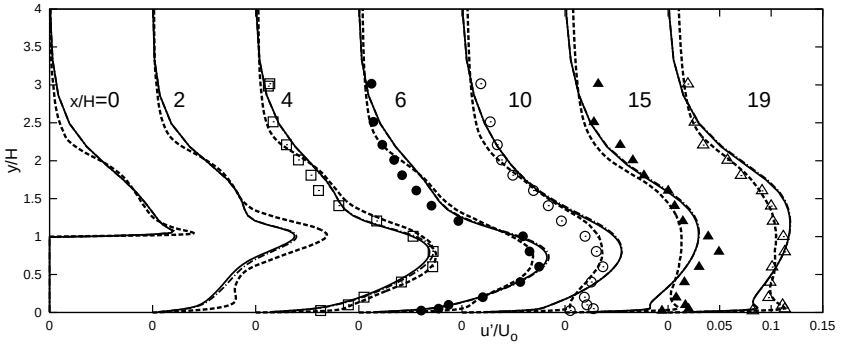

Figure 5.18: Normalized $\overline{uu}$ stress component for the backstep flow with $Re_H = 5100$ - computation with the ($-P_{SAS}$) model

5.1.4 Turbulent flow over a 2D Hill

So far the model has shown good performance for cases with no separation or separation from fixed points, where the bending of the velocity profile is not extremely high. In the following the cases with separation from curved surfaces, namely the 2D Hill with the two Reynolds numbers 10600 and 37000 and the 3D Diffuser will be in the focus of the modification to the JH-RSM in line with the ($-P_{SAS}$) term. The results for these cases in conjunction with the JH-RSM are highly inadequate. The consequence is an underestimation of the turbulence quantities and overestimation of the recirculation zone for the 2D Hill case and a wrong place of the recirculation zone, with separation in the upper right and lower right corner in the case of the 3D Diffuser. If the JH-RSM is used together with the ($-P_{SAS}$) concept the situation improves a lot. This can be seen in Fig. 5.20 and 5.21 for the two different 2D Hill testcases, where the normalized mean streamwise velocity is shown at different points in the streamwise direction over the hill height. The whole velocity distribution follows the reference data nicely, while the JH-RSM underestimates the acceleration peaks on top of the first hill and overestimates the region where the flow separates. To get a better impression of the direct impact of ($-P_{SAS}$), Fig. 5.19 shows the shortened recirculation zone obtained with the JH-RSM($-P_{SAS}$) compared to the baseline RSM by means of streamlines through the hill geometry for the lower Reynolds number case. The reference reattachment point is marked red. The distribution of the streamwise velocity profiles is a consequence of correctly capturing the turbulence quantities in the separating shear layer. Fig. 5.22 and 5.23 show shear stress profiles and Fig. 5.24 and 5.25 normal stress profiles in the streamwise direction at different streamwise positions for both Reynolds numbers. With the JH-RSM($-P_{SAS}$) the turbulence quantities increase rapidly after separation at $x/H = 0.24$ up to the reference values from the LES or the experiments in the separating shear layer at the positions $x/H = 0.5$, 1, 2 and 4. Those are exactly the positions where the JH-RSM dramatically underpredicts the turbulence quantities. High turbulence intensity in that area leads to fast mixing and then to a shorter recirculation zone. The ($-P_{SAS}$) is able to recognize the separation point and increase the production there. This is accompanied by a transport process of this extra production along the separating shear layer.

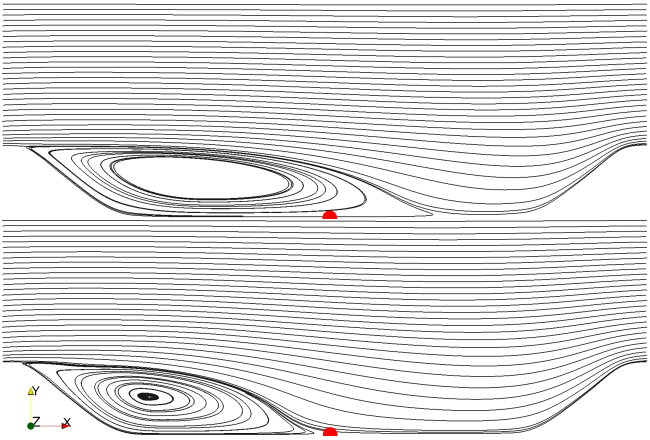

Figure 5.19: Illustration of the flow pattern for the 2D Hill with $Re_H = 10600$ - upper streamlines: RSM, lower streamlines: RSM($-P_{SAS}$)

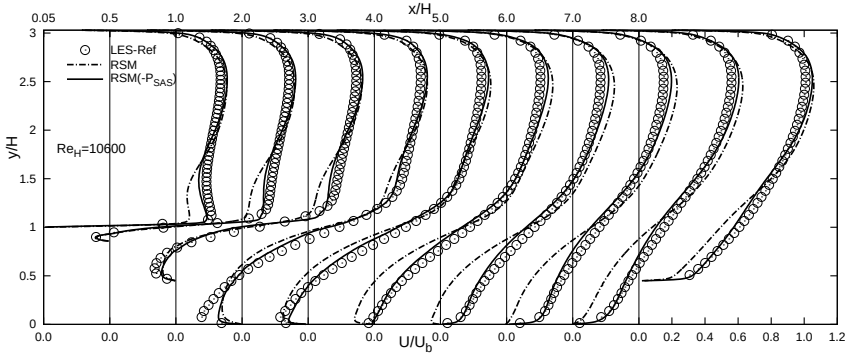

Figure 5.20: Normalized streamwise velocity for the 2D Hill with $Re_H = 10600$ - computation with the ($-P_{SAS}$) model

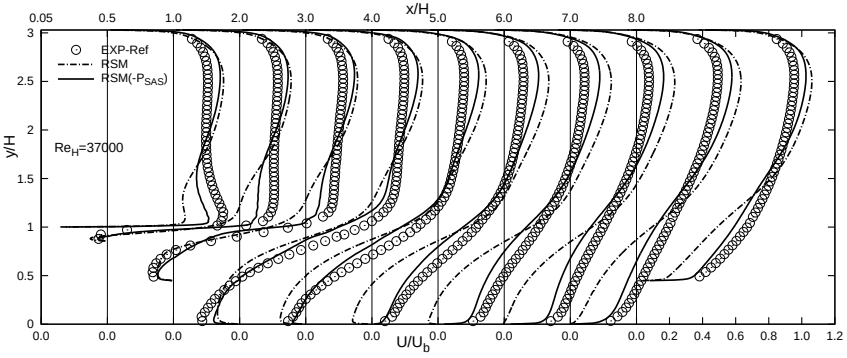

Figure 5.21: Normalized streamwise velocity for the 2D Hill with $Re_H = 37000$ - computation with the $(-P_{SAS})$ model

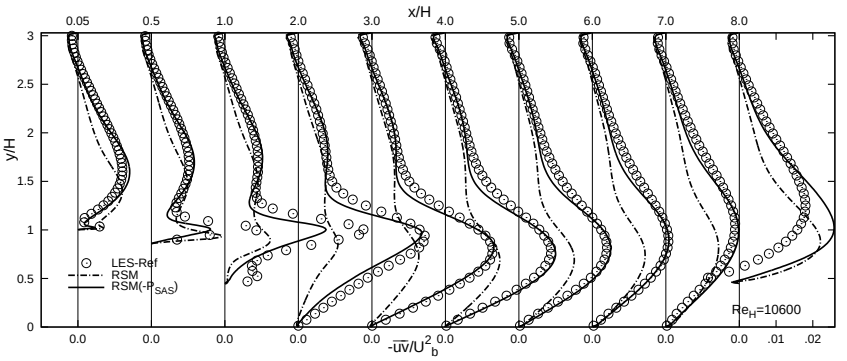

Figure 5.22: Normalized turbulent shear stress component for the 2D Hill with $Re_H = 10600$ - computation with the $(-P_{SAS})$ model

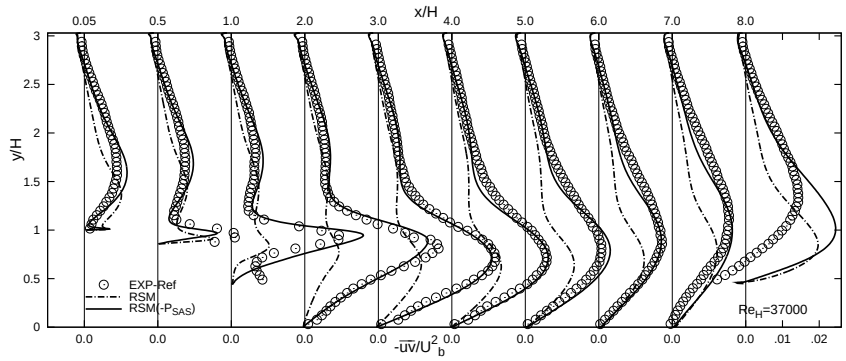

Figure 5.23: Normalized turbulent shear stress component for the 2D Hill with $Re_H = 37000$ - computation with the $(-P_{SAS})$ model

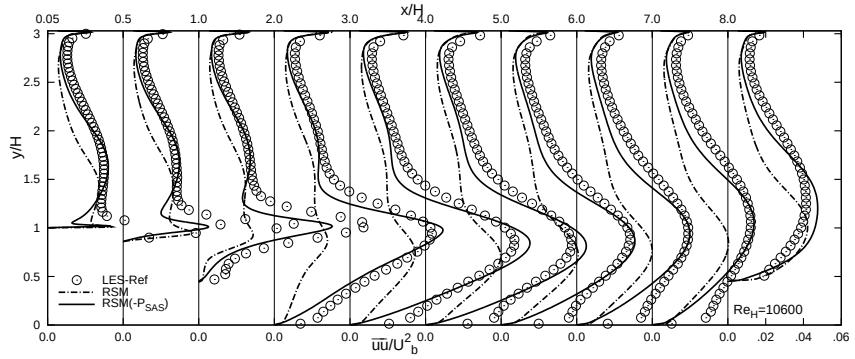

Figure 5.24: Normalized $\overline{uu}$ stress component for the 2D Hill with $Re_H = 10600$ - computation with the $(-P_{SAS})$ model

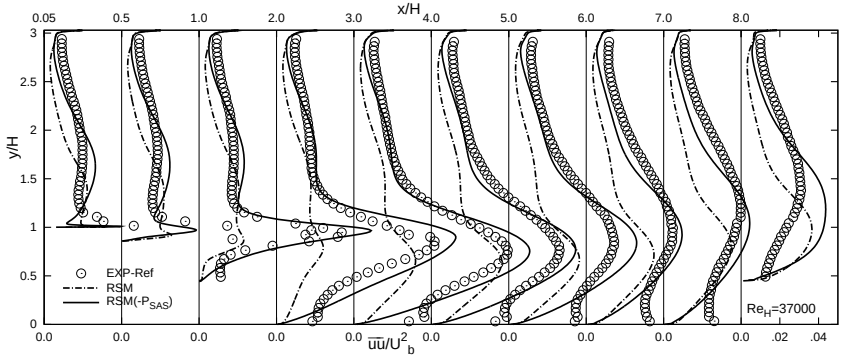

Figure 5.25: Normalized $\overline{uu}$ stress component for the 2D Hill with $Re_H = 37000$ - computation with the ($-P_{SAS}$) model

5.1.5 Turbulent flow in a 3D Diffuser

The 3D Diffuser suffers from separation from two curved surfaces, namely the upper and the right wall. It is not only a matter of correctly capturing the separation process in terms of rapid increasing Reynolds stresses, but also of predicting the flow in the rectangular inlet duct in terms of wall approximation behavior and core flow distribution. The JH-RSM predicts the separation process starting in the upper right corner, then moving slightly to the upper wall and then again back to the upper right corner while also the lower right corner largely separates. The regions with separating flow are shown in Fig. 5.26 as isocontours of the velocity, while the zero velocity contour is highlighted.

By including the ($-P_{SAS}$) term the turbulence intensity increases somewhat in the areas of separation from curved surfaces, which is for the diffuser the upper right corner at the beginning. Since the JH-RSM tends to predict separation along the diffuser close to the right wall, this procedure is blocked by the increased turbulence intensity in the upper right corner. This leaves some space for the separation process to develop to the correct position, namely the upper wall. This behavior is also shown in Fig. 5.26. As a consequence of the improved flow situation by means of separation behavior, the distribution of C_p on the lower wall improves also and is now very close to the experimental distribution as can be seen in Fig. 5.27. The JH-RSM underestimates the pressure recovery.

So far the JH-RSM($-P_{SAS}$) model has been tested on some flows includ-

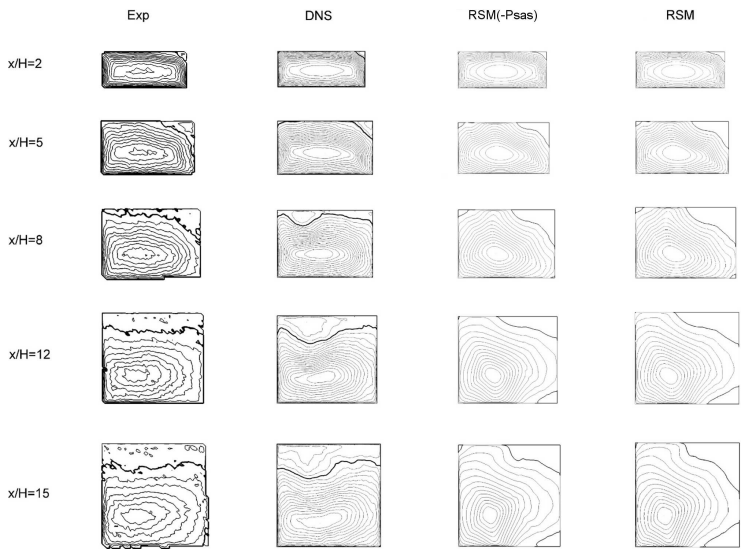

Figure 5.26: Iso contours of the streamwise velocity at five characteristic cutting planes through the diffuser - performance of the $(-P_{SAS})$ model

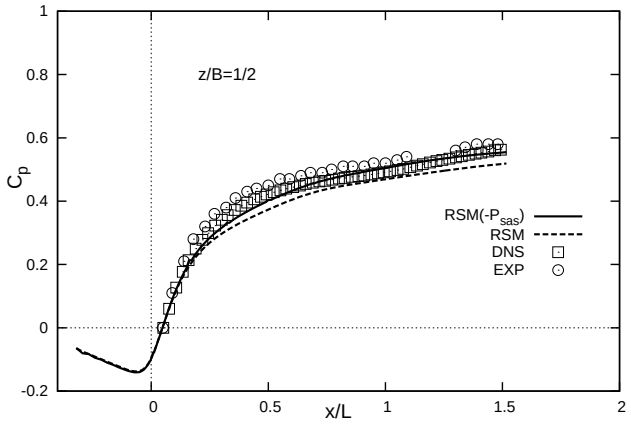

Figure 5.27: Pressure coefficient on the lower diffuser wall - performance of the $(-P_{SAS})$ model

ing separation from curved surfaces, separation from fixed points and flows with no separation but with high bending of the velocity profile like the turbulent mixing layer. At least for these cases it has shown good agreement with the reference data. No greater change was observed for flow situations where the JH-RSM is already capable to predict most of the flow quantities with sufficient accuracy. Contrary to that major improvement was observed for cases with separation from curved surfaces, introducing increased turbulence intensity in the separation point. A better prediction of the recirculation zone was the direct consequence. Of course some more testcases should be simulated to cover a broader range of flow phenomena.

6 Conclusions and Outlook

In this work an eddy-resolving Reynolds stress model, IS-RSM, has been developed which is based on the introduction of the von Karman length scale consisting of the ratio between second and first velocity derivatives. The model detects instabilities due to the increased ratio of the second to the first velocity derivative, and increases the production of the specific dissipation rate in those areas. Accompanied by that is a decrease of modeled turbulent kinetic energy and Reynolds stresses since the dissipation is a destruction term in their transport equations. Once the modeled quantities are reduced the simulation changes its behavior from a RANS like to a LES like approach, allowing for turbulent flow structures to be resolved. This captures the instantaneous character of the flow, thus increasing in a widespread manner the ratio between second and first velocity derivatives and so containing a self sustaining mechanism. The concept of introducing the von Karman length scale to trigger a turbulence model into structure resolving mode has been invented by Menter and co-workers [36] [34] and has been called scale adaptive simulation SAS. Some features have been given by this group to distinguish the SAS concept from other hybrid LES/RANS models [12]:

- Provide proper RANS performance in stable flow regions.
- Allow the break-up of large unsteady structures into a turbulent spectrum.
- Provide proper damping of resolved turbulence at the high wave number end of the spectrum (resolution limit of the grid).

It has been shown by means of different testcase simulations that the IS-RSM is indeed capable to switch into structure resolving mode with the ability to capture flow features under difficult flow conditions, like separation from curved surfaces, correctly. Contrary to the $k\omega$-SST-SAS which uses in its latest version the square of the ratio between the turbulent length scale and the von Karman length scale, the IS-RSM uses the square-root. The square originally introduced with the aim to detect homogeneous directions in terms of turbulence quantities, is in fact a triggering mechanism

for regions with high ratios of the second to the first velocity derivative and a damping one for vice versa conditions. It has to be said that once the model switches into structure resolving mode, no homogeneous direction can exist for the turbulence quantities but only for their statistics, which cannot be detected by such a modification. The square-root introduced with the IS-RSM is able to increase the derivatives ratio for quite stable flow regions with low von Karman length scale, while it somewhat dampens regions with already high ratios. The triggering mechanism is therefor more widespread in all flow regions but lower in its peak compared to taking the square of the ratio. This aspect is important with respect to turning the model into structure resolving mode under quite stable flow conditions.

By stabilizing the background Reynolds stress model (JH-RSM) with remodeling of the $P_{\epsilon,3}$-term, very high convection schemes could be applied to the IS-RSM. This led to the model being also able to switch into structure resolving mode for stable flow conditions (channel flow, duct flow). This distinguishes the IS-RSM from the SAS concept, which is the reason why the expression I(nstability) S(ensitive) has been chosen.

In the last part of this work a separation sensitive conventional RANS model has been developed by including the von Karman length scale to the ω^h equation but with the negative sign, noted as $(-P_{SAS})$. In regions where separation occurs the bending of the velocity profile increases and thus the ratio between first and second velocity derivatives. With the negative sign, exactly in those regions ω^h is reduced and therefor the modeled turbulent kinetic energy and the Reynolds stresses are increased. It has been explained that the positive sign in front of the original term which results from the need of matching the behavior in the logarithmic layer, in fact stands in no relation to that. The reason being that in a structure resolving simulation the proper correlation between the turbulent eddies has to be fulfilled to match the logarithmic layer. With a closer look to regions around detaching points it appears that the negative sign in front of the term should be more appropriately by means of conventional RANS simulations. With the JH-RSM($-P_{SAS}$) different testcases including separation from fixed points, from curved surfaces and testcases with no separation but with high bending of the velocity profile have been computed with encouraging results. These showed no difference compared to the results of the standard JH-RSM in case with no separation where the JH-RSM produces already accurate results. However large improvement in the results of separated flows from curved surfaces could be attained, which now show much better behavior in terms of turbulence quantities as well as

recirculation zone shape and length.

Finally it has to be said that the two developed models, the IS-RSM and the JH-RSM($-P_{SAS}$), differ basically only in the sign in front of the term but this difference is accompanied by a large difference in simulation behavior and cost. One model was designed to resolve turbulent flow structures and therefor always needs three-dimensional computational domains and unsteady calculations with small time steps. The other model however was designed to work in steady RANS mode or in URANS mode with large ensembles. In the end it is the decision of the user whether it is necessary to resolve the unsteadiness with a instability sensitive model which, if properly used, leads to more accurate results but also needs a lot more effort. On the other hand it can be enough to capture only the mean flow characteristics which can be done accurately enough with the help of the ($-P_{SAS}$) term, at least for separated flows from curved surfaces.
For future work a hybrid numerical scheme can be introduced which fulfills the different needs of RANS and LES. The large eddy simulation always requires high numerical schemes for the convective terms, while in general RANS, due to extreme cell aspect ratios, needs lower order schemes to damp out numerical instabilities. Of course the IS-RSM shows a continuous shift between RANS and LES with no classically sharp distinction between the two zones. Nevertheless, the second part of the SAS term,

$$T_2 = \frac{k}{1/3} max\left(\frac{1}{k^2}\frac{\partial k}{\partial x_j}\frac{\partial k}{\partial x_j}, \frac{1}{\omega^h\omega^h}\frac{\partial \omega^h}{\partial x_j}\frac{\partial \omega^h}{\partial x_j}\right), \tag{6.1}$$

has been introduced and calibrated to help the model go back to RANS very close to the walls. Because of the maximum function in

$$\begin{aligned} P_{SAS} &= 0.004\text{max}\left(T_1 - 8T_2, 0\right), \\ T_1 &= 1.755\kappa S^2\left(\frac{L_{SST}}{L_{vk}}\right)^{1/2} \end{aligned} \tag{6.2}$$

the forcing of the SAS term is eliminated if $8T_2 > T_1$, which means that the underlying JH-RSM is obtained. This can be used as a specific distinction in the blending of the numerical scheme for the convective terms, since anyway the model goes back to classic RANS under that circumstances. The hybrid scheme can be applied to complex flow cases with difficult to mesh geometries and not ideal cell aspect ratios close to walls. If $8T_2 > T_1$ the blending from 95 per cent CDS can be reduced to about 80 per cent. Such a scheme has been implemented and tested for simple cases. Fig.

6.1 shows, as an example, the outcome of the turbulent channel flow with respect to the areas with different numerical schemes. As can be seen the lower order one is used only very close to the walls, marked by the blue colour.

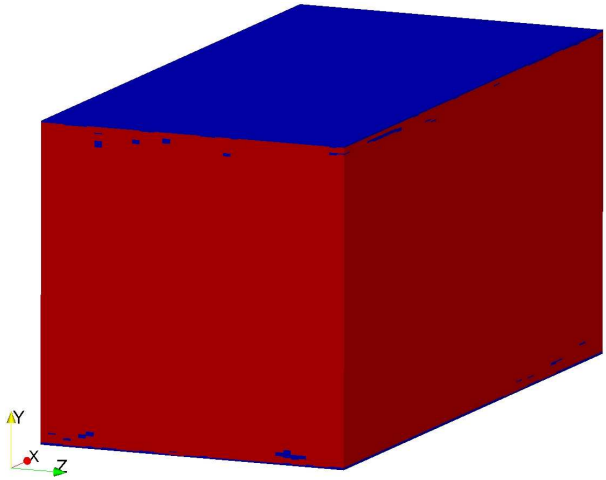

Figure 6.1: Hybrid numerical scheme for the turbulent channel flow - blue: 80 per cent CDS, red: 95 per cent CDS

To verify the proper operating mode, more testcases of varying complexity have to be computed in conjunction with the IS-RSM to draw final conclusions in respect to quantitative behavior. Nevertheless first simulations have shown a potential in that area that could help stabilizing the background RSM and so lead to a more widespread use of such models.

Bibliography

[1] ATAAC: Advanced Turbulence Simulation for Aerodynamic Application Challenges. *ATAAC A Seventh Framework Project*, 2009-2012

[2] B. Basara, S. Jakirlic: A new hybrid turbulence modelling strategy for industrial CFD. *INTERNATIONAL JOURNAL FOR NUMERICAL METHODS IN FLUIDS*, Volume 42, pages 89-116. John Wiley & Sons, Ltd., 2003.

[3] F. Billard, D. Laurence: A robust $k-\epsilon-\overline{v^2}/k$ elliptic blending turbulence model applied to near-wall, separated and buoyant flows. *International Journal of Heat and Fluid Flow*, Volume 33(4), pages 45-58. ELSEVIER, 2012.

[4] BOEING: Boeing Quiet Noise Technology Initiatives. *Backgrounder*, Boeing Commercial Airplanes, Seattle, Washington, USA.

[5] G. Brenn, S. Jakirlic, H.Steiner: Case 13.2: Flow in a 3-D diffuser. In *13th SIG15 ERCOFTAC Workshop on Refined Turbulence Modelling*, Graz University of Technology, Austria, 2008.

[6] M. Breuer: New Reference Data for the Hill Flow Test Case. *http://www.hy.bv.tum.de/DFG-CNRS/*, 2005.

[7] E.M. Cherry, G. Iaccarino, C.J. Elkins, J.K. Eaton: Separated flow in a three-dimensional diffuser: preliminary validation. *Annual Research Briefs 2006*, Center for Turbulence Research, Stanford University, pages 31-40 Stanford, 2006.

[8] L. Davidson: An Introduction to Turbulence Models. *Rept. 97/2*, Dept. of Thermo and Fluid Dynamics, Chalmers University of Technology, Göteborg, 1997.

[9] L. Davidson: EVALUATION OF THE SST-SAS MODEL: CHANNEL FLOW, ASYMMETRIC DIFFUSER AND AXI-SYMMETRIC HILL. In *European Conference on Computational Fluid Dynamics - ECCOMAS CFD 2006*, Egmond aan Zee, The Netherlands, 2007.

[10] D.M. Driver, H.L. Segmiller: Features of Reattaching Turbulent Shear Layer in Divergent Channel Flow. *AIAA Journal*, Volume 23(2), pages 163-171. 1985.

[11] P.A. Durbin: A Reynolds stress model for near-wall turbulence. *Journal of Fluid Mechanics*, Volume 249, pages 465-498. Cambridge University Press, 2003.

[12] Y. Egorov, F. Menter: Development and Application of the SST-SAS Turbulence Model in the DESIDER Project. In *Notes on Numerical Fluid Mechanics and Multidisciplinary Design*, Volume 97, pages 261-270. Springer, 2008.

[13] J.H. Ferziger, M. Peric: Numerische Strömungsmechanik. 1. Auflage. Springer, Berlin, 2008.

[14] J. Fröhlich, C.P. Mellen, W. Rodi, L. Temmerman, M.A. Leschziner: Highly Resolved Large-Eddy Simulation of Separated Flow in a Channel with Streamwise Periodic Constrictions. *Journal of Fluid Mechanics*, Volume 526, pages 19-66. Cambridge University Press, 2005.

[15] J. Gullbrand: Grid-independent large-eddy simulation in turbulent channel flow using three-dimensional explicit filtering. *Annual Research Briefs 2003*, Center for Turbulence Research, Stanford University, pages 331-342 Stanford, 2003.

[16] K. Hanjalic: TWO-DIMENSIONAL ASYMMETRIC TURBULENT FLOW IN DUCTS. PhD thesis, UNIVERSITY OF LONDON, August 1970.

[17] K. Iwamoto: Database for fully developed channel flow. *THTLAB Internal Report No. ILR-0201*, Department of Mechanical Engineering, The University of Tokyo, Tokyo, 2002.

[18] K. Iwamoto, N. Kasagi, Y. Suzuki: Reynolds Number Effect on Feedback Control of Wall Turbulence. In *International Symposium on Dynamics and Statistics of Coherent Structures in Turbulence*, pages 65-74. Tokyo, Japan, October 2002.

[19] S. Jakirlic: Reynolds-Spannungs-Modellierung komplexer turbulenter Strömungen. Doktorarbeit, Technische Fakultät der Universität Erlangen-Nürnberg, Herbert Utz Verlag, Erlangen, 1997.

[20] S. Jakirlic, K. Hanjalic: A new approach to modelling near-wall turbulence energy and stress dissipation. *Journal of Fluid Mechanics*, Volume 459, pages 139-166. Cambridge University Press, 2002.

[21] S. Jakirlic, J. Jovanovic: On unified boundary conditions for improved predictions of near-wall turbulence. *Journal of Fluid Mechanics*, Volume 656, pages 530-539. Cambridge University Press, 2010.

[22] L.N. Jenkins, M.R. Khorrami, M.M. Choudhari, C.B. McGinley: Characterization of unsteady flow structures around tandem cylinders for component interaction studies in airframe noise. *AIAA paper 2005-2812*, 2005.

[23] L.N. Jenkins, D.H. Neuhart, C.B. McGinley, M.M. Choudhari, M.R. Khorrami: Measurements of unsteady wake interference between tandem cylinders. *AIAA paper 2006-3206*, 2006.

[24] J. Jimenez, S. Hoyas: Turbulent fluctuations above the buffer layer of wall-bounded flows. *Journal of Fluid Mechanics*, Volume 611, pages 215-236. Cambridge University Press, 2008.

[25] S. Jovic, D. Driver: Reynolds number effect on the skin friction in separated flows behind a backward-facing step. *Experiments in Fluids*, Volume 18(6), pages 464-467. Springer, 1995.

[26] M.R. Khorrami, M.M. Choudhari, L.N. Jenkins, C.B. McGinley: UNSTEADY FLOWFIELD AROUND TANDEM CYLINDERS AS PROTOTYPE FOR COMPONENT INTERACTION IN AIRFRAME NOISE. In *11th AIAA/CEAS Aeroacoustics Conference*, Monterey, California, USA, 2005.

[27] N. Kornev, E. Hassel: Synthesis of homogeneous anisotropic divergence-free turbulent fields with prescribed second-order statistics by vortex dipoles. *Physics of Fluids*, Volume 19(6), 4 pages. American Institute of Physics, 2007.

[28] P.L. Lasagna, K.G. Mackall, F.W. Burcham Jr., T.W.Putnam: Landing Approach Airframe Noise Measurements and Analysis. *NASA Technical Paper 1602*, 1980.

[29] B.E. Launder, B.I. Sharma: Application of the Energy-Dissipation Model of Turbulence to the Calculation of Flow Near a Spinning Disc. *Letters in Heat and Mass Transfer*, Volume 1(2), pages 131-138. Nov.-Dec. 1974.

[30] B.E. Launder, G.J. Reece, W. Rodi: Progress in the development of a Reynolds-stress turbulence closure. *Journal of Fluid Mechanics*, Volume 68(3), pages 537-566. Cambridge University Press, 1975.

[31] B.E. Launder, D.B. Spalding: The numerical computation of turbulent flows. *Computer Methods in Applied Mechanics and Engineering*, Volume 3(2), pages 269-289. 1974.

[32] H. Le, P. Moin, J. Kim: Direct numerical simulation of turbulent flow over a backward-facing step. *Journal of Fluid Mechanics*, Volume 330, pages 349-374. Cambridge University Press, 1997.

[33] F.R. Menter, Y. Egorov: Formulation of the Scale-Adaptive Simulation (SAS) model during the DESIDER Project. In *Notes on Numerical Fluid Mechanics and Multidisciplinary Design*, Volume 103, pages 51-61. Springer, 2009.

[34] F.R. Menter, Y. Egorov: Revisiting the Turbulent Scale Equation. In *IUTAM Symposium on One Hundred Years of Boundary Layer Research Solid mechanics and its applications*, Volume 129, pages 279-290. Springer, 2006.

[35] F. R. Menter, Y. Egorov: The Scale-Adaptive Simulation Method for Unsteady Turbulent Flow Predictions. Part1: Theory and Model Description. *Journal of Flow, Turbulence and Combustion*, Volume 85(1), pages 113-138. Springer, 2010.

[36] F.R. Menter, M. Kuntz, R. Bender: A scale-adaptive simulation model for turbulent flow predictions. *AIAA paper 2003-0767*, 2003.

[37] D.H. Neuhart et al.: Measurements of the Flowfield Interaction Between Tandem Cylinders. *AIAA paper 2009-3275*, 2009.

[38] S. Obi: Berechnung komplexer turbulenter Strömungen mit einem Reynolds-Spannungs-Modell. Doktorarbeit, Technische Fakultät der Universität Erlangen-Nürnberg, Erlangen, 1991.

[39] S. Obi, K. Aoki, S. Masuda: Experimental and computational study of turbulent separating flow in an asymmetric plane diffuser. In *Ninth Symposium on Turbulent Shear Flows*, page 305. Kyoto, Japan, 1993.

[40] J. Ohlsson, P. Schlatter, P.F. Fischer, D.S. Henningson: Direct numerical simulation of separated flow in a three-dimensional diffuser.

Journal of Fluid Mechanics, Volume 650, pages 307-318. Cambridge University Press, 2010.

[41] OpenCFD: Ltd. http://www.opencfd.co.uk/openfoam/. 2010.

[42] U. Piomelli, E. Balaras: WALL-LAYERMODELS FOR LARGE-EDDY SIMULATIONS. *Annual Revue of Fluid Mechanics*, Volume 34, pages 349-374. 2002.

[43] S.B. Pope: Turbulent Flows. 1st printing. Cambridge University Press, August 2000.

[44] M. Popovac, K. Hanjalic: Compound Wall Treatment for RANS Computation of Complex Turbulent Flows and Heat Transfer. *Journal of Flow Turbulence and Combustion*, Volume 78(2), pages 177-202. Springer Science, 2007.

[45] C. Rapp: Experimentelle Studie der turbulenten Strömung über periodische Hügel. PhD thesis, Technische Universität München, 2009.

[46] O. Reynolds: An experimental investigation of the circumstances which determine whether the motion of water in parallel channels shall be direct or sinuous and of the law of resistance in parallel channels. *Philosophical Transactions of the Royal Society*, Volume 35, pages 84-99. 1883.

[47] O. Reynolds: On the dynamical theory of incompressible viscous fluids and the determination of the criterion. *Philosophical Transactions of the Royal Society of London*, Volume 186, pages 123-164. 1895.

[48] J.C. Rotta: Turbulente Strömungen. Teubner Verlag, Stuttgart, 1972.

[49] M. Schäfer: Numerik im Maschinenbau. 1. Auflage. Springer, Fachmedien Wiesbaden, 1999.

[50] B.W. Spencer: Statistical investigation of turbulent velocity and pressure fields in a two-dimensional mixing layer. Dissertation, University of Illinois, Illinois, 1970.

[51] S. Tavoularis, J. Jimenez, O. Leuchter: A Selection of Test Cases for the Validation of Large-Eddy Simulations of Turbulent Flows - Homogeneous Flows. *AGARD ADVISORY REPORT NO 345*, Working Group 21 of the Fluid Dynamics Panel of AGARD, 1997.

[52] E. de Villiers: The Potential of Large Eddy Simulation for the Modeling of Wall Bounded Flows. PhD thesis, Thermofluids Section, Department of Mechanical Engineering, Imperial College of Science, Technology and Medicine, London 2006.

[53] D.C. Wilcox: Formulation of the $k\omega$ Turbulence Model Revisited. *AIAA Journal*, Volume 46(11), pages 2823-2838. 2008.

[54] Y.J. Yang, L. Temmerman, M.A. Leschziner: INVESTIGATION OF ANISOTROPY-RESOLVING TURBULENCE MODELS BY REFERENCE TO HIGHLY-RESOLVED LES DATA FOR SEPARATED FLOW. In *European Conference on Computational Fluid Dynamics - ECCOMAS CFD 2001*, Swansea, Wales, UK, 2001.

Nomenclature

Latin letters

upper case

symbol	SI unit	description
$2D\ TKE$	m^2/s^2	two dimensional turbulent kinetic energy
$(C_p)_{rms}$	–	root mean square of the pressure coefficient
A	–	Reynolds stress anisotropy
B	m	width of the duct
C_f	–	friction coefficient
C_p	–	pressure coefficient
D	m	cylinder diameter
E	m^2/s^4	near wall term in the dissipation equation
$E(\kappa)$	m^2/s	energy content over wavenumbers in spectral space
H	m	step, duct or hill height
L	m	integral/ turbulent length scale or distance in between the cylinders
$L_{\nu K}$	m	von Karman lenth scale
$P_{\epsilon,3}$	m^2/s^4	production of the dissipation due to mean velocity gradients
P_k	m^2/s^3	production of the turbulent kinetic energy
P_ω	$1/s^2$	production of the specific dissipation
P_{SAS}	$1/s^2$	extra production in the specific dissipation equation according to the scale adaptivity concept
R_{ij}	m^2/s^2	two-point correlation tensor
Re	–	Reynolds number
Re_H	–	Reynolds number based on step or hill height
Re_λ	–	Reynolds number based on the Taylor microscale

Re_τ	–	friction Reynolds number
S	1/s	strain rate
U^+	–	velocity normalized by the friction velocity
U_0	m/s	maximum free stream velocity
U_b	m/s	bulk velocity in streamwise direction
U_i	m/s	velocity vector in index notation

lower case

symbol	SI unit	description
k	m^2/s^2	turbulent kinetic energy
k^+	–	turbulent kinetic energy normalized by the friction velocity
k_P	m^2/s^2	turbulent kinetic energy in the first point close to the wall
p	m^2/s^2	normalized pressure
$p^{'}$	m^2/s^2	normalized fluctuating pressure
p_0	m^2/s^2	normalized inlet pressure
p_{ref}	m^2/s^2	normalized pressure at a reference point
p_{rms}	m^2/s^2	root mean square of the normalized pressure
r_y	m	distance between two probes
u^+	–	normalized streamwise stress component
v^+	–	normalized longitudinal stress component
w^+	–	normalized lateral stress component
u_i	m/s	fluctuating velocity vector in index notation
u_τ	m/s	friction velocity
$\overline{u_i u_j}$	m^2/s^2	Reynolds stress tensor
$\overline{uv}^+$	–	normalized shear stress component
y^+	–	wall distance normalized by the friction velocity
y_P	m	wall distance of first computational point

Greek letters

upper case

symbol	SI unit	description
ΔU	m/s	difference between two velocities in streamwise direction
Θ	[deg]	angle to mark points on the cylinder surface
Φ	m^2/s	effective length scale in terms of $\sqrt{k}$
Φ_S	(*)	any arbitrary scalar quantity
Φ_{ij}	m^2/s^3	pressure strain tensor
Ψ	m^3/s^2	effective length scale in terms of k

lower case

symbol	SI unit	description
δ	m	shear layer thickness at mixing layer inlet
ϵ	m^2/s^3	dissipation of the turbulent kinetic energy
ϵ^h	m^2/s^3	homogeneous part of the dissipation of the turbulent kinetic energy
ϵ^{h+}	–	homogeneous part of the dissipation of the turbulent kinetic energy normalized by the friction velocity
ϵ^h_{ij}	m^2/s^3	homogeneous dissipation tensor
ϵ^h_{wall}	m^2/s^3	wall value of the homogeneous part of the dissipation of the turbulent kinetic energy
ζ_1, ζ_2, ζ_3	–	constant coefficients in the Ψ equation
κ	–	von Karman constant
κ	1/m	wavenumber
λ	m	Taylor microscale
ν	m^2/s	kinematic molecular viscosity
ν_τ	m^2/s	turbulent viscosity
π	–	mathematical constant

ρ	kg/m^3	fluid density
σ, σ_ϵ, σ_k, σ_Ψ	–	constant coefficients in front of turbulent diffusion models
ω	$1/s$	specific dissipation
ω^h	$1/s$	homogeneous part of the specific dissipation
ω^{h+}	–	homogeneous part of the specific dissipation normalized by the friction velocity
ω^h_{wall}	$1/s$	wall value of homogeneous part of the specific dissipation

Mathematical symbols

symbol	description
$\mathrm{D}/\mathrm{D}t$	material derivative
δ_{ij}	Kronecker delta

Abbreviations

symbol	description
2D	two-dimensional
3D	three-dimensional
ATAAC	Advanced Turbulence Simulation for Aerodynamic Application Challenges
BART	Basic Aerodynamics Research Tunnel
CFD	computational fluid dynamics
CFL number	Courant Friedrichs Lewy number
CDS	central differencing scheme
DESIDER	Detached Eddy Simulation for Industrial Aerodynamics
DNS	direct numerical simulation
ERCOFTAC	European Research Community On Flow, Turbulence and Combustion
IS-RSM	instability sensitive Reynolds stress model
JH-RSM	Jakirlic-Hanjalic Reynolds stress model
LES	large eddy simulation
NASA	National Aeronautics and Space Administration
RANS	Reynolds-averaged Navier-Stokes
RSM	Reynolds stress model
RSTM	Reynolds stress transport model
SAS	scale adaptive simulation
SIG	special interest group
SST	shear stress transport

UDS	upwind differencing scheme
URANS	unsteady Reynolds-averaged Navier-Stokes

List of Figures

List of Tables

Appendix A

ω^h-based Reynolds stress model

(i) Reynolds stress equation:

$$\frac{\mathrm{D}\overline{u_i u_j}}{\mathrm{D}t} = \frac{\partial}{\partial x_k}\left[\left(\frac{1}{2}\nu\delta_{kl} + C_s\frac{k}{\epsilon^h}\overline{u_k u_l}\right)\frac{\partial\overline{u_i u_j}}{\partial x_l}\right] - \left(\overline{u_i u_k}\frac{\partial U_j}{\partial x_k} + \overline{u_j u_k}\frac{\partial U_i}{\partial x_k}\right) + \Phi_{ij} - \epsilon^h_{ij}.$$

Pressure strain model:

$$\Phi_{ij} = \Phi_{ij,1} + \Phi^w_{ij,1} + \Phi_{ij,2} + \Phi^w_{ij,2},$$

$$\Phi_{ij,1} = -C_1\epsilon^h a_{ij}, \quad \Phi_{ij,2} = -C_2\left(P_{ij} - \frac{2}{3}P_k\delta_{ij}\right),$$

$$\Phi^w_{ij,1} = C^w_1 f_w\frac{\epsilon^h}{k}\left(\overline{u_k u_m}n_k n_m\delta_{ij} - \frac{3}{2}\overline{u_i u_k}n_k n_j - \frac{3}{2}\overline{u_k u_j}n_k n_i\right),$$

$$\Phi^w_{ij,2} = C^w_2 f_w\left(\Phi_{km,2}n_k n_m\delta_{ij} - \frac{3}{2}\Phi_{ik,2}n_k n_j - \frac{3}{2}\Phi_{kj,2}n_k n_i\right),$$

where

$$C_1 = C + \sqrt{A}E^2, \quad C = 2.5AF^{1/4}f, \quad F = min\left[0.6; A_2\right],$$

$$f = min\left[\left(\frac{Re_t}{150}\right)^{3/2}; 1\right], \quad f_w = min\left[\frac{k^{3/2}}{2.5\epsilon^h x_n}\right],$$

$$C_2 = 0.8A^{1/2}, \quad C_1^w = max\left(1 - 0.7C; 0.3\right), \quad C_2^w = min\left(A; 0.3\right),$$

$$A = 1 - 9/8\left(A_2 - A_3\right), \quad A_2 = a_{ij}a_{ji}, \quad A_3 = a_{ij}a_{jk}a_{ki},$$

$$E = 1 - 9/8\left(E_2 - E_3\right), \quad E_2 = e_{ij}e_{ji}, \quad E_3 = e_{ij}e_{jk}e_{ki},$$

$$e_{ij} = \frac{\epsilon_{ij}^h}{\epsilon^h} - \frac{2}{3}\delta_{ij}, \quad a_{ij} = \frac{\overline{u_i u_j}}{k} - \frac{2}{3}\delta_{ij}.$$

Stress-dissipation rate model:

$$\epsilon_{ij}^h = \left(1 - f_s\right)\frac{2}{3}\delta_{ij}\epsilon^h + f_s\frac{\overline{u_i u_j}}{k}\epsilon^h, \quad \text{where} \quad f_s = 1 - \sqrt{A}E^2, \quad \epsilon^h = \omega^h k.$$

(ii) Specific dissipation equation:

$$\frac{\mathrm{D}\omega^h}{\mathrm{D}t} = \frac{\partial}{\partial x_k}\left[\left(\frac{1}{2}\nu + \frac{\nu_t}{\sigma}\right)\frac{\partial\omega^h}{\partial x_k}\right] - \left(C_{\epsilon 1} - 1\right)\frac{\omega^h}{k}\overline{u_i u_j}\frac{\partial U_i}{\partial x_j}$$
$$- \left(C_{\epsilon 2} - 1\right)\omega^h\omega^h + \frac{2}{k}\left(0.55\frac{1}{2}\nu + \frac{\nu_t}{4}\right)\frac{\partial\omega}{\partial x_k}\frac{\partial k}{\partial x_k} + \frac{2}{k}\nu\nu_t\left(\frac{\partial^2 U_i}{\partial x_j^2}\right)^2,$$

$$\nu_t = 0.144 \cdot A \cdot k^{1/2} \cdot min\left[10\left(\frac{\nu^3}{k\omega^h}\right)^{1/4}, \frac{k^{1/2}}{\omega^h}\right).$$

Summary of the remaining coefficients:

$$C_s = 0.22, C_\epsilon = 0.18, C_{\epsilon 1} = 1.44, C_{\epsilon 2} = 1.80, C_{\epsilon 3} = 0.32.$$

Appendix B

instability sensitive Reynolds stress model

The model equation for the Reynolds stress tensor is the one given in Appendix A. The only difference is the model equation for ω^h which was extended through introduction of the P_{SAS} term:

$$\frac{\mathrm{D}\omega^h}{\mathrm{D}t} = \frac{\partial}{\partial x_k}\left[\left(\frac{1}{2}\nu + \frac{\nu_t}{\sigma}\right)\frac{\partial \omega^h}{\partial x_k}\right] - (C_{\epsilon 1} - 1)\,\frac{\omega^h}{k}\overline{u_i u_j}\frac{\partial U_i}{\partial x_j}$$
$$- (C_{\epsilon 2} - 1)\,\omega^h\omega^h + \frac{2}{k}\left(0.55\frac{1}{2}\nu + \frac{\nu_t}{4}\right)\frac{\partial \omega}{\partial x_k}\frac{\partial k}{\partial x_k} + \frac{2}{k}\nu\nu_t\left(\frac{\partial^2 U_i}{\partial x_j^2}\right)^2 + P_{SAS},$$

where

$$P_{SAS} = 0.004\mathrm{max}\left(1.755\kappa S^2\left(\frac{L_{SST}}{L_{vk}}\right)^{1/2} - 8T_2, 0\right),$$
$$T_2 = \frac{k}{1/3}max\left(\frac{1}{k^2}\frac{\partial k}{\partial x_j}\frac{\partial k}{\partial x_j}, \frac{1}{\omega^h\omega^h}\frac{\partial \omega^h}{\partial x_j}\frac{\partial \omega^h}{\partial x_j}\right),$$

$$L_{vK} = \kappa\left|\frac{U^{'}}{U^{''}}\right|, \quad L_{SST} = \frac{k^{1/2}}{C_\mu^{1/4}\omega^h}, \quad U^{''} = \sqrt{\frac{\partial^2 U_i}{\partial x_k^2}\frac{\partial^2 U_i}{\partial x_j^2}}, \quad U^{'} = \sqrt{2\cdot S_{ij}S_{ij}}.$$

Robert Maduta

Outotec GmbH
Ludwig-Erhard-Straße 21
D-61440 Oberursel
Germany

phone: +49 6171 7100
email: robert.maduta@outotec.com

Personal

Born on August 19, 1981, in Bukarest, Romania
(German citizenship)

Education

04/2009 - 10/2012	Doctoral research in Mechanical Engineering (Dr.-Ing.), Technische Universität Darmstadt, Darmstadt, Germany
10/2002 - 02/2009	Studies in Mechanical Engineering (Dipl.-Ing.), Technische Universität Darmstadt, Darmstadt, Germany

Employment

since 06/2013	Research engineer at Outotec GmbH Oberursel, Germany

...